TAMPEREEN TEKNILLINEN YLIOPISTO
TAMPERE UNIVERSITY OF TECHNOLOGY

Jarmo Makkonen

Classification of Metallic Targets Using a Walk-Through Metal Detection Portal

Julkaisu 1361 • Publication 1361

Tampere 2015

Tampereen teknillinen yliopisto. Julkaisu 1361
Tampere University of Technology. Publication 1361

Jarmo Makkonen

Classification of Metallic Targets Using a Walk-Through Metal Detection Portal

Thesis for the degree of Doctor of Science in Technology to be presented with due permission for public examination and criticism in Tietotalo Building, Auditorium TB109, at Tampere University of Technology, on the 15th of January 2016, at 12 noon.

Tampereen teknillinen yliopisto - Tampere University of Technology
Tampere 2016

ISBN 978-952-15-3668-7 (printed)
ISBN 978-952-15-3698-4 (PDF)
ISSN 1459-2045

Abstract

Metal detectors have been used for a long time for treasure hunting, security screening, and finding buried objects such as landmines or unexploded ordnance. Walk-through metal detection (WTMD) portals are used for making sure that forbidden or threatening metallic items, such as knives or guns, are not carried into secure areas at critical locations such as airports, court rooms, embassies, and prisons.

The 9/11 terrorist act has given rise to stricter rules for aviation security worldwide, and the ensuing tighter security procedures have meant that passengers face more delays at airports. Moreover, the fear of terrorism has led to the adoption of security screening technology in a variety of places such as railway and coach stations, sports events, malls, and nightclubs.

However, the current WTMD technology and scanning procedures at airports require that all metallic items be removed from clothing prior to scanning, causing inconvenience. Furthermore, alarms are triggered by innocuous items such as shoe shanks and artificial joints, along with overlooked items such as jewellery and belts. These lead to time-consuming, manual pat-down searches, which are found inconvenient, uncomfortable, and obtrusive by some.

Modern WTMD portals are very sensitive devices that can detect items with only small amounts of metal, but they currently lack the ability to further classify the detected item. However, if a WTMD portal were able to classify objects reliably into, e.g., “knives”, “belts”, “keys”, the need for removing the items prior to screening would disappear, enabling a paradigm shift in the field of security screening.

This thesis is based on novel research presented in five peer-reviewed publications. The scope of the problem has been narrowed down to a situation in which only one metallic item is carried through the portal at a time. However, the methods and results presented in this thesis can be generalized into a multi-object scenario. It has been shown that by using a WTMD portal and the magnetic polarisability tensor, it is possible to accurately distinguish between threatening and innocuous targets and to classify them into 10 to 13 arbitrary classes. Furthermore, a data library consisting of natural walk-throughs has been collected, and it has been demonstrated that the walk-through data collected with the above portal are subject to phenomena that might affect classification, in particular a bias and the so-called body effect. However, the publications show that, by using realistic walk-through data, high classification accuracy can be maintained regardless of the above problems. Furthermore, a self-diagnostics method for detecting unreliable samples has also been presented with potential to significantly increase classification accuracy and the reliability of decision making.

The contributions presented in this thesis have a variety of implications in the field of WTMD-based security screening. The novel technology offers more information, such as

an indication of the probable cause of the alarm, to support the conventional screening procedure. Moreover, eliminating the need for removing all metallic items prior to screening enables design of new products for scenarios such as sports events, where conventional screening procedures might be inconvenient, creating thus new business possibilities for WTMD manufacturing companies.

The positive results give rise to a variety of future research topics such as using wideband data, enabling simultaneous classification of multiple objects, and developing the portal coil design to diminish signal nonlinearities. Furthermore, the ideas and the basic principles presented in this thesis may be applied to other metal detection applications, such as humanitarian demining.

Preface

The work for this study was carried out between 2012 and 2015 for the *MIDAS2*-project at Tampere University of Technology (TUT) and The University of Manchester (UoM), United Kingdom (UK).

First, I would like to thank my pre-examiners Vedran Bilas and Bill Lionheart for accepting the task of examining this thesis, and for very good comments that improved the final manuscript. The funding of Academy of Finland is gratefully acknowledged. Without it, this work would not have been possible. In addition, I would like to thank Rapiscan Systems for their cooperation in the *MIDAS2*-project. Special thanks go to Ari Järvi for sharing his knowledge as well as enabling me to use such a wide range of test objects.

Dr. Juho Vihonen deserves a huge amount of credit for his supervision, guidance and the countless hours we spent discussing the papers to the finest detail. I am grateful for his support, and that he gave me the opportunity to work on this project.

Prof. Ari Visa (TUT) gave me the opportunity to continue working as a research assistant at TUT back in 2002. I would like to thank him for his confidence in me during all these years.

I would like to express my sincere gratitude to Prof. Anthony Peyton for the possibility to work in his laboratory, but most importantly, for his support whenever I needed it. Dr. Liam Marsh played an instrumental role in the work presented in this thesis. He walked me through the details of walk-through metal detection technology, answered my questions tirelessly, and was all in all a brilliant colleague. Thank you Liam. Also, I would like to thank Dr. Michael O'Toole and Dr. John Wilson (UoM), among other colleagues at UoM, for their friendship and for making me feel at home during my time in the UK.

Special thanks go to all my colleagues at TUT. It has been a pleasure to work in an environment where you can truly consider your colleagues to be your friends. I would also like to thank Virve Larmila and other TUT staff who made it so easy for us researchers to concentrate on our work. Furthermore, the system administrator of the group, Antti Orava, deserves to be singled out for credit, both for his professionalism in maintaining everyday work routines at the lab, and for sharing an office with me.

Finally, I want to thank Sonja for her support and understanding during this long project that has forced me to spend weekends and long evenings at my desk and laptop.

Contents

Acronyms

3D	Three-dimensional
BOD	Buried object detection
BoR	Body of revolution
CW	Continuous wave
CWD	Concealed weapon detection
DSRF	Discrete spectrum of relaxation frequencies
EM	Electromagnetic
EMD	Earth mover's distance
EMI	Electromagnetic induction
FP	False positive
GLRT	Generalized likelihood ratio test
KDE	Kernel density estimation
KNN	K-nearest neighbour
LDA	Linear discriminant analysis
LMA	Levenberg-Marquardt algorithm
LR	Logistic regression
LRT	Likelihood ratio test
MLE	Maximum likelihood estimate
MPT	Magnetic polarisability tensor
MSI	Magnetic singularity identification
NIJ	National Institute of Justice
NN	Neural network
NSMS	Normalized surface magnetic source
OAA	One-against-all
OAO	One-against-one
ONVMS	Orthonormalized volume magnetic source
PDF	Probability density function
RBF	Radial basis function
SEM	Singularity expansion method
SI	International system of units
SNR	Signal-to-noise ratio
sRVM	Structured relevance vector machine
SVM	Support vector machine
TUT	Tampere University of Technology
UIT	Unreliably inverted tensor
UK	United Kingdom
UoM	University of Manchester
US	United States of America
UXO	Unexploded ordnance
WTMD	Walk-through metal detection

Nomenclature

The following is not an exhaustive list of all symbols in this thesis. However, there are various symbols used throughout this thesis and they are listed here, along with some selected important ones. The symbols that are not included here are explained whenever used, or their meaning will be clear from the context of use. The use of a symbol for several distinct purposes has been avoided.

Latin alphabet

$D(a, b)$	Distance between a and b
$\mathbf{H}_\mathrm{t}$, $\mathbf{H}_\mathrm{r}$	H-fields for transmit and receive coils, respectively
$\Im\{\}$	Imaginary part of the given complex number
$\mathbf{j}$	Imaginary unit
$K(\mathbf{a}, \mathbf{b})$	Kernel function of input vectors $\mathbf{a}$ and $\mathbf{b}$
K	Neighbourhood size parameter for the KNN algorithm
$\overleftrightarrow{\mathbf{M}}$	Theoretical magnetic polarisability tensor
$\widehat{\overleftrightarrow{\mathbf{M}}}$	Estimated magnetic polarisability tensor
$m_{i,j}$	Element (i, j) of an MPT matrix
N	Number of elements (in a vector, sum, etc.)
$\mathbf{p}$	Object xyz-position vector
$\hat{\mathbf{p}}$	Estimated object xyz-position vector
$\mathbf{P}$	Theoretical object trajectory
$\hat{\mathbf{P}}$	Estimated object trajectory
$P(var)$	Probability of var
$P(var_1 \mid var_2)$	Probability of var_1, given var_2
$\mathbf{Q}(\omega)$	Quadrature signal
r	Residual value
$\mathbf{R}(\omega)$	In-phase signal
$\Re\{\}$	Real part of the given complex number
t	Time
$\mathbf{x}$	Sample, feature vector

Greek alphabet

$\boldsymbol{\beta}$	Levenberg-Marquardt solution, sample consisting of $\widehat{\overleftrightarrow{\mathbf{M}}}$ and $\hat{\mathbf{P}}$
λ	MPT eigenvalue
$\boldsymbol{\lambda}$	1x3 vector of MPT eigenvalues
$\boldsymbol{\mu}$	Bias signal
ω	Angular frequency

$\boldsymbol{\Omega}$	Set of classes, i.e., states of nature
Ω_i	Class i
$\boldsymbol{\rho}$	Theoretical portal input signal
$\hat{\boldsymbol{\rho}}$	Measured portal input signal
τ	Magnitude of eigenvalue λ
φ	Phase angle of eigenvalue λ

List of Publications

I Makkonen J., Marsh L. A., Vihonen, J., Visa, A., Järvi, A., Peyton, A. J. "Classification of metallic targets using a single frequency component of the magnetic polarisability tensor", *Journal of Physics: Conference Series, 450(1):012038, 2013.*

II Makkonen J., Marsh L. A., Vihonen, J., Järvi, A., Armitage, D. W., Visa, A., Peyton, A. J. "KNN Classification of Metallic Targets using the Magnetic Polarizability Tensor", *Measurement Science and Technology, 25(5):055105, 2014.*

III Marsh L. A., Makkonen J., Vihonen, J., Visa, A., Järvi, A., Armitage, D. W., Peyton, A. J. "Investigation of the significance of the 'body effect' on sensitivity to metallic objects in a walk-through metal detector", *Journal of Physics: Conference Series, 450(1):012037, 2013.*

IV Makkonen J., Marsh L. A., Vihonen, J., O'Toole, M. D., Armitage, D. W., Järvi, A., Peyton, A. J., Visa, A. "Determination of Material and Geometric Properties of Metallic Objects using the Magnetic Polarisability Tensor", *IEEE Sensors Applications Symposium (SAS), Zadar, Croatia, 13-15 April, 2015.*

V Makkonen J., Marsh L. A., Vihonen, J., Järvi, A., Armitage, D. W., Visa, A., Peyton, A. J. "Improving Reliability for Classification of Metallic Objects using a WTMD Portal", *Measurement Science and Technology, 26(10):105103, 2015.*

1 Introduction

Metal detectors have been used for a long time for treasure hunting, security screening, and finding buried objects such as landmines or unexploded ordnance (UXO). History tells us that the first proper metal detector was used already in 1881 by Dr. Alexander Graham Bell. The then president of the United States of America (US), James Garfield, had been shot by an assassin. A bullet was stuck inside the president, and in an attempt to save his life, Dr. Bell developed a device that could successfully detect small concealed metallic items. However, the device did not work on the president and the bullet was not found. Later, it was discovered that the metallic coil spring bed that the president was lying on caused so much background noise as to compromise Dr. Bell's effort [1]. This is an important lesson about the significance of background interference and signal-to-noise ratio (SNR) in detecting and classifying metallic objects.

Metal detection technology was already in use at the time of World War II and advanced rapidly due to the need for land mine detection [2]. A study by Roston [3] proves that, already in 1948, the research community knew how to distinguish between ferrous and conductive targets. The motivation for the separation was to suppress unwanted signals caused by elements such as ferrous rocks and thus to avoid the problem of the above Bell scenario.

Walk-through metal detection (WTMD) portals are devices capable of detecting metallic items carried through their detection space. The portals are used to ensure that forbidden or threatening metallic items, such as knives or guns, are not carried into secure areas. Airports are perhaps the obvious examples of metal detection, but these devices have also been used at, for example, government buildings, such as court rooms, embassies, and prisons. Historically, the reason for adopting WTMD technology, first at airports, was that between 1968-1972, 364 plane hijackings were reported worldwide. Consequently, a law was introduced in 1973, stating that all passengers and their luggage must be checked for concealed weapons [4, 5].

In fact, a great number of plane hijackings have been carried out by using knives instead of firearms. For example, such a case happened in New York in September 2001 (*The 9/11 terrorist act*), when two commercial flights were hijacked and crashed into buildings, causing the death of 2996 people and significant damage to the buildings, e.g., destroying two 110-story World Trade Center towers [6]. This gave rise to stricter rules for aviation security worldwide [7]. Tighter security measures mean that passengers must now arrive earlier at airports and face more delays [8].

Moreover, after this terrifying incident, the fear of terrorism has led to the adoption of security screening technology in a variety of scenarios. High speed trains [9], bus stations [10], marine ports, sports events [11 – 13] and even malls [14, 15], nightclubs, and schools [16, 17] have been secured, or have been suggested to be secured by using WTMD portals.

However, e.g., the current WTMD technology and scanning procedure at the airports requires that passengers must remove all metallic items from their clothing prior to scanning. Furthermore, if the portal sets off an alarm, a manual pat-down search must be conducted on the passenger, a procedure that is time-consuming, labour and capacity intensive (i.e., more parallel lines for scanning), and therefore causes delays. Passengers may find this inconvenient, and the pat-down search is seen as uncomfortable and obtrusive. In addition, those with artificial, metallic hip, or shoulder joint replacements often trigger the current detectors [18], resulting in unnecessary searches.

Modern WTMD portals are very sensitive devices and can detect items with only small amounts of metal, such as handcuff keys [19]. However, their ability to further classify the detected item is limited. The portals must fulfill a certain set of requirements [20] defined by, e.g., the US National Institute of Justice (NIJ [21]). These requirements specify which *threatening* items must be detected by the portal and trigger an alarm, and, on the other hand, which *innocuous* items should not trigger an alarm. There is also an upper limit for the number of allowed false alarms (i.e., the *false positive (FP) rate*). These requirements change due to increasing safety concerns that again affect legislation. Therefore, portal devices must be modifiable in order to accommodate any new requirements.

In addition to their ability to detect the metallic items, modern portals can roughly determine the location of the potential threat. This implementation varies by the manufacturer, but generally the portals indicate a portal region or a horizontal/vertical band of the likely object location and thus help security personnel in their manual pat-down search.

The current practice of removing all metal before scanning simplifies the task of the portal by significantly narrowing down the problem scenario. However, if the WTMD portal could, in addition to detecting the metallic items, reliably classify objects into classes “knife”, “belt”, “lighter”, “keys”, and such, the need to remove them items would disappear and allow, e.g., the passengers with artificial joints to bypass time-consuming pat-down searches. Moreover, crowds of people entering, e.g., shopping centres or sports events would be inconvenient and slow to scan using the airport style procedure, in which all metal has to be removed before screening. Fine-grained classification of objects would enable portal manufacturers to design a variety of new products for high throughput of people without compromising safety. The purpose of this thesis is to show that such a paradigm shift in WTMD-based security screening is possible.

1.1 Related work

Walk-through metal detection belongs to a wider scope of concealed weapon detection (CWD). The use of a variety of other technologies has been proposed for CWD, including millimetre waves, and Terahertz, Infrared, and X-ray -imaging [22, 23]. These, however, will not be covered in this thesis.

There are a few approaches in the literature that have dealt with an intelligent WTMD system, based both on electromagnetic induction (EMI) and magnetometer sensors. The approaches by Al-Qubaa et al. [24], Elgwel et al. [25], and Kauppila et al. [26] use EMI, and these studies will be discussed further in Chapter 5. On the other hand, Roybal et al. [27] and Kotter et al. [28] used a magnetometer -based portal to detect and locate metallic objects and to discriminate between threatening and innocuous items. Magnetometers are limited in that they can detect only magnetic materials; therefore, objects made of non-magnetic steels, such as some knives, will go undetected.

Detecting and classifying metallic objects by using EMI has been studied widely by other research communities. The technology has been applied to detecting and classifying buried metallic objects (buried object detection and identification, BOD), namely landmines [29] and unexploded ordnance [30, 31]. The literature on these fields contains a great amount of useful information that can be applied to the problem field of this thesis. The applicability of these technologies to security scanning at airports was acknowledged already in 1997 [32]. The main differences between the fields (CWD and BOD) are as follows:

- Prior knowledge of target objects: In BOD, the types of targets likely to be encountered are known. In CWD, not many assumptions can be made of threat items.
- Sensor/target movement: In BOD, the sensor moves while the target remains stationary. In CWD, the target moves while the sensor remains stationary.
- Type of EMI technique: In this thesis, a continuous wave (CW) excitation technique is used at a single frequency. In the BOD literature, CW is sometimes used, but most studies concentrate on pulsed EMI. Studies on pulsed EMI are referred to whenever the knowledge is applicable to our system, or to provide general background knowledge. The principles of these techniques are covered in Chapter 2.

1.2 Objectives of the thesis

The main objective of this thesis is to show that *metallic target objects can be reliably classified* by using a WTMD portal, which is capable of estimating the *magnetic polarisability tensor (MPT)* and the trajectory of the target.

To achieve its main objective, this thesis contains the following key contributions:

- To present a data library that has been collected to investigate the responses of typical metallic objects; and
- To present the characteristics of the data in the library and the physical phenomena that pose challenges to classification.

The main objective is divided into secondary objectives as follows:

- To show that metallic objects in the above library can be classified as threatening or innocuous and into 10 to 13 classes; and
- To show that in spite of the challenges, reliable classification is possible.

Figure 1.1 presents a classification system structure by Duda et al. [33]. The contributions of this thesis are related to the parts inside the red rectangle.

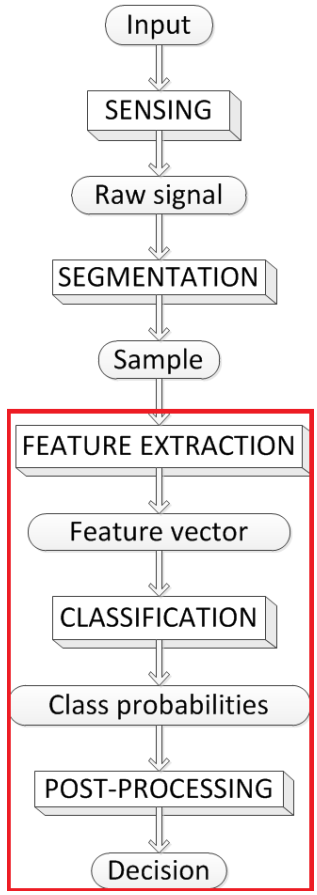

Figure 1.1: The structure of a classification system, as presented by Duda et al. [33]. The contributions of this thesis are related to the parts inside the red rectangle. The rectangles with capitalized text represent processes, whereas the rounded rectangles represent information or data.

1.3 Scope

The electromagnetic phenomena and interactions between concealed metallic items and the measurement system are complex. Therefore, it is not feasible with practical applications, such as the walk-through metal detection presented here, to aim at their accurate modeling. Consequently, this thesis has adopted an engineering approach. The background theory is kept simple: it is a coarse approximation of reality yet based on well-founded theoretical evidence found in the literature. Chapter 2 briefly presents the underlying physics and the approximation used; thereafter, the simple approximation is used.

Although in a real-life WTMD scenario the number of metallic items is unknown, in this thesis the problem scope is narrowed down to a situation in which only one metallic item is carried through the portal at a time. However, the methods and results presented in this thesis can be generalized into a multi-object scenario if the SNR and the resolution of the measurement system are good enough. In Section 5.7, references are made to literature that could be used for extending the system to handle multiple targets simultaneously.

Furthermore, the portal operation in this work is such that each coil works at a distinct single frequency, as opposed to a situation in which information on a wide frequency band can be obtained. In this thesis, the object is characterized by using a magnetic dipole model, and the limitations of the model may, in theory, affect the applicability of the results.

1.4 Publications and author's contribution

This thesis is based on five publications. The role of each publication is clarified in Chapter 5. In four of them (Publications I, II, IV, and V), the author was the main author and mainly responsible for producing them. Furthermore, the author collected practically all the walk-through scan data.

The author designed the experiments for Publications I and II with Dr. Marsh and Prof. Anthony Peyton. The manuscript of Publication I was written in cooperation with Dr. Marsh. The manuscript of Publication II was written mainly by the author. The author also conducted the experiments for publications I and II.

The main author of Publication III was Dr. Liam Marsh. The walk-through scans for the study were performed by several candidates (including Dr. Marsh and the author). The author planned the study in cooperation with Dr. Marsh and assisted in the experiments and in writing the manuscript.

The experiments for publications IV and V were planned with Dr. Juho Vihonen and Dr. Marsh and performed by the author with some assistance from Dr. Marsh. The manuscripts were written by the author with some assistance from Dr. Vihonen and Dr. Marsh.

The comments and feedback from the other authors were important and helpful in writing all the papers.

1.5 Outline of the thesis

This thesis is comprised of six chapters.

Chapter 1 introduces the field of metal detection and security screening. The background and motivation for the study are given, followed by the objectives, research methods, restrictions and contributions of the thesis.

Chapter 2 presents some background theory of EMI metal detection and characterization of metallic objects.

Chapter 3 presents the measurement system used in this thesis and explains how estimates of the magnetic polarisability tensor and the trajectory of the object are calculated.

Chapter 4 presents the main problems about the classification of metallic items using EMI data.

Chapter 5 discusses the contributions of this thesis in terms of its objectives in Section 1.2. Furthermore, generalization of the results is considered.

Chapter 6 concludes the thesis.

2 Electromagnetic induction spectroscopy

This chapter provides information about the basic principles of electromagnetic induction and how it can be used to classify metallic objects. This information is crucial for understanding the design of the measurement system in Chapter 3, and the phenomena observed in the experiments described in Chapter 5.

Section 2.1 provides information about the electromagnetic (EM) properties of metallic objects and how metallic objects can be detected and subsequently characterized using EMI. Section 2.2 explains the principle of the dipole model and how it is used to describe metallic objects. Section 2.3 presents parametric models for EMI characterization; i.e., how EMI responses can be parametrized using a physical model. Finally, Section 2.4 provides information about alternative physical models that tackle the drawbacks of the dipole model.

2.1 Detection and characterization of metallic objects

Many kinds of metals, such as iron, aluminium, copper, magnesium, chromium, and even gold, are used in common objects that might be carried through a WTMD portal. Each metal has its characteristic EM properties that arise from its chemical structure. However, objects are usually made of alloys instead of pure metals. Alloys are mixtures of metals that consist of several components in specific ratios. Hence, each alloy has its characteristic EM properties depending on its components. Furthermore, these properties might change according to how the alloy is manufactured, e.g., as a result of heat treatment and plating.

The most important EM properties are *conductivity* and *permeability*. Conductivity describes the capability of the material to conduct an electric current. The SI unit for conductivity is *Siemens per metre (S/m)*, and it is often denoted by the symbol σ. Permeability describes the magnetic behaviour of a material. The SI unit for permeability is *Henry per metre (H/m)*, but it can be also given as *relative permeability*, as explained in Table 2.1.

Among the most common alloys in everyday items are different types of steel, each of which is designed for a specific purpose. For example, *AISI/304 stainless steel*, one of the most common types of stainless steel, is non-magnetic and may contain a variety of metals, including iron, chromium, nickel, and manganese [34]. Table 2.1 lists some approximate EM properties of common materials.

Everyday objects may consist of several distinct metallic parts, i.e., be *heterogeneous* in terms of their metal content. For example, the blades, casing, and screws of a Swiss army

Table 2.1: Approximate EM properties of some pure metals and alloys. Permeability is given as relative permeability $\mu_R = \mu/\mu_0$ where μ_0 is the vacuum permeability. The values in the table are for representative purposes only. True values depend on a variety of factors, and can differ significantly. See [35–37] for reference.

Metal type	**Conductivity σ (MS/m)**	**Rel. permeability μ_R**	**Class**
Aluminium	36.9	1.000022	Paramagnetic
Brass	15.9	1.01	Paramagnetic
Carbon steel	5.9	100	Ferromagnetic
Copper	58.5	0.999994	Diamagnetic
Gold	44.2	0.99996	Diamagnetic
Iron	10.1	200 ... 4000	Ferromagnetic
Magnetic steel	1.4	1000 ... 1800	Ferromagnetic
Nickel	14.3	100 ... 600	Ferromagnetic
Silver	62.1	0.99998	Diamagnetic
Stainless steel	1.36	1.02	Paramagnetic
Zinc	16.6	<1	Diamagnetic

knife may all be made of different alloys. Moreover, the distinct parts can be welded, glued, or joined with metallic or non-metallic screws, affecting the EM properties of the object. The EMI response of heterogeneous objects is hard to model due to, e.g., the magnetic coupling between the parts.

EMI-based metal detection is based on exploiting the fact that metallic objects cause a change in a magnetic field, and that this change depends on the *intrinsic properties* of the object, such as size, shape, permeability, and conductivity. In an EMI-based metal detection system, a *primary magnetic field* is generated by feeding a current into the *transmit coil*. A metallic object in the primary field will alter the field, and this change can be detected at *the receive coil* (i.e., the *sensor*). Detected changes form the input signal of the system. This signal, in turn, contains information about the intrinsic properties of the object, enabling characterization and classification.

A metallic object alters the primary field by two principal mechanisms. In case of a permeable object, the magnitude of the primary field is amplified, while its phase remains unchanged. However, if the object is conductive, eddy currents are induced in it. This, in turn, generates a secondary magnetic field which interacts with the primary field, altering its signal phase and weakening its magnitude.

The above principle is simple and easy to understand. However, in reality, magnetic and electric interactions between the coils and the target object are more complex and can be quantified using the Maxwell equations; see, e.g., [38]. Unfortunately, exact modeling of the interactions is often computationally challenging, and therefore, practical solutions must use some approximation. Hence, we assume that the target object is far away from the coils and small in size compared to the wavelength of the excited primary field. This assumption allows us to ignore the so-called displacement currents in the Maxwell equations. The resulting model is called the eddy current approximation [39]. Importantly, in order to keep calculations simple, we must assume that the target object does not change the excited primary magnetic field – which is clearly not true and produces a small model error in the calculations. For the remainder of this thesis, we use this approximation and deal with the model error later.

There are two main approaches to EMI-based metal detection, depending on the type of the input signal fed into the transmit coil. These are *pulsed excitation* EMI (also known

as *time-domain EMI* or *pulsed EMI*) and CW EMI. In pulsed EMI, a pulse signal is fed into the transmit coil, whereas in CW EMI, the input signal is a continuous sinusoidal wave.

Pulsed EMI was not used for the experiments of this thesis. However, a large part of the literature on the characterization and classification of metallic objects using EMI has been produced using the technique. Therefore, it is covered for the sake of completeness. Moreover, many of the methods presented in this thesis may be directly applied to portals that use pulsed EMI. Furthermore, the methods may apply to fields such as humanitarian demining where pulsed EMI is commonly used.

In the pulsed EMI method, as the input current vanishes due to pulsed operation, the primary field decays, which in turn causes the secondary field to collapse. The changes in the decaying primary signal can be detected at the receive coil. The characteristics of this signal change (the *decay signature*) are dependent on the shape, size and EM properties of the object.

In turn, in CW EMI, the changes caused by a metallic item can be seen directly at the receive coil as a phase and magnitude difference between the transmitter and receiver, and the input signal of the CW system (for a single coil pair) is given by

$$f(\omega) = \Re(f(\omega)) + \Im(f(\omega)) = \mathbf{R}(\omega) + \mathbf{jQ}(\omega), \tag{2.1}$$

where ω is the angular frequency, $\mathbf{j}$ is the imaginary unit, $\mathbf{R}(\omega)$ is the frequency-dependent real ($\Re$) component, and $\mathbf{Q}(\omega)$ the frequency-dependent imaginary ($\Im$) component [40, 41]. The real (*in-phase*) part is in phase with the primary field, and the imaginary (*quadrature*) part is 90° out of phase with the primary field [41]. It should be noted that here the labeling of real and imaginary components is arbitrary, and that the signals could as well be named the other way around. For conductive, non-magnetic metals, such as copper and aluminium, $\mathbf{R}(\omega)$ should always take positive values, whereas for ferrous metals, $\mathbf{R}(\omega)$ should be negative at low frequencies [42]. Such heuristic information may be exploited in metal classification.

Because CW EMI methods work at predefined discrete frequencies, they are subject to noise only at them. Hence, the systems can operate at a much higher SNR than pulsed EMI systems [43]. On the other hand, pulsed EMI methods allow use of a much wider range of frequencies, and hence receive potentially more information on the characteristics of the object. However, yielding acceptable SNR is challenging due to its more difficult filtering of noise.

2.2 Dipole model

The measured input signal of an EMI system is often not useful as a *raw signal* for characterization and classification purposes. Storing such a large amount of data is not feasible, and computational complexity of data processing is high. Therefore, a variety of models have been proposed to parametrize EMI responses. For example, Williams et al. [44] have used a bivariate Gaussian model, whereas Tran et al. [45] have proposed the use of *Daubechies Wavelets*. These methods, however, do not exploit the existing prior knowledge on the underlying physics that causes the EMI responses.

Motivated by applications such as landmine and UXO detection, physics-based modeling of the EMI response of metallic objects has been studied for decades. Chesney et al. [46] were the first to properly address object characterization and classification using a pulsed

EMI response. They found that, e.g., the shape and amplitude of EMI responses behave differently as a function of orientation with aluminium and steel objects.

Defining a generic analytical model for the EMI response of an arbitrary metallic object is extremely difficult, if not impossible. However, analytical solutions exist for the response of a sphere, cylinder, spheroids [47], and arbitrary bodies-of-revolution [48]. Also, Sebak et al. [49] have presented an integral equation for modeling the EMI scattering of a homogeneous, permeable, and conductive object of arbitrary shape. However, these models are, owing to computational limitations, mostly prohibitively complex to use in real world applications. Moreover, there exists a wide range of metallic objects that are neither spherical nor axisymmetric. Therefore, a variety of simplistic physical EMI response models have been developed, of which the *dipole model* is perhaps the most commonly used.

The dipole model presents the target as an infinitesimally small point [1] source [50], i.e., a set of colocated dipoles that scatter the primary magnetic field. The scattering caused by the target is parametrized using the magnetic polarisability tensor, also known in the literature as the magnetic polarisability *dyadic* [51], which essentially defines how the target modifies the field vector values $\mathbf{H}_\mathrm{t}$ and $\mathbf{H}_\mathrm{r}$ (i.e., *H-fields*) of the primary magnetic field in each main axis, namely X, Y, and Z in a three-dimensional (3D) space. A relation exists between the measured signal, the H-fields and the MPT; it can be stated in terms of the voltage induced in the receive coil, and according to Abdel-Rehim et al. [52], be written as

$$V_{ind} = \eta \cdot \mathbf{H}_\mathrm{t}^T \overleftrightarrow{\mathbf{M}} \mathbf{H}_\mathrm{r}, \tag{2.2}$$

where $\eta = \frac{\mathbf{j}\omega\mu_0}{I_R}$, μ_0 is the permeability of free space, $\mathbf{j}\omega$ is the phase angle component, and I_R is the electric current present in the receive coil. Field vectors $\mathbf{H}_\mathrm{t}$ and $\mathbf{H}_\mathrm{r}$ are three-dimensional so that $\mathbf{H} = [H_X\ H_Y\ H_Z]$. The H-fields of any known coils can be analytically solved by using the *Biot-Savart -law* [53]. Because the field vectors are 3D, the MPT is a 3-by-3 matrix. For a CW EMI system, the values of the MPT are complex because the object changes the magnitude and the phase angle of the input signal; i.e., there is a frequency-dependent phase shift between the primary and secondary fields [40, 41], as described in Section 2.1. Hence, the magnetic polarisability tensor $\overleftrightarrow{\mathbf{M}}$ at the excitation frequency ω is given by (see, e.g., Norton et al. [54])

$$\overleftrightarrow{\mathbf{M}}(\omega) = \begin{bmatrix} m_{X,X}(\omega) & m_{X,Y}(\omega) & m_{X,Z}(\omega) \\ m_{Y,X}(\omega) & m_{Y,Y}(\omega) & m_{Y,Z}(\omega) \\ m_{Z,X}(\omega) & m_{Z,Y}(\omega) & m_{Z,Z}(\omega) \end{bmatrix}. \tag{2.3}$$

Moreover, it is symmetric such that $m_{X,Y} = m_{Y,X}$, $m_{X,Z} = m_{Z,X}$, and $m_{Y,Z} = m_{Z,Y}$. Hence, there are six unknown components, and if complexity is taken into account, there are 12 unknown terms. The MPT values are functions of the frequency ω and depend on the size, shape, and EM properties of the object. Similarly, the MPT exists for a pulsed EMI system response. The dyadic is similar, but its elements, i.e., the descriptors of the scattering, are functions of time instead of frequency. Hence, the time-domain MPT

[1] To be precise, the target is not assumed to be a point because then it would have no shape; such an assumption would invalidate what we want to achieve by using the model. Instead, the approximation is asymptotic in the size of the object (assuming a fixed shape) going to zero, as pointed out by Prof. Bill Lionheart.

$\overleftrightarrow{\mathbf{M}}(t)$ is given by

$$\overleftrightarrow{\mathbf{M}}(t) = \begin{bmatrix} m_{X,X}(t) & m_{X,Y}(t) & m_{X,Z}(t) \\ m_{Y,X}(t) & m_{Y,Y}(t) & m_{Y,Z}(t) \\ m_{Z,X}(t) & m_{Z,Y}(t) & m_{Z,Z}(t) \end{bmatrix}. \tag{2.4}$$

The above symmetry also applies to the time-domain MPT.

The 3-by-3 matrix MPT representation is called the *rank 2 tensor* and it is well understood and mathematically proven in the magnetostatic case (i.e., permeable objects only, see, e.g., [55] for details); Osborn [56] calculated the demagnetization factors of the general ellipsoid already in 1945. For a long time, its use for the eddy current approximation case (e.g., Norton et al. [54]) remained mathematically unproven. Recently, this conventional view of representing the MPT has been challenged by Ammari et al. [57], who claim that a rank 4 tensor is necessary, resulting in a total of 81 unknown terms in the matrix. These terms would be significantly more challenging to solve. However, Ledger and Lionheart [58] show that the conventional rank 2 tensor is indeed enough to characterize an object. Hence, the theory behind the MPT is well established, and theoretical values for rotationally symmetric objects such as cylinders, have been presented [59]. Baum [60] has shown that the MPT can be used to represent nonsymmetric objects, and hence six unknowns in the MPT matrix, as shown in (2.3), are necessary.

The eigenvalues $\boldsymbol{\lambda}$ of the MPT $\overleftrightarrow{\mathbf{M}}$ are given by a vector (*eigenvalue vector* or *triplet*) of three complex values

$$\boldsymbol{\lambda}(\overleftrightarrow{\mathbf{M}}) = \boldsymbol{\lambda} = [\lambda_1 \ \lambda_2 \ \lambda_3]. \tag{2.5}$$

They are a rotation invariant representation of the MPT, as shown in Publication II. Depending on the type of the MPT, the eigenvalues are either a function of frequency or time. Figures 2.1 [61] and 2.2 [61] show the frequency response of the MPT eigenvalues for a steel cylinder in two distinct orientations. Clearly, the frequency dependency of the eigenvalues, and consequently the MPT, is significant.

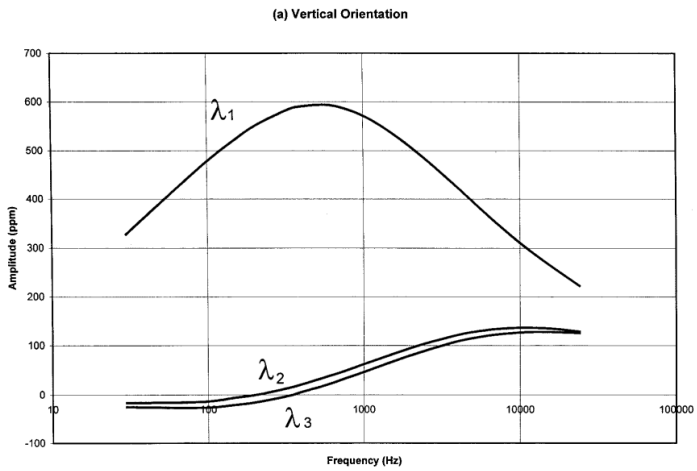

Figure 2.1: Frequency response of MPT eigenvalues of a steel cylinder, vertical orientation (from Norton et al. [61] ©2001 IEEE).

The dipole model is a coarse approximation that has been used because of its simplicity and subsequent low computational cost. Moreover, it has been shown by Bell et al. [62]

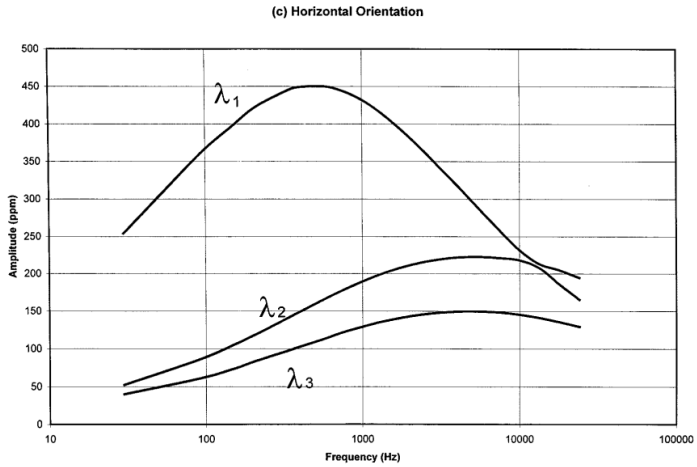

Figure 2.2: Frequency response of MPT eigenvalues of a steel cylinder, horizontal orientation (from Norton et al. [61] ©2001 IEEE).

that the dipole model works well enough for modeling the response for a variety of objects. However, the simplification comes at a cost; the dipole model is subject to limitations and assumptions. In addition to assuming that the target is an infinitesimally small point, or at least materially homogeneous, the dipole model assumes that the excited primary field is essentially uniform through the volume of the target. [2] Smith and Morrison [63] have shown that if the distance from the sensor to the target is much greater than the size of the target, the dipole model yields a very good approximation of the secondary magnetic field caused by the object. However, real objects are finite in size, and real coils generate non-uniform fields; therefore, the above assumptions are not valid [62]. Furthermore, the dipole model is not suitable for modeling objects that are positioned close to the sensor, and it cannot represent the complexities of heterogeneous objects [62, 64]. Consequently, the simplifications cause the model to break down with realistic data [50, 65], introducing an element of model error into the estimated parameters. Bell et al. [62] have shown that the eigenvalues of a steel rod change significantly as a function of orientation and distance from the coils. Far away from the coils the results are acceptable, but close to the coils the approximation breaks down. The authors state that this is due to the fact that large variations occur close to the coils in both direction and strength in the primary field over the length of the bar. Hence, they claim that a single set of eigenvalues obviously cannot fully represent an EMI response.

2.3 Parametric models for EMI response presentation

This section focuses on the parametrization of the dipole model, i.e., the MPT and in particular its eigenvalues. The literature offers a variety of options for representing them. Finding these unknown parameter values based on measured EMI data is an inverse problem, which can be solved by mathematical optimization. However, such

[2] As described above, the size of the object approaches zero asymptotically as the distance from the coils approaches infinity. This also to say that uniformity of the field values is not explicitly required; yet the accuracy of the model increases as the size of the object gets smaller.

inverse optimization algorithms are not covered here, but information about the possible algorithms is available in the literature for each parametric model.

The MPT eigenvalues essentially define the *transfer function* of the system formed by the input signal, the target object, and the output signal. For example, in a pulsed EMI system the eigenvalues can be thought to define the impulse response of the particular system. The transfer function can be defined using the *Laplace transform*. The so-called *poles and zeros* of the Laplace-space transfer function then essentially define the behaviour of the system. The Laplace transform space is also called the *complex frequency* plane as the poles are defined to be complex values $s = \sigma + \mathbf{j}\omega$. See, e.g., [66] for details.

Using this idea, Baum [67] introduced a methodology called the *singularity expansion method (SEM)* to represent the EMI response of conductive metallic targets, independent of the exciting signal waveform, in terms of singularities in the Laplace transform plane [68]. In particular, according to Baum, the Laplace-plane poles represent complex *natural frequencies* of the target, and reveal its intrinsic properties. According to the established theory, a low-frequency EMI response of highly conducting, permeable objects can be characterized by natural (complex Laplace-plane) frequencies that are real and negative [51, 69]. Geng et al. [70] provide a thorough explanation of the theory and show that each eigenvalue λ_i can be modeled as a sum of N Laplace-plane poles, given by

$$\lambda(s) = \sum_{n=1}^{N} \frac{A_n}{s - \zeta_n}, \tag{2.6}$$

where A_n is the nth expansion coefficient, and ζ_n is the nth pole. Note that the notation here is altered from the original version given by Geng et al. [70]. According to the authors, one or two of these poles are usually necessary to represent the measured response, whereas Riggs et al. [69] state that most EMI responses of (conductive) objects can be characterized by only two or three poles. For example, Tarokh et al. [71] have used this approach to represent the MPT eigenvalues of CW EMI data. Similarly, Carin et al. [59] have modeled the pulsed EMI response of finite length metallic cylinders and rings by using two or three poles, and state that the approach can also be applied to general rotationally symmetric targets.

Additionally, real and negative poles, according to the theory [66], correspond to damped exponentials that define how the signal decays as a function of time. According to Baum, the response can be represented as a sum of damped exponentials or exponentially decreasing sinusoids [67]. Therefore, the two representations are equivalent. The time-dependent decay of the receive coil signal is of special interest for pulsed EMI systems. Hence, a common approach in the literature (see, e.g., Baum [51] and Collins et al. [72]) has been to model the time-domain EMI response of a permeable, conducting target as a sum of damped exponentials, given by

$$\lambda_i(t) = \sum_{n=1}^{N} A_n e^{-\alpha_n t}, \tag{2.7}$$

where A_n is an amplitude factor that depends on the size of the target and on its distance from the sensor, and α_n is a decay parameter [51, 72]. Similarly, Pasion and Oldenburg [73] argue that the time decay behaviour of dipoles along each axis, i.e., each eigenvalue, depends linearly on

$$\lambda_i(t) = \kappa_i(t + \alpha_i)^{-\psi_i} e^{-t/\gamma_i}, \tag{2.8}$$

where κ_i, α_i, ψ_i, and γ_i are the decay parameters, and their values depend on the size, shape, conductivity and permeability of the target object. The authors propose a nonlinear inversion process to be used for finding the parameter values [73]. As an example of this general approach, Geng et al. [70] have shown that a pulsed EMI response of conducting and permeable bodies of revolution (BoR) can be modeled as a sum of damped exponentials, and that the damping constants are strongly dependent on the shape, conductivity, and permeability of the target.

Modeling the wideband frequency response (*spectrum*) of an EMI signal has also been studied. For example, Gao et al. [43] have used a so-called *Method of Moments analysis* to model the EMI spectra of objects, assuming that they are BoR. The benefit of knowing the EMI spectrum is that different frequencies reveal distinct characteristics of the objects. For example, Chilaka et al. [74] state that discrimination of thick-walled and thin-walled ferrous cylinders necessitates the use of low frequencies (< 30 Hz). Above these frequencies, wall thickness does not affect the response and distinct cylinders look almost identical [74].

Furthermore, Miller et al. [48] have proposed three parametric models to estimate the EMI spectra of different types of objects. The models are based on analytical solutions found in the literature, namely for a sphere, a cylinder, and multiple conducting loops. The proposed three-parameter model is for permeable spheres and cylinders, the four-parameter version for wire loops, and the five-parameter version for complex targets. Their results show that the EMI response of most targets can be modeled accurately by using only a few parameters. Furthermore, Bell et al. [62] state that the four-parameter model can be used to successfully present the frequency domain EMI response of a variety of compact objects. The model is given by

$$f(\omega) = \mathbf{R}(\omega) + \mathbf{jQ}(\omega) = A\{s + \frac{(\mathbf{j}\omega\upsilon)^{\varsigma} - 2}{(\mathbf{j}\omega\upsilon)^{\varsigma} + 1}\}, \tag{2.9}$$

where ω is the frequency, A is an amplitude, υ is a response time constant, and where ς determines the width of the response spectrum, and s is a factor controlling the relative magnitudes of response asymptotes at low and high frequencies [62]. Recently, to enable faster inversion, this model has been reduced to a two-parameter version by Ramachandran et al. [75] by using a gradient angle model.

A somewhat similar approach, the *discrete spectrum of relaxation frequencies (DSRF)* (see, e.g., studies by Wei et al. [76, 77]) is a model that describes the EMI spectrum of an object as a discrete set of pairs $\{\zeta_K, c_K\}$, where $\zeta_k = 1/\tau_k$ is a relaxation frequency, and τ_k is the corresponding relaxation time, and c_k is the amplitude related to the corresponding frequency. These pairs define the frequency bins of the spectrum. The spectrum can be solved analytically for basic shapes such as spheres and cylinders. The relaxation frequencies are position and rotation invariant, but the amplitudes are not. The DSRF contains information about the shape, size, orientation, permeability, and conductivity of the object, and using it, the frequency spectrum of an EMI signal can be presented by

$$\Psi(\omega) = c_0 + \sum_{n=1}^{N} \frac{c_n}{1 + \mathbf{j}\omega/\zeta_n}, \tag{2.10}$$

where c_0 is a shift term, N is the number of relaxations, i.e., the model order, c_n are the real spectral amplitudes, and ζ_n the relaxation frequencies. Wei et al. [76, 77] have provided methods for estimating the DSRF parameters. Furthermore, Tantum et al. [78]

have used a *structured Relevance Vector Machine (sRVM)* to find the DSRF spectrum for an object using CW EMI at 21 distinct frequencies. The idea is that the sRVM assigns weights for each frequency, based on their importance, and most of them will converge to zero [79]. Scott and Larson [80] have presented DSRF-representations for several small objects, and Krueger et al. [81] have used a dictionary of DSRF responses to determine the location and orientation of unknown buried targets.

2.4 Extensions of the dipole model and representing heterogeneous objects

As discussed above, the dipole model is a coarse approximation with several weaknesses. According to Shubitidze et al. [82], the validity of the dipole model is often compromised in case of heterogeneous objects, causing a certain degree of model error, as also discussed in Section 2.2. Unfortunately, many common items are heterogeneous, i.e., contain a variety of metal alloys and consist of distinct parts. Consequently, several approaches have been proposed for extending the dipole model to accommodate real objects in a better way.

Zhang et al. [83] have extended the dipole model to allow for targets of complex shapes, namely UXO. Thus the object is represented by multiple sets of dipoles, each set assigned to distinct physical locations within the target. This arrangement accommodates heterogeneous objects, though it does not take into account the magnetic coupling between object parts [83]. Moreover, Braunisch et al. [84] have used the dipole model to present the EMI response of a collection of small (conducting and permeable) objects, while trying to take their mutual interactions into account. This can be seen as an attempt to understand the EM behaviour of heterogeneous objects. Nevertheless, Shubitidze et al. [82] claim that a model using several dipoles to simulate a heterogeneous target cannot accurately represent a true EMI response because such an approach does not take magnetic coupling into account. They have studied the EMI-responses of various heterogeneous metallic objects. The main issues of concern are, first, coupling between the distinct parts of the object, and second, close proximity issues that change the characteristics of the response, i.e., its spectrum, significantly when the object is close to the coils. They propose a hybrid model for heterogeneous targets, and show that it can represent the response of certain heterogeneous objects more accurately than the dipole model [82].

Shubitidze et al. have also proposed two generalized dipole models, namely the *normalized surface magnetic source* (NSMS) model [85] and the *orthonormalized volume magnetic source* (ONVMS) model [65]. The NSMS model associates the object with a prolate spheroid that is composed of radially oriented dipoles. Hence, the total scattered magnetic field is approximated as a sum of all the magnetic fields that have been radiated by these dipoles. The authors demonstrate by measurements that the NSMS is more robust than the dipole model [85]. The ONVMS, on the other hand, associates the measured response with a set of magnetic dipole sources that, instead of a single point, are distributed over the volume that the primary magnetic field interrogates. The model tackles the problems of the simple dipole model by allowing for heterogeneous objects, significant variations of magnetic fields, and even multiple objects with overlapping signals. By definition, the ONVMS does not contain more information than the dipole model, but the quality of its information is better, especially in the presence of noise, complex targets, and overlapping target signatures [65]. The ONVMS has been shown by Bijamov et al. [86] to outperform the dipole model and perform well in a variety of field tests to detect UXO.

Apart from the different versions of the dipole model, other approaches have been introduced. Grzegorczyk et al. [87] have modeled highly permeable and conductive objects as ellipsoids, as opposed to bodies of revolution. Zhang et al. [64], on the other hand, have modeled metallic objects as homogeneous spheroids of arbitrary shape, size, permeability, and conductivity. Furthermore, they state that spheroids can accurately represent the responses of homogeneous, irregular objects, and that even many types of heterogeneous objects might be modeled by using two or more spheroids. The parameters of their proposed model are rotation and position invariant, and characterize the physical properties of the object, enabling classification. However, since the estimated parameter values are not directly related to the intrinsic parameters of the object, intelligent classification algorithms are necessary [64].

3 WTMD measurement system

This chapter presents the measurement system, referred to as *the portal*, used in this thesis, and it covers the part of the system flowchart shown in Figure 3.1. The input for this subsystem is a single walk-through scan, whereas its output is the solution $\boldsymbol{\beta}$ consisting of an estimate for the MPT matrix ($\widehat{\mathbf{M}}$) and an estimate of the trajectory of the object in the XYZ-space ($\hat{\mathbf{P}}$).

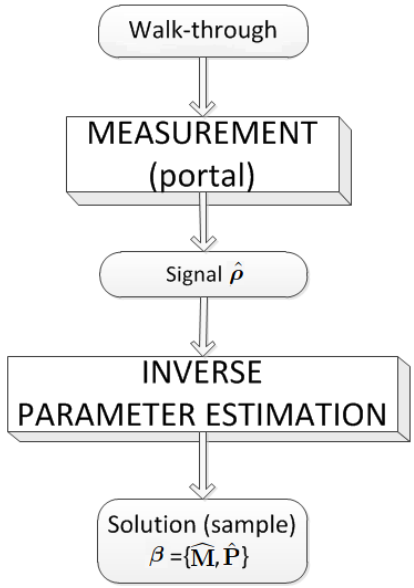

Figure 3.1: The scope of Chapter 3 as a flowchart.

The methods reported in this thesis are not dependent on the portal. Any WTMD system design that is capable of consistently estimating the MPT (see Section 2.2) of the unknown object can be used. In addition, some methods require a capability to estimate the trajectory of the unknown object.

3.1 Sensors, sensing and segmentation

Years of research and cooperation between Tampere University of Technology (TUT), Finland, Rapiscan Systems, and the University of Manchester, United Kingdom (UK), culminated in the development of a WTMD portal technology capable of reliably estimating the MPT of a target object. Initially, the ideas were tested at TUT using a prototype

system (see Kauppila et al. [26]). The system was built from a classification point of view, and hence the main focus was to estimate the MPT of the target without having to accurately position the target object based on EMI data. This estimation was achieved by using a custom six-coil geometry design that produced uniform magnetic fields in three dimensions across the detection space. The design greatly simplified the recontruction of the MPT (2.3). However, mainly because of the coil design, the so-called *body effect* (see Section 5.1) soon proved problematic in the early prototype. This meant that the signal caused by the human body often dominated the target object signal.

Later, a more sophisticated prototype WTMD measurement system (the portal) was built at the University of Manchester. Various papers have been published on the portal (see, e.g., the publications by Marsh et al. [88, 89]). Figure 3.2 shows the portal structure along with definitions of coordinate axes, namely X, Y, and Z. The X-axis denotes the walking direction. Thus, when a person walks through the portal, the transmit coils will be on the left-hand side and the receive coils on the right-hand side. The portal volume is 0.75 metres (m) × 2.05 m × 0.83 m (X × Y × Z). The overall design of the portal is similar to that of the professionally built, official devices used at airports.

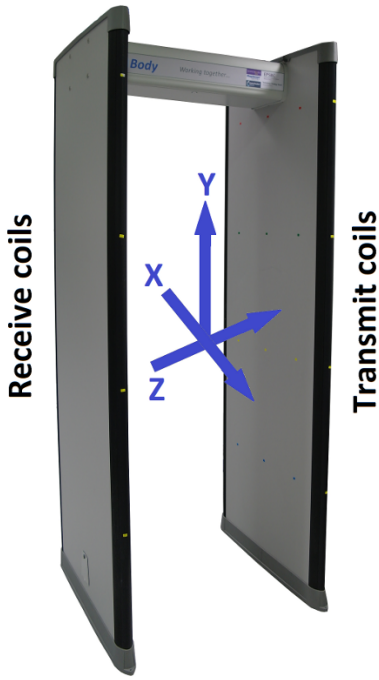

Figure 3.2: The portal. The coordinate axes used throughout this thesis are marked, along with the transmit and receive coils. (Modified from Publication II) ©2014 IOP Publishing. Reproduced with permission. All rights reserved.

The portal uses a total of 16 coils. Its coil geometry is shown in Figure 3.3(a) (from Marsh et al. [89]). There are eight transmit coils in one side panel, and eight receive coils in the other. The corresponding transmitters and receivers are not aligned with each other, but instead they are placed at different heights, except for the lowest pair. In addition, the coils on each side overlap slightly. The coils are so-called *gradiometer coils*,

as shown in Figure 3.3(b) (from Marsh et al. [89]). Their design cancels out the effect of the so-called far field, increasing the SNR of the system.

The system uses CW excitation by way of a single frequency for each coil pair, as opposed to systems described in, e.g., the landmine detection literature, which often use multi-frequency excitation. All transmitters operate at distinct frequencies, ranging from around 8 kHz to 14 kHz, to allow distinguishing of the signals from each other, i.e., to eliminate crosstalk. The width of the frequency bands is approximately from 500 Hz to 1 kHz.

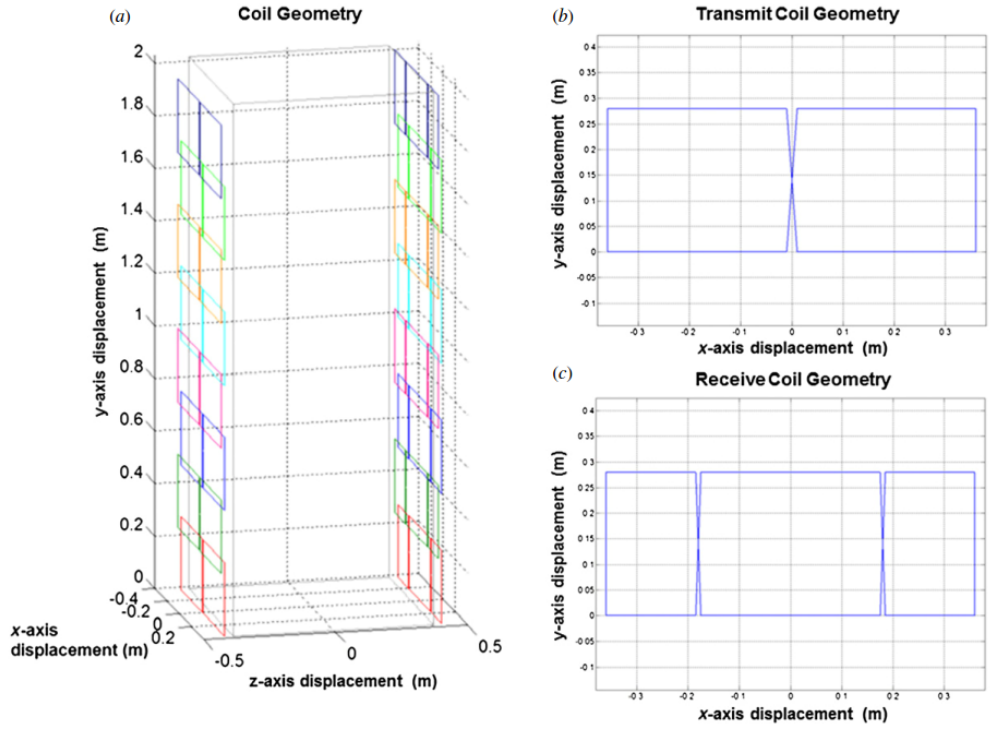

Figure 3.3: EMBody portal coil configuration (From Marsh et al. [89]) ©2013 IOP Publishing. Reproduced with permission. All rights reserved.

The system produces measurements at a rate of 100 Hz. Each measurement sample, for practical reasons such as limitations of SNR, contains data from 34 out of 8x8=64 possible coil combinations. The system output has been calibrated using a magnetic, non-conductive ferrite sphere so that each coil pair produces a roughly equal response in terms of amplitude.

The system has an adjustable triggering threshold that defines the change in a coil pair signal required to trigger the portal. If a large enough response is measured, the portal will record data before and after the trigger point. If the threshold is met at time $T_{triggered}$, the system captures one second of data between $[T_{triggered} - 0.5s \ldots T_{triggered} + 0.5s]$. Figure 3.4 demonstrates this for one coil pair. The measured input signal consists of an in-phase and a quadrature part, as described in (2.1).

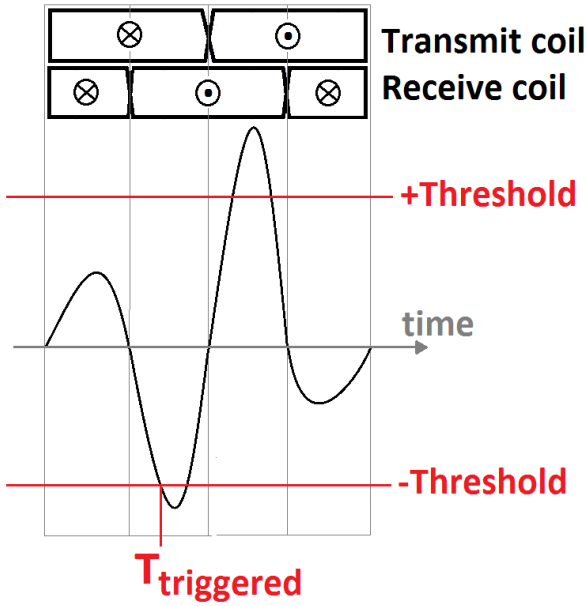

Figure 3.4: The portal is triggered when the signal for one coil pair exceeds the triggering threshold. One second of data is recorded, half a second before $T_{triggered}$, and half a second after. The signal owes its shape to the arrangement of the gradiometer coils. Note that this picture is for illustration purposes only and does not represent real data.

3.2 Feature extraction: Applying the dipole model

In order to classify the detected target object, it is crucial to obtain information on its characteristics, namely its material and dimensions. For this purpose, the object must be characterized by applying a model to measured data. The dipole model (as described in Section 2.2) is used to model the WTMD portal data because it provides a reasonable approximation of the object while its simplicity enables real-time data processing.

As presented in Section 2.1, permeability and conductivity, along with the size and shape of the object, determine how it interacts with the excited primary magnetic field. Figure 3.5 shows an overview of these changes. A magnetic object, i.e., an object with considerable permeability, amplifies the magnitude of the primary field (see Figure 3.5(a)). On the other hand, in case of a conductive object, eddy currents are induced in it, thus creating a secondary magnetic field. This secondary field will interact with the primary field, affecting its phase and magnitude. The effect on magnitude will be opposite to the primary field, i.e., it will be weakened. A highly conductive object will have a significant effect on both the phase and the magnitude of the primary field. This is demonstrated in Figure 3.5(b). The phase and magnitude of this change depend on the frequency of the excited signal. On the other hand, as shown in Figure 3.5(c), an object with low conductivity will have only a relatively small effect on the phase of the primary field. In practice, many objects that are carried through WTMD portals are both conductive and magnetic, so the above effects are often mixed.

The system can be described with the dipole model by introducing, at each location in the XYZ-space within the portal, a relation between the measured signal, the receive and

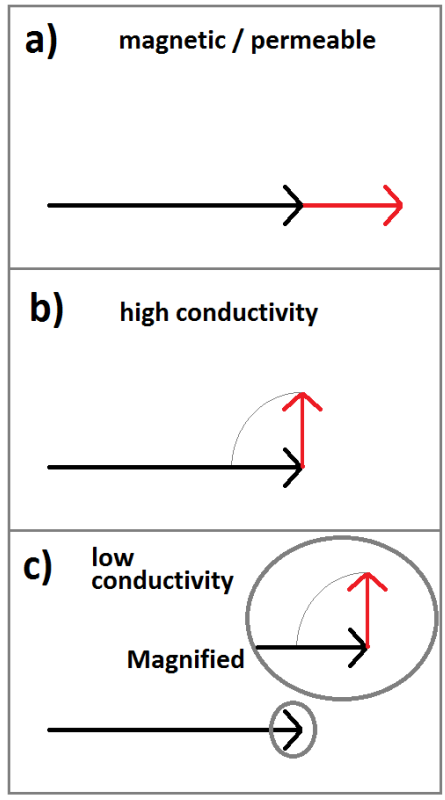

Figure 3.5: The effect of different kinds of materials on the primary magnetic field.

transmit H-fields, and the MPT of the unknown object (see (2.2)). This is given by

$$\rho(\mathbf{p}, \overleftrightarrow{\mathbf{M}}) = \mathbf{H}_{\mathrm{t}}^{T}(\mathbf{p})\, \overleftrightarrow{\mathbf{M}}\, \mathbf{H}_{\mathrm{r}}(\mathbf{p}), \tag{3.1}$$

where $\mathbf{H}_{\mathrm{t}}$ and $\mathbf{H}_{\mathrm{r}}$ are the transmitter and receiver coil magnetic field vectors, respectively, $\mathbf{p} = [X\ Y\ Z]^T$ is the object centre position vector, and $\overleftrightarrow{\mathbf{M}}$ is the MPT of the object. The elements of the MPT matrix $\overleftrightarrow{\mathbf{M}}$ are complex values ($m_{i,j} = \Re(m_{i,j}) + \mathbf{j}\,\Im(m_{i,j})$) due to the presence of in-phase and quadrature signals, as explained in Section 2.2. However, the elements are not defined to change as a function of frequency because the system is defined to use a single frequency at around 10 kHz. As described earlier, this is not exactly true as each transmit coil has its own designated frequency band.

Marsh et al. [89] have presented examples of MPT values for various kinds of objects (Figure 3.6 (from [89])). For a magnetic spherical object (Figure 3.6(a)), the diagonal values should all be the same. A magnetic, infinitely thin rod aligned with one axis of the system should have a nonzero value for only one diagonal element (Figure 3.6(b)). The depicted MPT indicates that only the Y-components of the H-field vectors affect the output signal. However, if the rod is even slightly rotated, the MPT values change as other components of the H-field vectors are affected. Similarly, for a magnetic disc aligned along the YZ-plane, the MPT matrix should be as shown in Figure 3.6(c). On the other hand, for non-magnetic objects, owing to the physical facts described earlier in

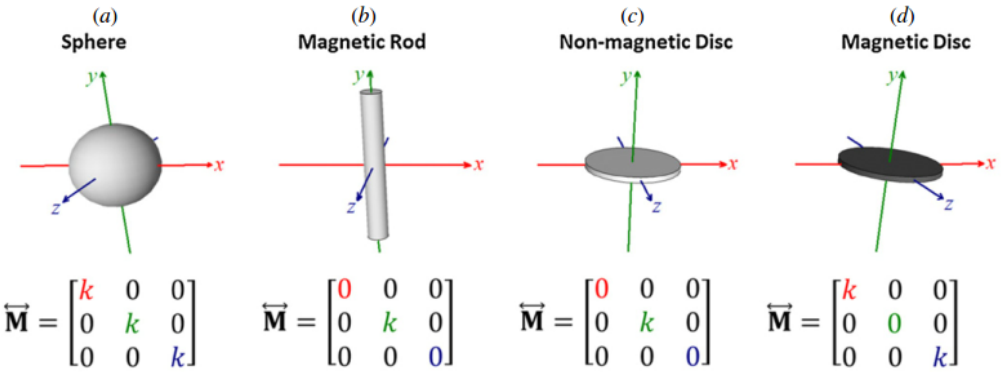

Figure 3.6: Examples of MPT values for some objects (from Marsh et al. [89]). Here the parameter k is an arbitrary constant term representing the magnitude of the element. ©2013 IOP Publishing. Reproduced with permission. All rights reserved.

this thesis, the tensor is different, as shown in Figure 3.6(d). However, as demonstrated in Figure 3.5, the conductivity of the object plays a large role in this case and hence the MPT values depend on the excitation frequency of the system.

3.3 Target MPT and trajectory estimation

The geometry of a coil determines the shape of the magnetic field it creates. For metallic object detection and characterization, the direction of the magnetic field vectors is crucial because the technique is based on detecting changes in the excited primary magnetic field. The target object affects the field vectors differently depending on their orientation in relation to the object. Hence, the target object can be *seen* by the detector solely from the directions of the field vectors. Indeed, to estimate the MPT for the object, it is essential that the magnetic field sees the object from as many directions as possible [61]. If the target is seen from one direction, only one linear combination of the MPT eigenvalues can be measured [62].

For example, a solenoid-based measurement system can be used to estimate the MPT for any object small enough to fit inside the solenoid. A solenoid is a coil that is formed by a helix of wire [90]. The magnetic field that it generates inside itself is strong and unidirectional along the length of the coil; i.e., the field vectors run parallel inside it, as demonstrated in Figure 3.7. Hence, with a solenoid, a metallic item can be seen from one direction at a time. While solenoids can be used to estimate the MPT for an object, measurements must be taken using several object orientations to capture enough information in all three dimensions.

When the exact position of the target object is known, the MPT for the target can be solved trivially as long as enough measurements are available from at least six views (corresponding the six unknowns in $\overleftrightarrow{\mathbf{M}}$) on the object (see Kauppila et al. [26]). Exactly six views are needed if they are selected optimally. However, in a WTMD scenario, the object trajectory, i.e., its position as a function of time, is unknown. Hence, it must be estimated simultaneously with the MPT parameters. It is not feasible to analyze all possible trajectories and all possible MPT parameter combinations to find an optimal solution. Hence, some heuristic knowledge must be used. It is known *a priori* that if

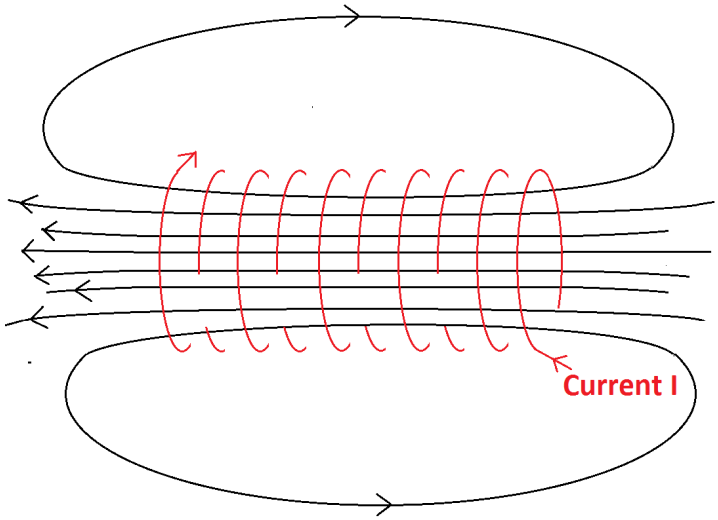

Figure 3.7: A solenoid creates a strong magnetic field in one direction. The wire is shown in red and the magnetic field vectors in black.

a person is carrying a concealed object through the portal, the trajectory of the object will be more or less a straight line at a slight angle in relation to the portal side panels, with any curvature resulting from the gait and movement of the arms (e.g., in case of a wristwatch) or legs/feet (e.g., a concealed knife near the ankle or shoe shank). Therefore, it is common sense to start off with an initial guess of the trajectory that is a straight line, i.e., that only the X-position changes as a function of time while Y and Z remain constant.

In the WTMD portal, the orientation of the unknown object cannot be controlled. However, during a walk-through, we assume that the object travels at a roughly constant orientation through the portal. Consequently, the orientation of the target changes slightly in relation to the field vectors as the object travels along the portal, as shown in Figure 3.8. Moreover, as all the coil combinations get an independent view on the object, enough measurements are made from a sufficient number of angles to get a good idea of how the object behaves in an EM sense. Finally, measurements are taken at a high rate of 100 Hz, enabling removal of noise by averaging.

The system response $\hat{\boldsymbol{\rho}}$ consists of a time series of measurements that are recorded of each walk-through scan. Normally, this is approximately one second of data, i.e., 100 measurement frames at 100 Hz. As the portal records data from 34 coil pairs, one second of walk-through scan data contains 100 frames $\times$ 34 coils pairs = 3400 measurement values.

A theoretical dipole model -based relationship between measurements and the MPT has been presented in (3.1). The transmitter and receiver coil magnetic field vectors $\mathbf{H}_\mathrm{t}$ and $\mathbf{H}_\mathrm{r}$ are known because they can be analytically solved. However, the object centre position vector $\mathbf{p}$ and the MPT $\overleftrightarrow{\mathbf{M}}$ are unknown. It is not possible to use analytical, straightforward methods to find $\overleftrightarrow{\mathbf{M}}$ and the series of estimated object positions $\widehat{\mathbf{p}}_i$, i.e., the *path* or *trajectory* of the object. Therefore, it is an inverse optimization problem to find them.

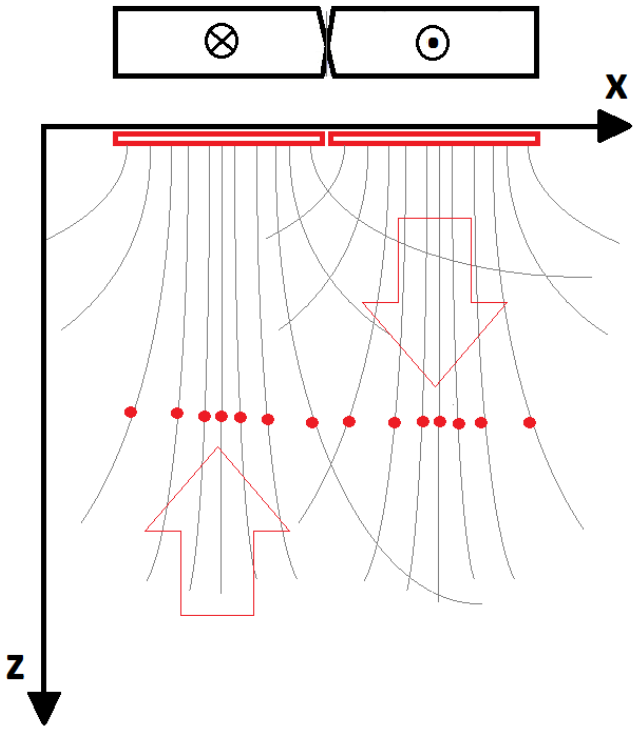

Figure 3.8: An object trajectory in the primary magnetic field shown as red dots, from left to right. Red arrows indicate the direction of the magnetic field vectors (shown in black). Along its trajectory, the object is interrogated from a variety of directions. Note that this picture is highly simplified and for illustration purposes only.

The *solution* of inverse optimization is defined as $\boldsymbol{\beta} = \{\widehat{\mathbf{M}}, \hat{\mathbf{P}}\}$, where $\hat{\mathbf{P}}$ is the estimated object trajectory. The inversion algorithm tries to find such a solution $\boldsymbol{\beta}$ that it minimizes the difference between the actual measured response $\hat{\boldsymbol{\rho}}$ and the theoretical response calculated with the above model ($\boldsymbol{\rho} = \boldsymbol{\rho}(\hat{\mathbf{p}}, \widehat{\mathbf{M}})$). The function to be optimised may be written as

$$F = ||\hat{\boldsymbol{\rho}} - \boldsymbol{\rho}||_2^2. \tag{3.2}$$

This optimization process is solved with the Levenberg-Marquardt algorithm (LMA), for which the details can be found in the literature [91, 92]. The algorithm starts by defining the initial guess $\boldsymbol{\beta_0} = \{\widehat{\boldsymbol{M}}_0, \hat{\mathbf{P}}_0\}$ for a solution. The initial guess of the MPT is defined to be the identity matrix, i.e., $\widehat{\boldsymbol{M}}_0 = \mathbf{I}_3$. $\hat{\mathbf{P}}_0$ is determined by finding the coil pair with the strongest response, and then assuming that the object travels along a straight line through the portal.

The residual value, r, is a measure for prediction error within inverse optimization, and it indicates the quality of $\boldsymbol{\beta}$. In the case of the portal, the residual is calculated by taking the L2-norm of the difference between the actual measurements $\hat{\boldsymbol{\rho}}$ and the forward response $\boldsymbol{\rho}$ as a function of the estimated MPT $\widehat{\mathbf{M}}$ and the path $\hat{\mathbf{P}}$, and dividing this value by the L2-norm of the measurements $\hat{\boldsymbol{\rho}}$, given by

$$r = \frac{||\boldsymbol{\rho} - \hat{\boldsymbol{\rho}}||}{||\hat{\boldsymbol{\rho}}||}, \tag{3.3}$$

where $\hat{\boldsymbol{\rho}}$ contains measurement values over time for all transmitter-receiver coil pairs.

The estimates described here are used in all the publications, as well as in Chapter 5, where the experimental results of this thesis are reported.

4 Classification methods

This chapter provides an overview of the available methods for classifying metallic targets, i.e., *magnetic singularity identification (MSI)* [69]. Perhaps the first method to classify metallic targets using EMI was proposed by Chesney et al. [46] in 1984. Over the past 30 years, the techniques have advanced with a variety of methods available now. Beran et al. [93] have proposed a model to coarsely divide methods of metallic object classification using EMI (see Figure 4.1). In their model, the two main approaches are *statistical classification*, i.e., *model-based approaches*, including *generative* and *discriminative methods*, and *library methods*. Generative methods (Section 4.3) aim to model the underlying data distribution that has produced the measured samples, whereas discriminative classifiers (Section 4.4) try to find a decision boundary in the so-called *feature space*. Library methods, (Section 4.5) also known as *example-based or dictionary matching approaches*, on the other hand, match the unknown sample with samples in a predefined library [93]. Before reviewing the

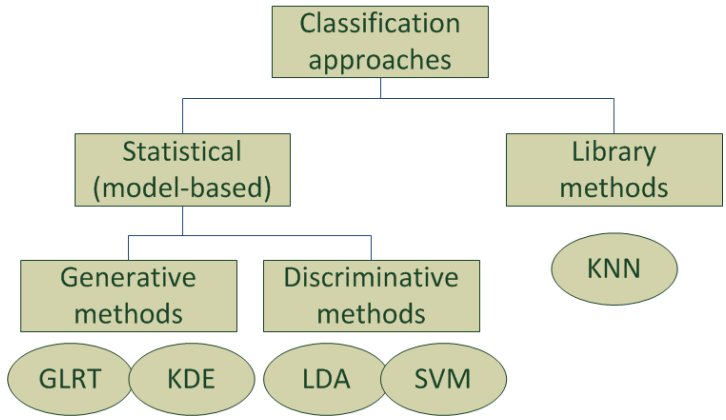

Figure 4.1: Classification methods, as described by Beran et al. [93].

different classification methods, this chapter introduces the basic concepts of classification (Section 4.1) and features (Section 4.2).

4.1 Basic concepts and terminology

Pattern classification is a process of assigning given unknown samples $\mathbf{x}$ to one of predefined categories, i.e., classes $\mathbf{\Omega} = \{\Omega_1\ \Omega_2\ \ldots\ \Omega_{N_\Omega}\}$, where N_Ω refers to the number of classes. The true class of the current sample in consideration, $\Omega(\mathbf{x})$, is also called the *state of nature* in the literature. In the context of classifying metallic objects, these terms are defined as follows. Samples $\mathbf{x}$ are N_{feat}-dimensional feature vectors that describe objects,

given by

$$\mathbf{x} = [feature_1 \ feature_2 \dots feature_{N_{feat}}] \tag{4.1}$$

A feature is typically either some measurement value, or a mapping from the measurement data space to a lower dimensional space, e.g., the mean value of a time-series of measurements. A good feature should characterize objects in terms of the classes of interest, i.e., produce similar values for objects within the same class, and dissimilar values for others [33]. These feature values are calculated by using measurements recorded by the WTMD portal. Moreover, because the parameter estimation described in Section 3.3 produces samples $\boldsymbol{\beta}$ that contain information on the characteristics of an unknown metallic object, we can write $\mathbf{x}_i = \boldsymbol{\beta_i}$, although $\mathbf{x}$ can contain further feature values extracted from $\boldsymbol{\beta}$. Classes $\boldsymbol{\Omega}$ are the categories that we wish to use for classification. The simplest and the most common scenario for WTMD portals is to distinguish between threatening and innocuous objects. Hence

$$\boldsymbol{\Omega_{simple}} = \{\Omega_1 \ = \ Innocuous, \ \Omega_2 \ = \ Threat\}. \tag{4.2}$$

However, for some scenarios, a more fine-grained categorization might be needed. For example, the threatening items can be further divided into sharp objects and firearms. On the other hand, innocuous objects can be classified, e.g., as belts, mobile phones, and wrist watches:

$$\boldsymbol{\Omega_{multiple}} = \{\Omega_1 \ = \ Belt, \ \Omega_2 \ = \ Coins, \ \Omega_3 \ = \ Knife \ , \dots , \ \Omega_{13} \ = \ Gun\}. \tag{4.3}$$

In case of metallic objects, however, defining formally what kind of objects should fall into these categories is challenging. For example, a variety of weapons have been designed to look like innocuous items, such as knives that resemble a lighter or a pen [94]. Obviously, in a security screening application, they should be classified as knives, but if the knife is also a lighter, how can the machine tell the difference? However, if the classes are heterogeneous, i.e., contain a variety of different kinds of objects, finding a model that is common for all the objects is challenging. For example, the class *knife* might include simple knives that consist of a single metallic blade and a wooden or plastic handle. On the other hand, some knives have a metallic handle, and Swiss Army knives contain a variety of different small tools whilst on the outside resembling a block of metal. The common feature of all knives is that they contain a blade. However, it is difficult to state exactly what a common knife is like as a metallic object. These difficulties of defining the classes pose a great challenge to classifier design.

Although a classifier can be based solely on heuristic rules, such as using arbitrary fixed thresholds for feature values, most systems generalize, i.e., *learn* the decision rules from a given set of examples, the *training data*. This learning process can be *supervised* or *unsupervised*. Supervised learning means that a set of training samples $\mathbf{X}_{TRAINING} = [\mathbf{x}_1 \ \mathbf{x}_2 \dots \ \mathbf{x}_{N_{TRAINING}}]$ ($N_{TRAINING}$ is the number of training samples) with known respective class labels $\boldsymbol{\Omega}_{TRAINING} = [\Omega(\mathbf{x}_1) \ \Omega(\mathbf{x}_2) \dots \ \Omega_{(}\mathbf{x}_{N_{TRAINING}})]$ is available. However, in unsupervised learning, this information is completely or partially unavailable. In this thesis, the emphasis is on supervised learning, although some unsupervised learning methods are covered in Section 5.7.

4.2 Features

As mentioned in 4.1, features are a means of making samples separable into classes to facilitate classification. A good feature should extract relevant information from the data

and/or the underlying phenomenon that the data describe. Features can, first, describe the data in a compact way, make raw data unnecessary, and enable simple comparison between the feature values, and, second, characterize the target by representing its intrinsic properties. Most parameters of the physical models described in Chapter 2 act as features because they describe the measured EMI signal in a compact manner and characterize the target. There are many examples of this in the literature. Tarokh et al. [71] have used the Laplace-plane pole representation of MPT eigenvalues to classify buried objects with a CW EMI device. In a pulsed EMI scenario, Fernandez et al. [95], used some decay parameters as features while applying the NSMS model, whereas Shubitidze et al. [96] have shown with real UXO test scenario data that use of such features can help accurately distinguish between UXO and clutter.

In the case of WTMD, raw time-domain measurement data consisting of the induced voltage of each coil pair is not very useful for classifying metallic objects, because it does not characterize the target adequately because it contains background noise and information related, e.g., to the speed of the walk-through and the gait of the candidate. Therefore, the MPT is a step towards a better characterization of the target, containing relevant information for classification, such as its intrinsic properties. In theory, the MPT is independent of target location but orientation-dependent, making it unsuitable for use as a feature. Therefore, eigenvalues $\boldsymbol{\lambda}$, as defined in Section 2.2, have been introduced, and as shown in Publication II, they constitute a rotation- (and location-) invariant [54] representation of the MPT, and hence a good feature. Moreover, according to Bell et al. [62], the eigenvalues contain all the information within the MPT that can be used for classification. [3]

In this thesis, eigenvalues $\boldsymbol{\lambda}$ as such refer to their *Cartesian* presentation, i.e., to complex two-dimensional values whose real part is on the X-axis and imaginary part on the Y-axis. However, for practical purposes, a *polar* presentation of the eigenvalues is defined. The *magnitude* of an eigenvalue λ_i is given by

$$\tau(\lambda_i) = \tau = ||\lambda_i|| = \sqrt{\lambda_i \cdot \overline{\lambda_i}}, \tag{4.4}$$

where $\overline{\lambda_i}$ is the complex conjugate of λ_i. In polar presentation, the magnitude is on the Y-axis. Similarly, the *angle* $\varphi(\lambda_i)$ of an eigenvalue is given by

$$\varphi(\lambda_i) = \varphi = \text{atan}(\Re(\lambda_i), \Im(\lambda_i)), \tag{4.5}$$

where *atan* is the four-quadrant arctangent function. In polar presentation, the angle is on the X-axis, and its range is usually $[-\pi \dots \pi]$. Correspondingly, the magnitude is on the Y-axis. These concepts are visualized in Figure 4.2.

It is known *a priori* that some materials are typical of certain types of objects, and similarly, e.g., knives are usually long and thin objects. Therefore, heuristic features for metallic target characterization might include descriptors of material, size, and shape. There are many examples in the literature that indicate the usefulness of MPT eigenvalues for this purpose. Norton et al. [61] state that the MPT represents the object as a uniform and ellipsoidal shape, and that its eigenvalues can be related to the lengths of

[3] Because the eigenvectors of $\overleftrightarrow{\mathbf{M}}$ are complex, they do not contain real orientation information for the object. It has been suggested by Prof. Lionheart that the real and imaginary parts of $\overleftrightarrow{\mathbf{M}}$ may be considered separately, hence yielding two sets of real eigenvectors. The relationship between these orientations may then be of value. However, SNR-related problems are likely to arise in WTMD portals.

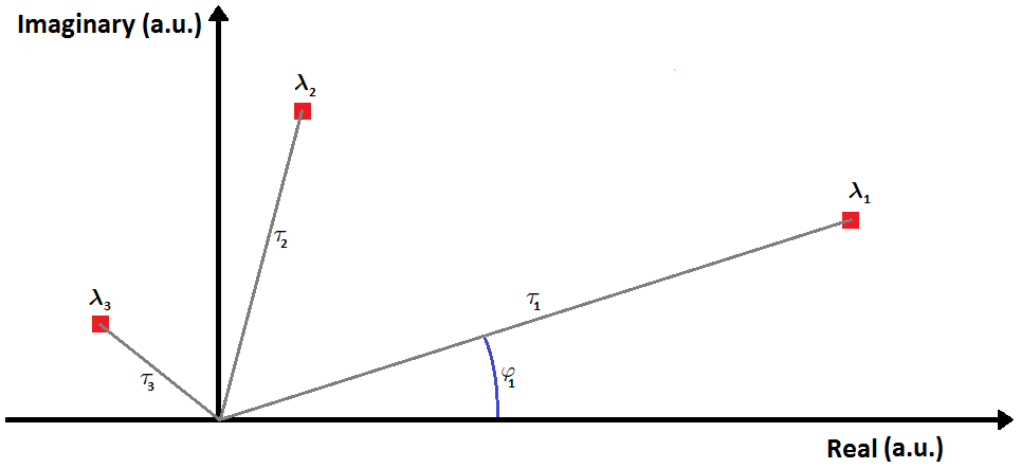

Figure 4.2: Eigenvalues and their angles and magnitudes, shown on a Cartesian plot.

the semi-major axes of the ellipsoid. [4] Furthermore, according to Bell et al. [40, 62], the eigenvalues of the MPT are related to the strength of the induced field along the principal axis of the target, and there is a strong correlation between the size of the target and the magnitudes of the eigenvalues. Moreover, they state that measurements of the longitudinal vs. transverse field ratio of the object show a strong correlation between the physical aspect ratio of the object and the corresponding measurements [40].

Many studies have used this aspect ratio as a feature for classification. In these studies, the elements of the time domain diagonalized MPT were often given by $\Lambda_X = m_{1,1}, \Lambda_Y = m_{2,2}, \Lambda_Z = m_{3,3}$; these values correspond to the eigenvalues $\boldsymbol{\lambda}$. In case of a cylindrical object, there are two distinct values: $\Lambda_{longitudinal} = m_{1,1}$ and $\Lambda_{transverse} = m_{2,2} = m_{3,3}$ (see, e.g., Khadr et al. [97] for details).

Khadr et al. [97] and Bell et al. [40] have used this representation for UXO/clutter discrimination using a pulsed EMI system. They propose a feature for modeling the length-to-diameter aspect ratio of the detected object, assumed to be a prolate spheroid, given as the ratio $|\Lambda_{longitudinal}/\Lambda_{transverse}|$ of two time-domain eigenvalues of the MPT.

However, this approach may not be reliable. Indeed, in the magnetostatic case, the above ratio is known to be nonlinear [55]. Furthermore, for the eddy current case, there are examples of nonlinearity in the literature. Bell et al. [40] consider a pulsed EMI system and argue that since the time window is of fixed length, the ratio of the transverse and longitudinal responses depends not only on the shape of the target but also on its size. More importantly, they have shown that the ratio is also frequency-dependent. In a more recent study, Bell et al. [62] state that in the time-domain, the transverse and longitudinal responses of the targets have different decay rates. This results in different ratios of the above eigenvalues at different times, and hence frequencies. A detailed analysis of the relationship between the eigenvalues and target size appears in another study by Bell et al. [41]. Barrow and Nelson [98] have used a similar method and ratios of the $\Lambda_{X,Y,Z}$-values to determine the shape of targets. However, they found that these values are related to object dimensions in a nonlinear fashion, and that there is a typical variance of 20-30%

[4] There exists mathematical proof of this in the magnetostatic case [55]. However, in the eddy current case, i.e., for conductive objects, this remains hypothetical.

around the mean of each value−-even for a steel sphere. They state that this variation in the values may arise from a measurement error due to sensor noise and inaccuracies in location estimation. To complicate things further, the coil geometry used affects the ratio; therefore, Grimm and Sprott [99] have studied different transmitter-receive coil geometries to be used with the above method.

However, a variety of advanced features exploiting the aspect ratio have been proposed. Pasion and Oldenburg [73] use the decay parameters in (2.8) to determine the shape of the object. They use ratios κ_1/κ_2 and ψ_1/ψ_2 to decide whether the geometry is plate-like or rod-like. Similarly, Norton et al. [54] have proposed *ordnance-likeness* as a feature to distinguish between UXO and clutter. First, they ordered the eigenvalue vector by their real parts in such a way that $\Re(\lambda_1) < \Re(\lambda_2) < \Re(\lambda_3)$. Then, a ratio was calculated by

$$OrdnanceLikenessRatio = \frac{\Re(\lambda_3) - \Re(\lambda_2)}{\Re(\lambda_2) - \Re(\lambda_1)}. \tag{4.6}$$

This ratio was then calculated at multiple excitation frequencies, and the feature for each object was the mean of $\log(OrdnanceLikenessRatio)$ across all frequencies. The imaginary parts of the eigenvalues were found less suitable for this purpose, as shown in the results [54]. Ambrus et al. [100], while using a pulsed EMI landmine detection system, took this idea further by constructing a 3-by-3 matrix of the ratios of all three eigenvalues, each of which was measured at three time gates of the detector, i.e., at three points in time, to capture the signal decay characteristics.

In addition to methods using the aspect ratio, some approaches in the literature classify metallic targets based on their volumetric size. However, these methods use more advanced classifiers. Zhang et al. [64] have used *support vector machines (SVM)* and *neural networks (NN)* for this (SVM and NN are described in Section 4.4). In addition, Fernandez et al. [101] have shown that spheroids of different sizes can be discriminated by their volume and radius by using an SVM. These studies suggest that features can be generated that enable use of size and shape information as features for classification.

Extracting material information from EMI data has also been reported. Huang and Won [102] have used CW EMI and modeled metallic targets as permeable and conductive spheres and used the model parameters to determine the conductivity and permeability of the targets. However, the results show that solving permeability and conductivity is feasible only in a noise-free scenario. Furthermore, using pulsed EMI, Pasion and Oldenburg [73] have used the parameter ψ in (2.8) to determine whether the target is magnetic or non-magnetic. Furthermore, Trang et al. [103] have studied the relationship of the phase angle and magnitude of a CW EMI response and the material of metallic targets. According to them, the permeability of the target can be seen at very low frequencies of the in-phase component of the response. Moreover, the phase angle of various metals, namely magnetic steel, non-magnetic steel, copper, brass, lead, and aluminium, was found to be independent of object orientation [103].

4.3 Statistical classification and generative methods

Bayesian decision theory lays the basis for optimal classification rules. The Bayes formula relates the posterior probability to the priors as

$$P(\Omega_i|\mathbf{x}) = \frac{P(\mathbf{x}|\Omega_i)P(\Omega_i)}{P(\mathbf{x})}, \tag{4.7}$$

where $P(\Omega_i|\mathbf{x})$ is the posterior probability for the state of nature being Ω_i given that the feature vector is $\mathbf{x}$, $P(\mathbf{x}|\Omega_i)$ is the prior conditional probability for the feature vector $\mathbf{x}$ given that the state of nature is Ω_i. $P(\mathbf{x})$ and $P(\Omega_i)$ are the independent probabilities for $\mathbf{x}$ and Ω_i, respectively. The prior (*a priori*) probabilities $P(\Omega_i)$ for the classes in $\mathbf{\Omega}$ are unknown, i.e., it is not possible to know how many, e.g., threats are encountered compared to innocuous items. Therefore, it is common to assume that each class is equally probable, but this also makes it impossible, in most cases, to use (4.7) directly for classification. If the prior probability density function (PDF) for each class is known, the likelihood ratio test (LRT) is the optimal classifier [33]. The LRT states the ratio between how likely the given data $\mathbf{x}$ is under the class Ω_i compared to the *null hypothesis*. A decision threshold for the ratio Υ is used to classify the samples. However, in most cases, the true PDFs $P(\mathbf{x}|\Omega_i)$ for each class Ω_i are unknown, though they may be estimated by using training data: the true PDF is replaced with a maximum likelihood estimate (MLE) of the PDF. As a visual example, Figure 4.3 shows a scenario of modeling the PDF for some class using its eigenvalues $\boldsymbol{\lambda}$. For each of the three eigenvalues, there is a cloud of data points within the training values. This cloud can be used to find an approximation of the PDF, or three PDFs, should each cloud be considered a PDF of its own.

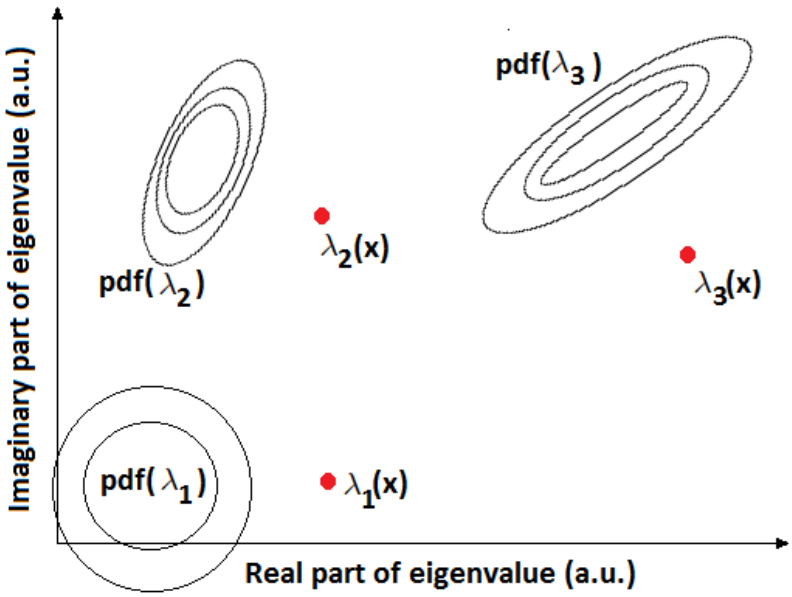

Figure 4.3: A PDF has been estimated for each eigenvalue of some category. The eigenvalues of an unknown sample $\mathbf{x}$ are shown in red. It is a statistical problem to estimate the probability of the red points having been created by the PDFs shown.

Collins et al. [72] were among the first to incorporate Bayesian decision theory in MSI, namely in landmine detection, using both CW EMI and pulsed EMI. For classification, they used the so-called *generalized likelihood ratio test (GLRT)*. The GLRT is a generalized version of the LRT, which can be used even if there are unknown parameters in the PDFs. The GRLT is given by

$$\frac{P_{MLE}(\mathbf{x}|\Omega_1)}{P_{MLE}(\mathbf{x}|\Omega_2)} \lessgtr \Upsilon, \tag{4.8}$$

where $P_{MLE}(\mathbf{x}|\Omega_i)$ is the maximum likelihood estimate of $P(\mathbf{x}|\Omega_i)$, and Υ is a decision threshold parameter (for details, see, e.g., Duda et al. [33]). The results of the Collins et al. study showed that the GLRT significantly outperforms the conventional threshold based methods. The GLRT has also been used for CW EMI data by Riggs et al. [69].

The performance of the GLRT using both signal space, i.e., using only the raw signal, and feature space classification has been compared in the literature. For example, Tantum and Collins [104] used decay parameters as features and compared that with using the whole time-domain signal for classification. Based on their simulated results, they argue that using the whole signal yields a higher level of accuracy than using the features. However, Aliamiri et al. [50] have made a similar comparison and come to an opposite conclusion. They state that this is because of model mismatch, i.e., the presence of non-Gaussian deterministic noise within the signal, especially in case of large targets. Yet, they show that some reasonable violations may be tolerated against the dipole model assumptions if their effect on parameter estimation is well understood. Furthermore, they state that overcoming the model mismatch problem requires developing a rich library that takes parameter variation, such as their position and orientation dependency, into account as completely as possible. They used kernel density estimation (KDE) with a Gaussian kernel to estimate prior PDFs for the classes. The MPT eigenvalues at 4 distinct frequencies were used as features. However, they observed that the eigenvalue PDFs were markedly non-Gaussian by nature. Consequently, a whitening transform was applied to normalize the shape of the data distribution prior to applying KDE. Furthermore, though the MPT eigenvalues should be orientation- and position- invariant in principle, this is not the case in reality; therefore, measurement data from several orientations and positions are needed to model the PDFs [105].

In summary, while feature-space classifiers are suboptimal in theory compared, e.g., to a signal space GLRT, they are more robust against the problems of the dipole model. Aliamiri et al. [50] argue that as long as the feature value clouds are distinct and well-defined, the feature-based methods perform well regardless of the above model mismatch.

4.4 Non-parametric discriminative methods

Parametric classification methods are problematic because they depend on the estimation of prior PDFs for each class. Moreover, parametric PDF estimation always assumes a unimodal PDF, making modeling of multimodal PDFs impossible. On the other hand, discriminative, non-parametric feature-based methods skip prior PDF estimation and instead, using the training data, aim to directly estimate the posterior probabilities $P(\Omega_i|\mathbf{x})$ for a given feature vector, i.e., to solve the probability of each class Ω_i, given the unknown sample $\mathbf{x}$.

Typically, a discriminative classifier finds a decision rule that divides the feature space into regions, each of which corresponds to a certain class Ω_i. A linear discriminant analysis (LDA) -based binary classifier is one of the simplest examples of such functionality. Based on training data, it finds a linear function that divides unknown samples into two categories. The linear function is defined by finding a weight factor $\mathbf{w}_i$ for each training sample $\mathbf{x}_i$. In case of two features, the problem can be seen as finding a line in two-dimensional space that divides the training samples into two categories in an optimal way. The linear discriminant is calculated by

$$\mathbf{w} \cdot \mathbf{x} \lessgtr \Upsilon, \tag{4.9}$$

where w is a weight vector, and Υ is the decision threshold. This simple binary LDA approach may be easily applied to a multiclass case by defining a binary decision tree classifier. A binary decision tree is an intuitive and transparent way to define the classification logic of a system. Such a tree consists of a series of decision nodes, which divide the feature space hierarchically into subspaces until a conclusion is reached, i.e., a leaf of the tree. Each decision node may be defined as a binary LDA rule, though any rule that divides the feature space can be used. Moreover, the nodes need not even deal with numeric features. This makes decision trees a logical choice for problems in which similarity between feature values is difficult to define. The complexity of a node can vary from a simple linear discriminant to a multilayer neural network.

Pasion and Oldenburg [73] propose a classification scheme that resembles a tree classifier. The inputs of the classifier are, as discussed in Section 4.2, parameters ψ_1, ψ_2, κ_1, and κ_2. First, the algorithm calculates $\overline{\psi} = (\psi_1 + _2)/2$. If $\overline{\psi} > 0.8$, the object is likely to be magnetic; otherwise, it is considered non-magnetic. Then in case of magnetic targets, if $\kappa_1/\kappa_2 > 1$ and $\psi_1/\psi_2 < 1$, the object is magnetic and rod-like. However, if $\kappa_1/\kappa_2 < 1$ and $\psi_1/\psi_2 > 1$, the object is magnetic and plate-like. In the case of non-magnetic targets, if $\kappa_1/\kappa_2 > 1$, the object is non-magnetic and plate-like. Otherwise, the object is non-magnetic and rod-like [73]. This heuristics-based method has been shown applicable in practice to identify of UXO [106]. Why this does not make a proper binary tree is that in theory undefined outcomes are possible because the leaves do not cover the whole feature space.

A *support vector machine* (SVM) is a linear binary classifier, and hence related to the LDA classifier. Therefore, it is suited, e.g., for distinguishing between threatening and innocuous items. An SVM requires no *a priori* knowledge about the underlying process that has generated the data [101]. Let $\mathbf{x}_i$ be feature vectors for training and $\mathbf{g}_i \in \{-1, 1\}$ the corresponding ground truth labels for the two classes in consideration, i.e., for Ω_0, $g = -1$ and for Ω_1, $g = 1$. An SVM searches for a hyperplane $g_i(\mathbf{x_i} \cdot \mathbf{w} + s_f) - 1 \geq 0$, where $\mathbf{w}$ is a vector of weight factors and s_f is a scaling factor. The optimal hyperplane should maximize the margin $2/|\mathbf{w}|$. The idea is that most weights $\mathbf{w}$ are found irrelevant during the training phase in such a way that they converge to zero terms. The remaining samples that get nonzero weights are called *support vectors*, and they essentially define the hyperplane. Moreover, to prevent overfitting, an SVM imposes a penalty for misclassifications. This is called the capacity of the machine (for details on SVMs, see, e.g., Duda et al. [33] and Fernandez et al. [95]).

This linear SVM can be transformed into a non-linear version by using a *kernel function* $K(\mathbf{a}, \mathbf{b}) = \Phi(\mathbf{a}) \cdot \Phi(\mathbf{b})$, which maps the input vectors $\mathbf{a}$ and $\mathbf{b}$ into a higher dimensional space [33]. The *radial basis function (RBF)*, also known as the *Gaussian kernel*, is a commonly used kernel function. It is given by $K(\mathbf{a}, \mathbf{b}) = e^{-|\mathbf{a}-\mathbf{b}|^2/2\sigma^2}$, where σ is a parameter controlling kernel width. This function essentially measures the similarity between $\mathbf{a}$ and $\mathbf{b}$; i.e., when they are close in Euclidean space, the output is close to one, and if they are dissimilar, the output is close to zero. Therefore, the classifier will converge to the nearest neighbour classifier with small values of σ [33, 101, 107] (see Section 4.5).

To discriminate between multiple classes, the problem must be split into several binary classification problems by using multiple *one-against-one* (OAO) or *one-against-all* (OAA) SVM classifiers, or a *directed acyclic graph SVM* [108]. In the OAO method, the output class is usually determined by choosing the class that has most positive outcomes out of all comparison pairs. In the OAA method, on the other hand, usually the class with

the best performance is assigned as output. Furthermore, the multiclass problem can be converted to a binary classification tree problem, in which each node is solved with an SVM, as demonstrated by Fei and Liu [109].

In the literature, the SVM is widely used for BOD. For example, Fernandez et al. [101] used an SVM with a RBF kernel to classify UXO. They measured their data using CW EMI at five distinct frequencies and used MPT eigenvalues as classification features. The classifier discriminated objects based on their size, namely radius, length, and volume [101]. They have also successfully used a multiclass SVM with a voting-based OAO approach to classify UXO, this time with time-domain decay parameters as features [95]. Moreover, Aliamiri et al. [50] have used a similar multiclass SVM OAO approach to classify buried objects.

4.5 Dictionary matching and K-nearest neighbour classification

Dictionary matching, also known as *fingerprint matching* [110], is a non-parametric classification method, in which training data is used to form a library (*dictionary*) of feature vectors (*fingerprints*). Like discriminative methods, dictionary matching estimates the *a posteriori* probabilities $P(\Omega_i|\mathbf{x})$ from the training samples; i.e., class labels from training data are used directly to classify unknown samples. The classification outcome is constructed by matching the unknown sample $\mathbf{x}$ with the most similar feature vector in the library. The similarity of samples in terms of given features is based on some distance metric $D(\mathbf{a}, \mathbf{b})$.

Perhaps the most commonly used distance metric is the *Euclidean distance*, also known as the *L2-norm*. In case of two vectors $\mathbf{a}$ and $\mathbf{b}$ of N samples, it is given by

$$D(\mathbf{a}, \mathbf{b}) = \sqrt{\sum_{i=1}^{N} (\mathbf{a}_i - \mathbf{b}_i)^2}. \tag{4.10}$$

Norton and Won [61] have used the L2-norm has been used as a goodness-of-fit measure for multi-frequency MPT eigenvalues as follows:

$$E_m = \sum_{l=1}^{N_f} \sum_{i=1}^{3} w_l |\hat{\lambda}_i(\omega_l) - g\lambda_i(\Omega_n, \omega_l)|^2, \tag{4.11}$$

where ω_l is the lth discrete frequency, w_l is a (positive) weighting factor for each frequency, g is a scaling factor, $\lambda_i(\Omega_n, \omega_l)$is the ith eigenvalue for class Ω_n and frequency ω_l, and $\hat{\lambda}_i(\omega_l)$ is the ith eigenvalue of the unknown sample, measured at frequency ω_l. Moreover, the authors state that using separate scaling factors (g_R and g_Q) for real and imaginary parts of the eigenvalues may yield better classification results. However, scaling is only necessary if the signal amplitude must be normalized, as in UXO detection. The WTMD data is already scaled, as explained in Chapter 3. Other common distance metrics include the Manhattan distance (i.e., L1 norm), Minkowski, and Chebyshev distances [111].

These simple metrics may not be suitable for certain types of features, e.g., in a case when the classifier must determine the similarity between two eigenvalue spectra, such as sets of DSRF-parameters, because the spectra may contain a different number of frequency bins [79]. *Earth Mover's Distance (EMD)* is defined as the work needed to convert one DSRF spectrum into another; hence the name. In addition, Huang and Won [112] have

proposed a distance metric for two CW EMI spectra containing the same number of frequency bins, given by

$$D(\mathbf{a},\mathbf{b}) = \frac{\sum_{i=1}^{N_f}(|\Re(\mathbf{a}_i) - \Re(\mathbf{b}_i)| + |\Im(\mathbf{a}_i) - \Im(\mathbf{b}_i)|)}{\sum_{i=1}^{M}(|\Re(\mathbf{b}_i)| + |\Im(\mathbf{b}_i)|)}, \tag{4.12}$$

where $D(\mathbf{a},\mathbf{b})$ is the misfit in percent, i is the index of frequency bin, and N_f is the number of frequency bins used.

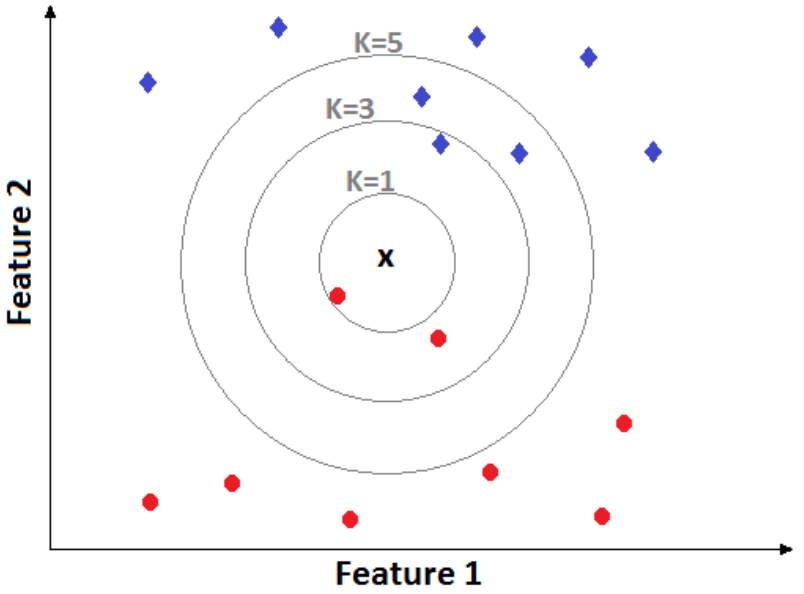

Figure 4.4: The K-nearest neighbour algorithm principle. The neighbourhoods $K = 1$, $K = 3$, and $K = 5$ are marked with circles. For $K = 5$, the classification outcome would be the blue category, otherwise the red one.

Nearest neighbour classifiers are typical dictionary matching methods. Already in 1988 by McFee and Das [113] used such methods to classify magnetometer-based MPT data based on early findings in the field, such as the study by Moskowitz and Della Torre [114]. Nearest neighbour classification works as follows. Using the definitions in Section 4.1, let $\mathbf{X}_{TRAINING}$ be a vector of N_T training samples, and $\mathbf{\Omega}_{TRAINING}$ their respective class labels. Let $\mathbf{x}' \in \mathbf{X}_{TRAINING}$ be the *nearest neighbour* of an unknown sample $\mathbf{x}$ and Ω' its class label. The term *nearest neighbour* refers to the sample $\mathbf{x}'$, which is at the shortest distance from $\mathbf{x}$, i.e., $\mathbf{x}' = arg\ min\ D(\mathbf{x},\mathbf{x}_i)$, $\mathbf{x}_i \in \mathbf{X}_{TRAINING}$, where $D(\mathbf{a},\mathbf{b})$ is the distance function used to measure the similarity of samples $\mathbf{a}$ and $\mathbf{b}$. The nearest neighbour classifier relies on a single sample to determine the class. This leads to suboptimal performance in terms of theoretical error rate, i.e., the Bayes rate [33]. Intuitively, the reliability of the decision can be improved by using more samples for classification. In K-nearest neighbour (KNN) -classification, K nearest samples in terms of distance D are chosen, and the class label that appears most often within these samples is assigned to sample $\mathbf{x}$. To avoid draws, K is usually an odd number. Figure 4.4 shows the principle of KNN-classification. Increasing the value of the parameter K lowers the

theoretical upper bound for the classification error rate; i.e., the error gets closer to the Bayes rate. On the other hand, the K nearest neighbours must be close enough to $\mathbf{x}$ in terms of distance D not to lose classification reliability. As a compromise, small values such as 3 and 5 are often used. The idea of the KNN method is to model the underlying PDFs using only the local neighbourhood close to the sample $\mathbf{x}$ [115].

A variety of modified versions of the KNN have been presented in the literature. Non-uniform weighting of the nearest neighbour samples has been proposed to give more importance to the samples that are similar to $\mathbf{x}$ in terms of the distance measure [115, 116]. Such weighting enables use of a larger region K while keeping the focus on the nearest samples. Furthermore, a fuzzy version of the KNN has been proposed by Remus et al. [115], to enable the nearest neighbours to have a fuzzy membership in multiple classes.

The literature contains a variety of studies on the use of the KNN for scenarios such as distinguishing between landmines and clutter. For example, in one such study, Tantum et al. [79, 117] used DSRF spectra as features and the EMD for distance calculation. In addition, Fails et al. [111] used the four parameter model (2.9) by Miller et al. [48] as features. Their distance calculation employed a search region of K samples, and within the region, compared the mean distance from $\mathbf{x}$ to landmine targets with the mean distance to clutter targets.

5 Classification of metallic targets using the WTMD portal

This chapter presents the contributions reported in the included five publications, and shows that the objectives laid out in Section 1.2 have been met. Furthermore, the contributions and results are discussed.

The structure of this chapter is as follows. Section 5.1 presents the concept of the so-called body effect and explains how it shows in measurements made with the portal. Section 5.2 presents the data collection procedure used in this thesis and provides an overview of the library contents. Section 5.3 provides information about the kind of noise and bias components in the library samples and elaborates the reasons for their occurrence. Furthermore, information is provided about how the effect of these components can be diminished. Section 5.4 discusses the factors that contribute to the reliability of the samples from the classification point of view. In addition, a novel method to detect unreliable samples is presented. Section 5.6 shows that metallic objects can be accurately classified using the WTMD portal and the KNN. Section 5.5 demonstrates that MPT eigenvalue angles $\boldsymbol{\varphi}$ contain information about the material of the object, and that a correlation exists between MPT eigenvalue magnitudes $\boldsymbol{\tau}$ and the dimensions of objects. Finally, Section 5.7 generalizes on the results.

5.1 Body effect

The *body effect* is a phenomenon that describes the interference caused by the human body in the received portal signal. It can be either inductive or capacitive in nature, depending on its source. From an electromagnetic point of view, the body is somewhat conductive and eddy currents thus flow around the body, creating a secondary magnetic field, which in turn affects the primary field. This inductive body effect adds up to the changes caused by the actual target object. Furthermore, because the body is a large object, its EM response is significant enough to be measurable with the portal. However, according to experts in the field, the scale of these inductive effects depends on coil design and the sensitivity of the portal; the phenomenon can be seen mainly in devices designed to detect very small items.

In the portal described in Chapter 3, the body effect happens mainly due to, as shown in Publication III, capacitive coupling between the human body and the portal coils. The key to the phenomenon is the electric field generated by the transmit coils. The effect is then based on the relatively high permittivity of the human body, which consequently causes the body to act as a capacitor and generates direct electric interference in the

receive coil signal. Therefore, the capacitive body effect does not, in principle, alter the magnetic fields within the portal detection space.

The results in Publication III show that each of the five candidates had a unique, repeatable body effect signal, which did not correlate with the approximated body volume. Based on observations of the raw measurement signal, a conclusion was made that for large test objects, in this case NIJ gun phantoms, the body effect was relatively small whereas for small objects, such as an NIJ aluminium knife phantom, the body effect signal was clearly summed with that of the target, as shown in Figure 7 from Publication III.

Publication I showed that the body effect may significantly affect the classification results. Consequently, it had to be taken into account in designing the data library and the experiments in this thesis.

Furthermore, the capacitive body effect might be reduced or even removed by preventing the electric field caused by the transmit coils from entering the portal detection space. In Publication I, it was suggested that this may be done using insulative screening (such as tape or paint on the portal panels) between the body and the portal coils. However, the inductive body effect cannot be removed by physical means. On the other hand, a calibration routine could be developed to remove both body effect components because evidence suggests that they form a measurable and repeatable error component to the signal.

5.2 Data library

Portal manufacturers are usually the ones to do research on detecting and classifying metallic objects with WTMD portals. And understandably, they are reluctant to release their data to public domain for fear of disclosing technical details and corporate secrets and providing competitors with potentially useful information. Therefore, no database is publicly available of parametrized EMI responses, such as MPT eigenvalues of typical metallic objects. Hence, the data library for the studies in this thesis was constructed by the author using the measurement system described in Chapter 3 at the University of Manchester, UK.

The data was collected via natural walk-through scans performed by several subjects (*candidates*), though most (>95%) of them in the library were performed by the author. As discussed in Section 5.1 and shown in Publication III, the body effect influences the measured signal and the obtained MPT values. Thus, using mainly the same candidate for data collection ensures that the measurements are comparable, and that also any variance in other factors, such as gait, is eliminated.

Furthermore, since walk-through speed and object trajectory may affect the measurement values and thereby the estimated MPTs, it is crucial to be able to produce consistent, repeatable measurements. No exact method was used to control the walk-through speed; thus, as a compromise, the aim was to walk through the portal always at the same, natural, steady pace.

The object trajectory, *path*, varies mainly as a function of object placement (*location*) on the body of the candidate as well as on the placement of the steps that the candidate takes. Naturally, different candidates also have a different height and gait, which might affect the resulting trajectories. In Publication V, it was demonstrated that object location, and hence the path, has an effect on the MPT eigenvalues, and therefore a method for controlling the trajectories is necessary. Keeping the object in a repeatable location for

the duration of a walk-through always produces about the same object trajectory if the candidate enters the portal in the same way and walks along the same steps. This was ensured by marking a foot placement grid on the portal floor (Figure 5.1).

Figure 5.1: Step guidance markings on the portal floor.

The repeatability of object location was ensured as follows. An *apron*, i.e., a plastic and cardboard vest with location markings, was constructed with the markings of the apron showing 12 locations. The locations were selected to correspond to the test locations for WTMD portals defined by the NIJ [20, p. 7] (see Figure 2 of Publication V; note that only 8 of the 12 locations are shown). This measurement setup made data collection repeatable and enabled production of comparable MPT values (an example of a walk-through scan and the data collection setup is shown in Figure 1 in Publication V).

In total, the data library contains 142 objects and 4394 samples. Figure 5.2 shows a comprehensive list of the object types and the objects included in the library. Figure 5.3 features examples of the objects in the library.

Figure 5.4(a-d) shows the eigenvalues of the selected objects and Figure 5.5(a-d) the corresponding objects. Each object registers eigenvalue clusters in both non-magnetic ($\varphi \in [0 \dots 1]$) and magnetic ($\varphi \in [2 \dots pi]$) zones. Experience shows that objects made of a single type of metal yield eigenvalue clusters in only one of these zones (details, e.g., in Publication IV). Thus, the phenomenon in Figure 5.4 may be due to the fact that the objects consist of several distinct metals. However, their exact metallic composition is unknown.

Figure 5.6 shows the eigenvalues of an object consisting of eight phantom bullet cases. This example is here to show that sometimes inverse optimization finds two or more

- Misc. objects (27)
  - Ferrite spheres (1)
  - Ferrite rods (1)
  - Brass strips (2)
  - Iron strips (6)
  - Aluminium strips (6)
  - Iron cylinders (3)
  - Aluminium cylinders (3)
  - AISI/304 stainless steel cylinders (3)
  - AM magnetic steel cylinders (3)
  - AN non-magnetic steel cylinders (3)
- Artificial joints (1)
- Belts (7)
- Bags of coins, from various countries (13)
- Containers, pocket-size metallic boxes (6)
- Mobile electronics (9)
  - Mobile phones (5)
  - MP3 players (4)
- Jewellery (2)
- Sets of keys (9)
- Lighters (2)
- Wrist watches (5)
- Shoe shanks (7)
- Scissors (2)
- Spoons (1)
- Nail clippers (1)
- Gun phantoms, gun phantom parts, phantom ammunition (19)
  - Sets of phantom bullet cases (3)
  - Gun phantom parts (2)
  - Guns phantoms (14)
- Knives (27)
  - Opinel knives (7)
  - NIJ knife models (2)
  - Swiss army knives (4)
  - Pen knives (2)
  - Miscellaneous knives (12)

Figure 5.2: Objects comprising the library. The numbers in brackets indicate the total number of objects within the particular category.

distinct solutions for the same object (for more information, see Section 5.4). Here the two cluster triplets may have been caused by the fact that the measurements came from two distinct object locations. However, experience has shown that this phenomenon is somewhat rare in the library.

The data library contains a wide variety of objects, and the number of objects is relatively large. However, because there exists a practically infinite number of different metallic objects, the library is, in the end, quite small and sparse. Furthermore, for each object, the number of samples is limited. Performing walk-through scans was time-consuming and data could not be gathered on all objects at various portal locations and orientations. However, for the purposes of this thesis, the library contains enough samples, especially since the measurements were carefully selected to study the phenomena of interest.

5.3 Bias and noise in signals

Publication V proves that an element of bias and different noise components are present in the measured system response $\hat{\boldsymbol{\rho}}$, and that the response can be given by

$$\hat{\boldsymbol{\rho}}(\mathbf{p}, \boldsymbol{\Theta}) = \boldsymbol{\rho} + \boldsymbol{\mu}(\mathbf{p}, \boldsymbol{\Theta}) + \mathbf{N}_{\text{body}} + \mathbf{N} \ , \tag{5.1}$$

where $\boldsymbol{\Theta}$ is the orientation of the object, $\boldsymbol{\rho}$ the theoretical response solely for the target object, $\boldsymbol{\mu}(\mathbf{p}, \boldsymbol{\Theta})$ a position and orientation dependent bias term, $\mathbf{N}_{\text{body}}$ the body effect, and $\mathbf{N}$ a general noise term. Generally, in the above equation, the body effect signal cannot be considered noise, but rather a systematic error term. However, the body effect depends on the physiological properties of the person (e.g., the volume of body fluids, which varies

Figure 5.3: *Opinel*-brand knives and shoe shanks. The knives from top to bottom are: Opinel Effile (size 12), Opinel INOX (size 8), and Opinel Lame Acier (size 8). Note that in their dimensions the blades resemble the shoe shanks.

due to conditions such as dehydration) and hence may vary daily. Furthermore, from the point of view of the underlying dipole model and from an overall perspective described in (5.1), the body effect term $\mathbf{N}_{\text{body}}$ represents an individual noise-like error source.

Moreover, Publication V states that estimated eigenvalues can be thought to consist of several parts that are determined by the above bias and noise terms in the signal:

$$\boldsymbol{\lambda}(\widehat{\mathbf{M}}) = \boldsymbol{\lambda}(\overleftrightarrow{\mathbf{M}}) + \boldsymbol{\mu}_{\lambda} + \mathbf{N}_{\lambda}, \tag{5.2}$$

where each term denotes the contribution of the corresponding terms in (5.1). $\mathbf{N}_{\lambda}$ contains the combined noise effect caused by $\mathbf{N}_{\text{body}}$ and $\mathbf{N}$. Figures 3(a-d) in Publication V demonstrate the positional and orientation biases and noise in the data.

Based on the background knowledge in Chapters 2 and 3, the bias term consists of all the imperfections that cause the dipole model to be built on a skewed view of the object. These imperfections exist mainly due to the fact that the primary field vectors are in reality not perfectly parallel, as shown in Figure 5.7, and that especially near the transmit coils they are far from the requirements of the dipole model. Second, the strength of the field vectors varies due to, e.g., the decay of the magnetic field further away from the transmit coils. Third, the view on the object is not optimal because some view directions always register more measurements than others. Finally, though the measurement system used in this thesis is a single frequency excitation system, each transmit coil functions at a distinct frequency. The frequency bands are some 500Hz-1kHz apart. This may seem like a small difference, but as shown by the eigenvalue frequency response curves in Figures 2.1 and 2.2, significant changes can happen to MPT eigenvalues within a couple of

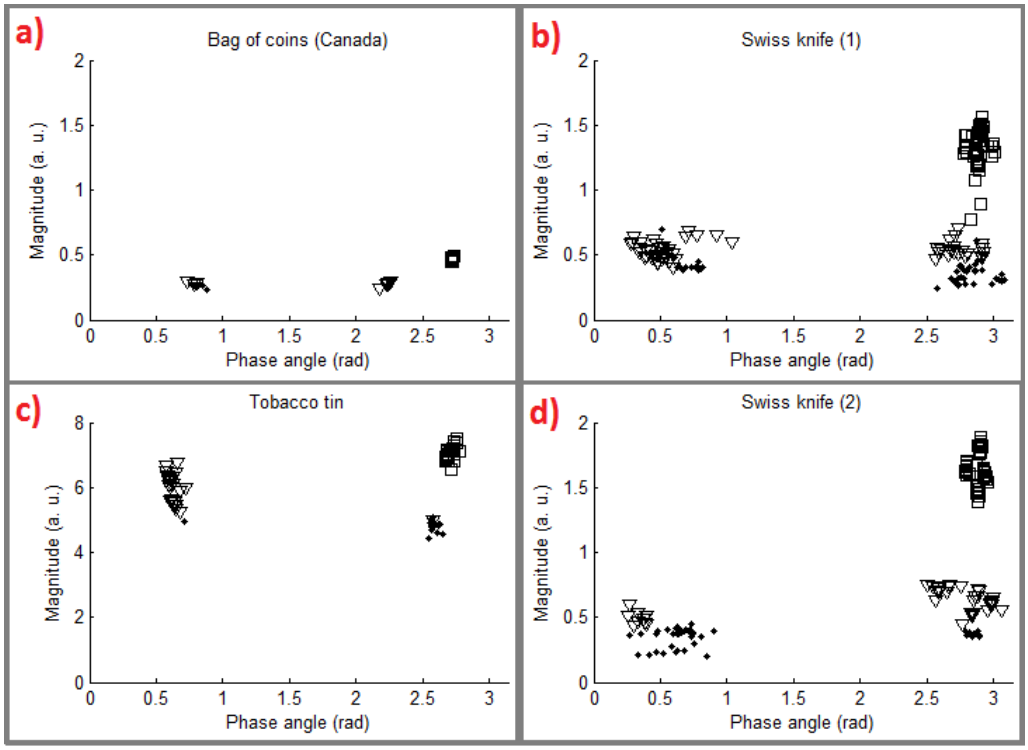

Figure 5.4: Eigenvalues of selected objects in the library. Note that the Y-axis scale of (c) is distinct. The different symbols denote the eigenvalues λ_1, λ_2, and λ_3 ordered by magnitude. The corresponding objects are shown in Figure 5.5.

frequency bands. The MPT estimation process does not take such changes into account, a limitation that may cause some of the current bias. Moreover, the positional bias may depend also on the material of the object because, according to Shubitidze et al. [82], the response of heterogeneous targets can change close to the coils.

The literature supports the existence of the bias term. For example, Aliamiri et al. [50] have noticed that the spread of data values modeled with the dipole model is non-Gaussian by nature, a finding that corresponds to the bias term introduced in Publication V. Moreover, they claim that the variability in the values is deterministic, agreeing with the findings in Publication V. According to Aliamiri et al., apart from background noise, the parameter variation is caused by model mismatch, meaning that the dipole model is not a good approximation of the underlying physics. They conclude that the bias could be reduced by using a more accurate physical model [50].

Eliminating the main sources of the bias, namely getting the magnetic fields to correspond more closely to the assumptions made in the definition of the model, or using operating frequencies closer to one another, seems challenging and beyind the scope of this thesis. Nevertheless, reducing the bias would be beneficial. Because it may never be possible to produce unbiased and high SNR measurements across the whole portal space, these problems must be addressed and taken into account at the later stages of the system, namely feature extraction, classification, and decision making. For example, a feasible option might be to use the estimated path information to compensate for the positional

Figure 5.5: Examples of objects in the library. a) Canadian coins b) a Swiss knife (1) c) A tobacco tin d) a Swiss knife (2). The corresponding eigenvalues are shown in Figure 5.4.

bias. Because similar trajectories yield similar MPT estimates for the same object, the trajectory information could be used to increase or decrease the reliability of the sample. Alternatively, one might use only the fingerprints from roughly the same location for the dictionary matching process. This could be done by estimating a YZ-plane centre position for the samples using their trajectories. However, this does not apply to the orientation bias because there is no method available to estimate the orientation of objects.

5.4 Detection of unreliable samples

As explained in Section 3.3, the inverse optimization -based parameter estimation algorithm seeks a solution $\boldsymbol{\beta}$ that best fits the measured signal $\hat{\boldsymbol{\rho}}$, given the physical model defined in Section 3.2. From the classification point of view, one would want the algorithm to yield such a solution $\boldsymbol{\beta}$ that the MPT estimate $\widehat{\mathbf{M}}$ would always be as close to the theoretical MPT $\overleftrightarrow{\mathbf{M}}$ as possible. The same applies to the path estimate $\hat{\mathbf{P}}$ and $\mathbf{P}$. However, several factors cause problems that can finally lead to poor MPT estimates. A poor MPT estimate here means that the estimated parameter values differ significantly (i.e., to an amount clearly not resulting from normal noise variance) from the true theoretical MPT. Such poor estimates are called *Unreliably Inverted Tensors (UITs)* in Publication V. Since theoretical MPT values are unknown, another way to define a UIT is to approach the problem through repeatability. From the classification point of view, theoretical MPT values are not necessary if the classification algorithms use only training data that is produced by the same or a similar measurement system with the same properties.

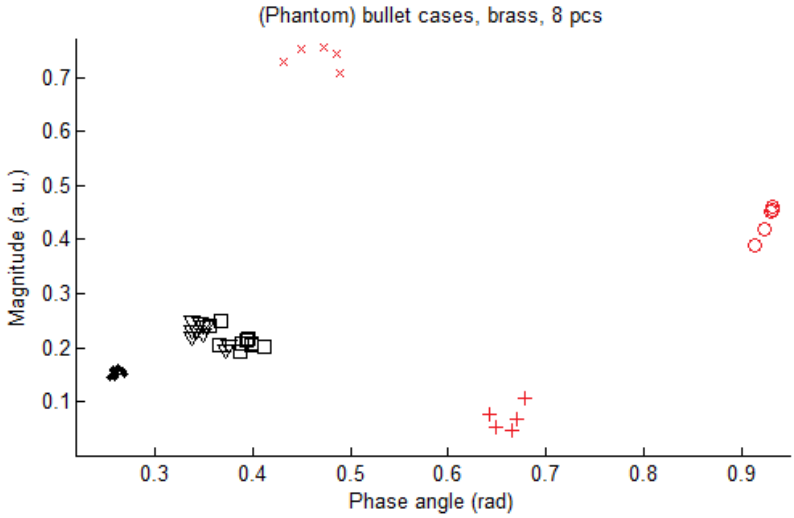

Figure 5.6: Phantom bullet cases, 8 pieces. Note that the eigenvalues form two sets of three clusters because of two separate solutions found by inverse optimization. Importantly, the distinct solutions come from two separate portal locations. The points marked in red come from location 2-2, whereas the black points come from near the coils, location 1-3 (for location details, see Publication V)

Figure 5.8 shows a UIT scenario by using estimated MPT eigenvalues for a belt. Inverse estimation has here produced two distinct solutions.

Several factors may produce UITs. First, the assumptions limiting the applicability of the dipole model (see Section 2.2) may be invalid. Indeed, real objects are rarely homogeneous and never infinitely small to be presented as a point in space, nor are they an infinite distance away from the coils to ensure parallel field vectors across the sample. Consequently, the model may not be valid for the given object and measurement, and the solution that yields the lowest residual may, in fact, be a poor estimate for the true MPT. Inverse estimation can thus produce values that have a low fitting error, but that are outliers compared to the other data points assigned to the objects of the same object class [118].

Second, the problem with many inverse optimization algorithms, including the one used in the portal, is that they can get stuck at local minima instead of finding the global minimum, i.e., the optimal solution, as demonstrated in Figure 5.9. Therefore, the solution depends on the initial guess taken [118].

The literature offers approaches to tackle the problem of sample unreliability. Remus and Collins [118] have proposed a method using the *Fisher information metrics* as a means to evaluate the quality of samples produced by inverse optimization. In addition, Walker et al. [119] propose a measure called the *figure of merit* for quantifying data quality, based on factors such as the perceived SNR of the signal and size of the detected object. Such data quality measures may help quantify the reliability of classification outcomes.

On the other hand, Grzegorczyk et al. [120] have used a *Kalman filter* to reduce the effect of Gaussian noise on the inverse estimation of the MPT and the position of metallic targets. The problem with this approach is that the noise may in reality not be Gaussian,

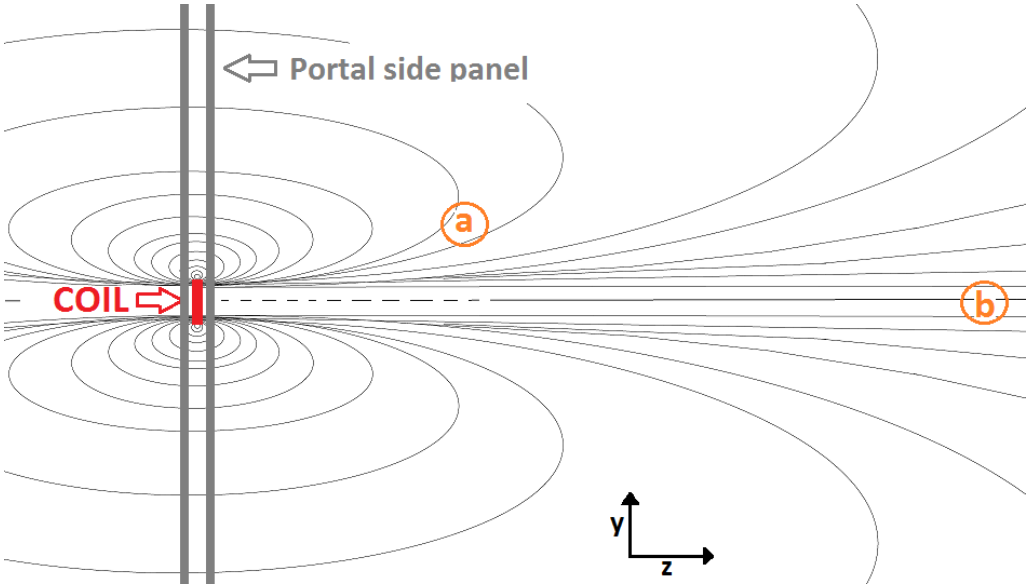

Figure 5.7: The limitations of the dipole model. The figure shows the shape of the magnetic field created by a coil in 2D. Close to the coil, the field vectors are curved, causing a skewed view of the object (a). Further away from the coil, the field vectors are parallel, enabling use of the dipole model for object (b).

as shown by Aliamiri et al. [50]. Furthermore, Beran et al. [121] have proposed two methods for taking data uncertainty into account when considering estimated EMI model parameters. The first method models data uncertainty, i.e., noise, with Gaussian PDFs and thereby trains an SVM, which is consequently optimized for noisy data. The second one tackles the problem of multimodal data distributions, such as the one shown in Figure 5.8, by creating a set of points for each measurement by inverse optimization by using a large number of distinct initial guesses. The consequent multimodal distribution is modeled using a Gaussian mixture model [121].

Publication V proposes a method for detecting UITs. This method can be considered to perform so-called *outlier detection* [122], and it uses residual-value- and heuristics-based features calculated from the path information. Logistic regression (LR) is used to choose the best set of features along with corresponding weights and thresholds. The results show that the novel method can, indeed, detect samples that would otherwise be unreliable for classification, enabling a consequent significant increase in classification accuracy with the rest of the samples. Furthermore, path-based features performed better than residual-based features, but a combination of a moderate residual threshold, such as $r_T = 0.6$, in combination with path features performed best. The publication proposes that samples detected as UITs be fed back to inverse optimization with a new initial guess. Experience has shown that these UITs derive largely from a poor initial guess, which is quite hard to recover from.

Moreover, this encourages improvement of inverse optimization by using several initial guesses instead of one, as proposed by Beran et al. [121]. The resultant possible increase in computational time is not a concern because of the sinking costs of processor power.

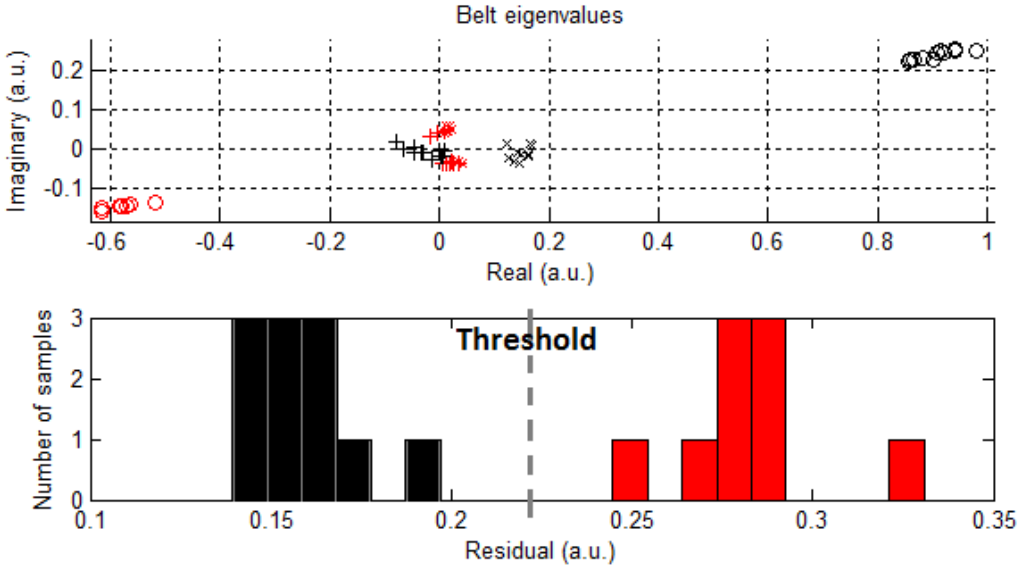

Figure 5.8: An example of two distinct solutions (shown in red and black) found by the inverse optimization. The upper graph shows the eigenvalues for a belt, and the lower one the corresponding residual histogram.

5.5 Estimating material and geometric properties of objects

Publication IV showed that it is possible to distinguish between a variety of metals using a single frequency component of the MPT. Furthermore, it was showed that only one eigenvalue, λ_3, i.e., the one with the largest magnitude, is needed. Consequently, the angle φ_3 was the feature to classify materials. The materials used for the study were aluminium, copper, stainless steel, ferrous steel, and brass. Accuracies of over 94% were reported for using only φ_3 as a feature, whereas using the magnitude τ_3 as additional information helped to raise the accuracy beyond 98%. For these classifications, a simple LDA classifier was used.

Furthermore, Publication IV examined the correlation between MPT eigenvalue magnitudes, $\boldsymbol{\tau}$, and object dimensions. For this, a library consisting of a variety of metallic strips and cylinders was used. The results showed that the object surface area and the length of the MPT magnitude vector, $|\boldsymbol{\tau}|$, correlate. Moreover, for similar objects of similar materials, this correlation is somewhat linear.

Section 4.2 discussed many approaches found in the literature to estimate the aspect ratio of an object by using either the ratio of eigenvalues as such or that of eigenvalue magnitudes. Such an approach is logical because a variety of object classes can often be described by their shape. However, in the context of the portal, this is not straightforward. As shown in Publication IV, it is not accurate to estimate dimensions by using magnitude values. Thus, using these values to estimate the aspect ratio of an object may not be reliable. Moreover, as explained in Section 4.2, concerns have been voiced about using such an approach. Because the ratio of eigenvalues (or magnitudes) is not constant, exploiting it for a classification feature should be done in a constrained scenario, preferably when the types of possible target objects are known *a priori*.

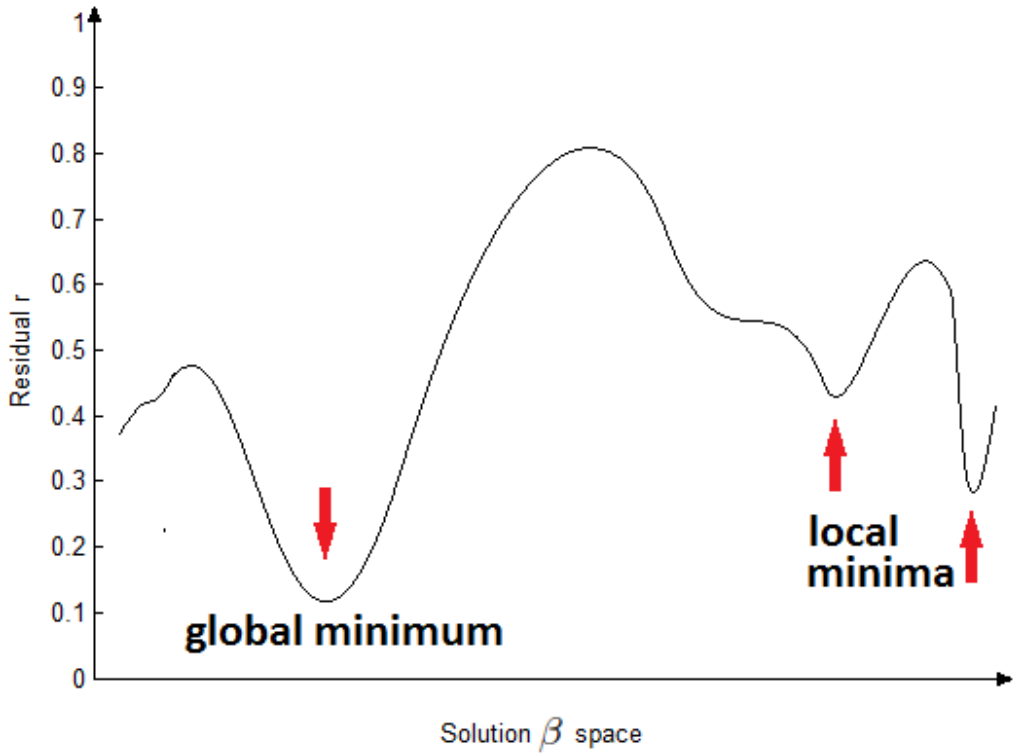

Figure 5.9: The principle of inverse optimization. The algorithm can get stuck at local minima because the residual value grows as the solution moves away from the minimum.

Publication IV demonstrated that the phase angle and magnitude of MTP eigenvalues correspond to the material and geometric properties of the object. Therefore, it is logical to use these features to determine the similarity of two given samples. However, feature scaling can be a problem because a difference in phase angles cannot directly be compared with a difference in magnitudes. Moreover, as shown in Figure 5.10, phase angle values of low magnitude MPT eigenvalues are noisy and contain no reliable information. The above feature weighting may be a possible solution, but these features could also be used separately. In many scenarios, it may be enough to determine for each MPT eigenvalue λ_i whether it refers to a magnetic or a non-magnetic entity, and whether the magnitude of λ_i is small, i.e., noisy, or large enough to be considered for material determination.

5.6 KNN Classification of metallic targets using WTMD EMI data

Publications I, II, and V, exploited a KNN-algorithm for classification. In Publications I and II, each eigenvalue vector $\boldsymbol{\lambda}$ was sorted in order of an increasing magnitude τ of each eigenvalue λ_i; i.e., that λ_1 is the smallest and λ_3 the largest by magnitude. The distance D between the sample to be classified, $\hat{\mathbf{x}}$, and each sample $\mathbf{x_i}$ in the *dictionary*, the collection of known reference samples, was calculated using a distance measure, given

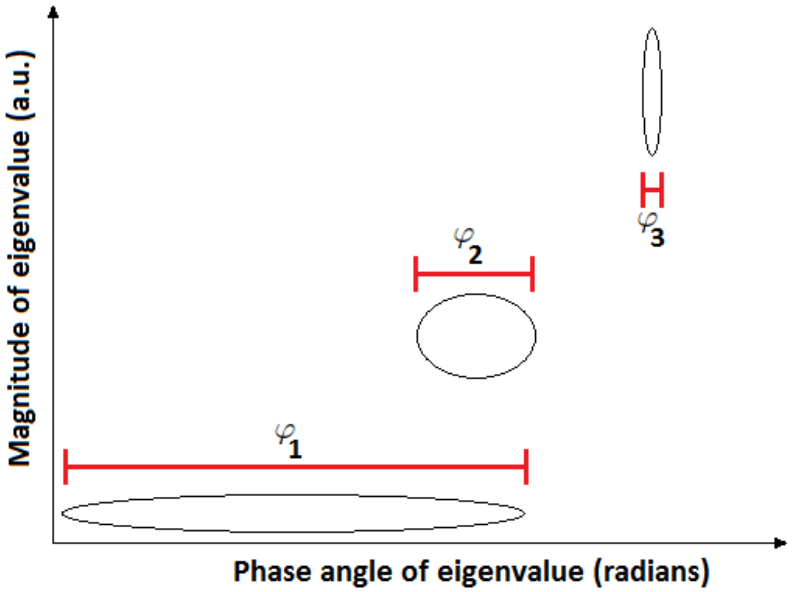

Figure 5.10: The effect of noise and low MPT eigenvalue magnitudes on the corresponding phase angle values. Low magnitude eigenvalues cannot be relied on when their angle is used for classification. Note that the figure is for illustration purposes only and does not represent real data.

by

$$D(\boldsymbol{\lambda}_a, \boldsymbol{\lambda}_b) = \sqrt{(\lambda_{a,1} - \lambda_{b,1})^2 + (\lambda_{a,2} - \lambda_{b,2})^2 + (\lambda_{a,3} - \lambda_{b,3})^2}, \tag{5.3}$$

where $\boldsymbol{\lambda}_i$ are eigenvalue vectors, and $\lambda_{i,j}$ are the corresponding sorted eigenvalues. This distance was calculated only once for the sorted eigenvalue vectors. However, in Publication V, the distance was calculated six times, i.e., once per each permutation of the eigenvalue orders within the vectors. Regardless of the distance calculation method, the class of sample $\mathbf{x_i}$ with the smallest resulting distance was selected as the classification outcome because sorting the eigenvalues λ_i by magnitude τ does not always result in matching the corresponding clusters with one another.

The effect of the parameter value K was studied in Publications I and II. Because the training data contained only a few samples of each class, using values $K = 3$ or higher resulted in worse performance than using $K = 1$, i.e., the nearest neighbour -classifier. Hence, it has been shown that $K = 1$ is a suitable value when the size of the training data is small. Therefore, Publication V used only $K = 1$ instead of repeating the study of the previous papers.

In Publication I, for a library of 1316 samples, an accuracy in excess of 98% and a recall of over 99% were reported to distinguish between threatening and innocuous objects. In classifying the samples into 10 categories, accuracies were over 94%. Filtering out samples with a residual value of more than 0.5 improved results, highlighting the fact that in principle, samples with a high residual value are more unreliable to classify than those with low residual values.

Publication I also addresses the impact of the body effect on classification. The results

with two candidates of significantly different body size suggest that the body effect can be seen also with high SNR objects, and that it can significantly affect classification accuracy. The accuracies gained with the body effect test data were significantly lower than those from other tests.

In Publication II, for a library of 835 samples, the threat/innocuous -classification yielded accuracies of over 95%, with a recall of over 95%. Classification accuracy into 13 categories was reported to be over 85%. These results are slightly worse than those in Publication I, but this is because of a more challenging library of objects, which was collected especially to test the limits of the method. Again, filtering out high residual samples using thresholds of 0.35 and 0.5 improved accuracies at the cost of not being able to classify all the samples.

Moreover, the results of Publication II indicate that the classification method was indeed capable of handling fine differences in object size and materials when the data were recorded by using a single location. This capability was demonstrated in Publication II by distinguishing between 1) different kinds of knives, 2) different shoe shanks, 3) metallic containers of different sizes, and 4) knives and shoe shanks. Furthermore, the method was shown to be able to estimate the number of phantom bullet cases in a phantom gun. Publication II concluded that 1) a broader object library is needed, that 2) the library should contain objects in several locations and orientations, and that 3) separability of different materials, shapes and sizes of objects should be studied. 1) and 2) were demonstrated in Section 5.2, and 3) was discussed in Section 5.5.

Finally, Publication V showed that a classification method that uses all possible eigenvalue permutations performs slightly better than one that uses sorted eigenvalue vectors. Furthermore, the proposed UIT detection method, when used prior to classification, can significantly reduce the number of misclassifications.

In conclusion, classifying metallic objects with KNN yields demonstrably excellent accuracy results. Therefore, it is certainly possible to classify metallic objects with the method presented in this thesis.

However, KNN may have the downside of relying only on the library of training samples. In a scenario where a variety of unknown objects of known classes are likely to be encountered, an SVM with a Gaussian kernel may be a suitable option because it functions like KNN but has perhaps a slightly better capacity for generalization.

Furthermore, the Euclidean distance used in Publications I, II, and V may have the weakness of being sensitive to the scaling of features. The one-to-one scaling between the calibrated real and imaginary components of MPT eigenvalues is arbitrary and does not necessarily yield optimal distance scores to distinguish between different object classes. Another type of scaling or calibration of these components may affect classification performance. Instead of using the above arbitrary scaling, it is possible to find scalar weights for each feature. Hence, for MPT eigenvalues, the distance would be of the form $D_{weighted}(\mathbf{a}, \mathbf{b}) = \sum_{i=1}^{N} w_i \cdot D(\mathbf{a}(i), \mathbf{b}(i))$, where $\mathbf{a}$ and $\mathbf{b}$ are feature vectors, $\mathbf{a}(i)$ and $\mathbf{b}(i)$ are the ith feature values of $\mathbf{a}$ and $\mathbf{b}$, and w_i are the weights that can be estimated by using training data.

Three studies in the literature that reported metallic object classification using a WTMD portal. Al-Qubaa et al. [123] have proposed an electromagnetic imaging -based WTMD portal, which classifies 12 distinct objects, namely six guns, a knife, a wristwatch, a key, a screwdriver, and a pair of scissors, as threatening and innocuous objects. This classification method is based on creating features using, e.g., the discrete wavelet transform and the

fast Fourier transform and classifying samples using an SVM or a NN classifier. However, the classification accuracies reported [24, 124] are low compared to those in this thesis. Furthermore, the amount of data in the reported tests allows no analysis of the reliability of the method. In addition, no real walk-through scans were used in the study.

Elgwel et al. [25], on the other hand, have proposed a method to classify conductive objects in a pulsed EMI WTMD portal scenario. The research was based on finite element modeling (FEM) -simulations only. The method exploited a so-called decay parameter as a feature to characterize objects. Six objects were studied, namely a wristwatch, a key, a mobile phone, a knife, a handgun, and a hand grenade. The simulations indicate that the method could detect multiple objects simultaneously and distinguish between them. However, adding noise to the simulation quickly lowered performance [25]. Because this study was based on simulations only, the feasibility of its method for a real-world scenario cannot be analyzed.

The study by Kauppila et al. [26], conducted at Tampere University of Technology, can be considered pioneering for the publications in this thesis, which focused on nearest neighbour -based classification of metallic targets using EMI data measured with a WTMD portal. However, there are some key differences between the study by Kauppila et al. and the ones presented in this thesis. First, Kauppila et al. used no real walk-through scan data because of the body effect problems described in Section 3.1. Instead, to simulate the performance of their system, they used real MPT estimates of a wide range of objects. To validate their results, they produced real measurement data using a WTMD system prototype and a special robotic arm. Second, as mentioned in Section 3.1, the two systems differ in their coil geometries though the inverse estimation algorithms in this thesis would apply to both systems. Third, Kauppila et al. used the L1-norm as a distance measure instead of the Euclidean distance used here. Nevertheless, Kauppila et al. have shown with simulations based on real MPT estimates that metallic targets can be classified with a single frequency component (over a wide range of frequencies) of the MPT. Furthermore, they used robotic arm data successfully to validate the simulated results. In sum, their results are comparable to those presented here, as shown in Publication V. Therefore, this thesis confirms that the classification performance predicted by Kauppila et al. can be achieved by using real walk-through scan data, and that the body effect is no longer a prohibitive factor for the technology. Based on these observations, it can be argued that the methods and results of this thesis represent the state-of-the-art in the field.

5.7 Generalization and future work

This thesis has focused on a single object scenario in which the number of target objects per walk-through scan is one. However, in practice, a WTMD system must deal with multiple objects simultaneously. In BOD, several studies have been reported on simultaneous detection and characterization of multiple objects (Hu et al. [125], Economou et al. [126], Remus and Collins [127], and Grzegorczyk et al. [128]), confirming its feasibility. Moreover, at least two studies have reported multi-object detection and characterization using a WTMD portal. First, Elgwel et al. [25] considered a simulated multi-object scenario. Second, and most importantly, Marsh et al. [129] tested the same measurement system used in this thesis for a multi-object scenario by using up to three objects simultaneously; the dipole model enables the representation of multiple objects using multiple MPTs if the objects are sufficiently far apart. Therefore, the methods presented in this thesis can be expected to be generalizable to a multi-object scenario in the near future. Essentially,

if MPTs can be reliably estimated for all targets, the classification methods presented here are undoubtedly capable of dealing with the task. However, there is work to be done to optimize the measurement system so that reliable inverse optimization could be realized for locating and characterizing an arbitrary number of targets.

In this thesis, supervised learning techniques were used as the primary means to train classifiers. However, the necessary predefined training data may not be representative or even available [86]. Furthermore, producing labeled training data is laborious and expensive. It is also practically impossible in general to have a set of training data that would, e.g., contain all the objects that might be encountered in a real-life security screening scenario.

On the other hand, unsupervised learning can reduce human involvement in training the methods and allow for online learning of unknown target types. The literature contains some studies on using unlabeled training data for classifying metallic objects. For example, Benavides et al. [130] have used unsupervised learning, namely *self-organizing maps*, to discriminate UXO. Furthermore, Liu et al. [131] have proposed a *semi-supervised learning* method for detecting and classifying UXO, which uses both labeled and unlabeled data, and have demonstrated the usefulness of their method in a real-world scenario. In addition, Bijamov et al. [86] have proposed a semi-supervised UXO classification method based on an iterative clustering algorithm, which first groups unlabeled EMI signatures of targets into clusters and, step by step, requests labels for them. As labels are revealed, the system learns more and more different types of UXO and clutter signatures. The number of clusters to be formed is predefined.

This clustering approach is somewhat analogous to my earlier work [132] in the context of semantic video retrieval. In a WTMD scenario, the approach may be used for a semi-supervised online learning scheme as follows. First, the method should contain a fairly large amount of training data from most classes to be encountered. The system then calculates the distance of an unknown sample $\mathbf{x}$ to the known samples. If the distance is small enough, i.e., the classification decision can be trusted, the object is classified as usual. However, if $\mathbf{x}$ resembles no known sample, the portal triggers the alarm. A manual inspection is carried out to identify metallic target(s). This identification information is then input into the system by a human operator. If the target cannot be identified, the system may still store its EMI signature and path estimate for use in clustering. Based on the labeled and unlabeled samples, the system should be able to improve its classification method on the fly.

This thesis has presented classification algorithms to distinguish between metallic objects. Figure 5.11 shows an overview of the structure of the proposed system. However, these algorithms cannot directly be applied to a real security screening scenario without any additional intelligence for final decision making. The reliability of the classification decision must be analyzed, and based on the cost of misclassifications, a decision must be made, e.g., on whether to raise the alarm or not. The implementation of this logic is application-specific. However, the method by Pasion et al. [133] serves as a good starting point. The authors have proposed two thresholds for decision making. The first is a data quality threshold, which determines the minimum SNR for measurements to ensure sample reliability. The second is a threshold that determines the maximum reliable distance for library methods; i.e., how far the closest matching library sample can be from the unknown sample to rely on it for classification. Pasion et al. propose that optimal threshold values could be determined by using either training data or simulations.

The methods presented in this thesis may enable use of a single portal hardware solution

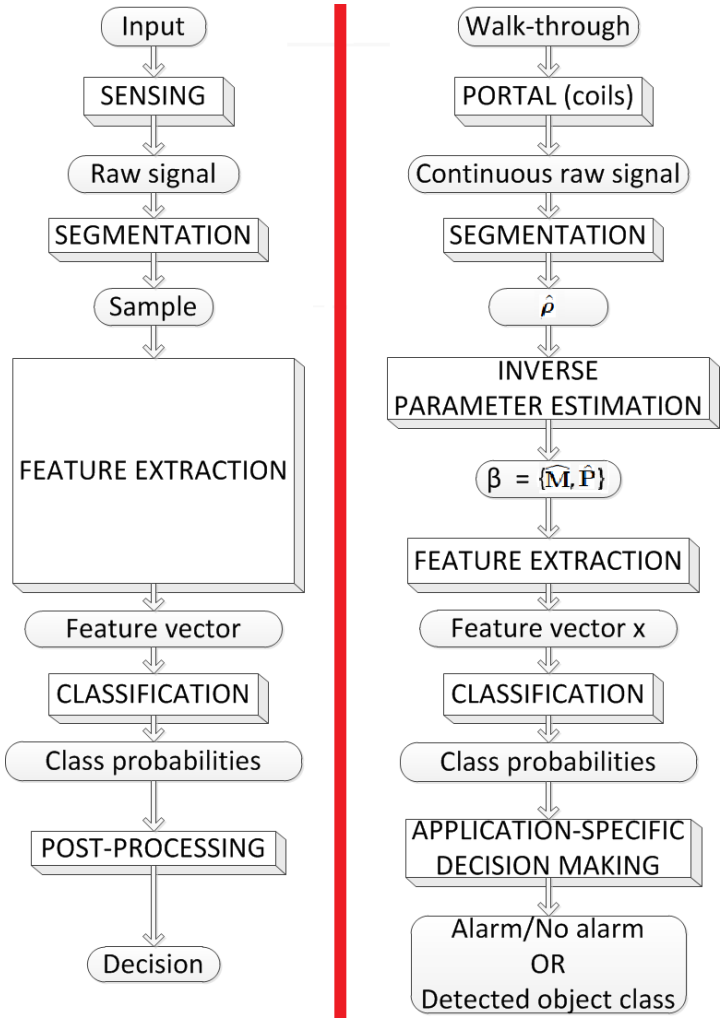

Figure 5.11: A classification system overview as presented in [33] (left) and the corresponding structure used in this thesis.

while tailoring a variety of classification schemes for different scenarios. For example, various items are forbidden at major sporting events, shopping malls, and airports. In these cases, only the EMI signature library, and possibly the classification algorithm, must be changed. Ideally, one could add to and remove forbidden items from the library on the fly as operational requirements change. As long as MPT parameters can be solved for the detected target object, a KNN classification scheme can be set up trivially by gathering training samples of, e.g., the threat objects that the system is required to detect.

6 Conclusion

Chapter 5 has shown that the WTMD portal described in Chapter 3 can help accurately classify metallic objects into 10 to 13 arbitrary classes and distinguish threatening objects from innocuous ones.

Furthermore, it has been shown that although the measurements made with the portal are subject to many problems, such as body effect and signal bias, they can be overcome and a high classification accuracy can be maintained.

A self-diagnostics method for detecting unreliable samples has also been presented. The results show that the method can significantly increase classification accuracy and the reliability of decision making.

Further generalization of the results has been discussed in Section 5.7, and, arguably, the technology can be commercialized. The next steps in this direction are, first, to enable simultaneous classification of multiple objects, and, second, to diminish or compensate for the effects of bias and noise by designing hardware that can produce better SNR and minimize the effect of model mismatch. However, based on the information in the literature and the observations made in this thesis, compensating for the problematic issues by introducing algorithmic tools on the classifier side may be a good way forward. Other topics for future work include enabling the use of multiple excitation frequencies to gain more information on the frequency response of the object.

The implications of the results of this thesis are three-fold. Firstly, for the EMI-based metal detection and characterization research community, it has been shown that the MPT, having been successfully used in the field of UXO/landmines for years, can be applied to WTMD security screening. In addition, the positive results encourage using the methods presented here also for other research, such as classification of UXO/landmines. Second, for the field of WTMD security screening, it has been shown that a paradigm shift, i.e., eliminating the need to remove all metallic items before screening, is possible. Moreover, the novel technology offers more information by indicating the probable cause for the alarm to support the conventional screening procedure. Finally, the technology enables design of new products for time-critical WTMD screening scenarios such as major sporting events and train stations where airport-style methods may be too slow and inconvenient, and opens up new business possibilities for companies like Rapiscan.

Bibliography

[1] R. J. Brown. HistoryBuff.com: Alexander Graham Bell and the Garfield assassination. Last visited 2015-04-25. [Online]. Available: http://www.historybuff.com/library/refgarfield.html

[2] C. V. Nelson, "Metal detection and classification technologies," *John Hopkins APL Technical Digest*, vol. 25, no. 1, pp. 62–67, 2004. [Online]. Available: http://techdigest.jhuapl.edu/td/td2501/nelson.pdf

[3] B. Roston, "Development of locators of small metallic bodies buried in the ground," *Electrical Engineers - Part II: Power Engineering, Journal of the Institution of*, vol. 95, no. 48, pp. 653–664, Dec. 1948.

[4] The Federal Aviation Administration (FAA): A historical perspective, 1903-2008, Chapter 4. Last visited 2015-07-11. [Online]. Available: https://www.faa.gov/about/history/historical_perspective/media/historical_perspective_ch4.pdf

[5] Transportation Security Administration (TSA), evolution timeline. Last visited 2015-07-11. [Online]. Available: http://www.tsa.gov/video/evolution/TSA_evolution_timeline.pdf

[6] The National Commission on Terrorist Attacks Upon the United States: The 9/11 commission report. Aug. 21, 2004. Last visited 2015-04-21. [Online]. Available: http://www.9-11commission.gov/report/

[7] "After the attacks: Airport security; F.A.A. announces stricter rules; knives no longer allowed," *New York Times*, Sep. 12, 2001, last visited 2015-04-21. [Online]. Available: http://www.nytimes.com/2001/09/13/us/after-attacks-airport-security-faa-announces-stricter-rules-knives-no-longer.html

[8] K. Gkritza, D. Niemeier, and F. Mannering, "Airport security screening and changing passenger satisfaction: An exploratory assessment," *Journal of Air Transport Management*, vol. 12, no. 5, pp. 213 – 219, 2006. [Online]. Available: http://www.sciencedirect.com/science/article/pii/S0969699706000354

[9] "New Jersey rail station tests metal detectors," *Los Angeles Times*, Feb. 2, 2006, last visited 2015-04-18. [Online]. Available: http://articles.latimes.com/2006/feb/08/nation/na-bombscreen8

[10] "Scanning Britons for knife crime," *BBC News*, Dec. 9, 2004, last visited 2015-04-21. [Online]. Available: http://news.bbc.co.uk/2/hi/uk_news/4078019.stm

[11] "Rapiscan Systems metal detector receives National Center for Spectator Sports and Security lab recognition," *Reuters*, Nov. 18, 2014, last visited 2015-02-25. [Online]. Available: http://www.reuters.com/article/2014/11/18/ca-rapiscan-systems-idUSnBw185942a+100+BSW20141118

[12] "Major league ballparks beef up security with metal detectors," *USA Today*, Apr. 6, 2015, last visited 2015-06-03. [Online]. Available: http://www.usatoday.com/story/sports/mlb/2015/04/06/major-league-ballparks-beef-up-security-with-metal-detectors/25372453/

[13] "Metal detectors coming to Air Canada Centre," *Toronto Sun*, Apr. 13, 2015, last visited 2015-06-03. [Online]. Available: http://www.torontosun.com/2015/04/13/metal-detectors-coming-to-air-canada-centre

[14] "Analysis: Nairobi attack may trigger tighter security at malls worldwide," *Reuters*, Sep. 22, 2013, last visited 2015-04-21. [Online]. Available: http://www.reuters.com/article/2013/09/22/us-kenya-attack-mallsecurity-analysis-idUSBRE98L0LP20130922

[15] "Canal Walk gets metal detectors," *IOL News South Africa*, Oct. 21, 2014, last visited 2015-04-21. [Online]. Available: http://www.iol.co.za/news/crime-courts/canal-walk-gets-metal-detectors-1.1768214#.VTYZd2MyHKA

[16] "Over 1,200 weapons taken from NYC students last schoolyear," *New York Post*, Oct. 19, 2014, last visited 2015-04-21. [Online]. Available: http://nypost.com/2014/10/19/over-1200-weapons-confiscated-from-city-schoolkids-nypd/

[17] "Weapon detectors in city schools," *BBC News*, Feb. 14, 2008, last visited 2015-04-21. [Online]. Available: http://news.bbc.co.uk/1/hi/england/hampshire/7245298.stm

[18] J. S. Dines, H. Elkousy, T. B. Edwards, G. M. Gartsman, and D. M. Dines, "Effect of total shoulder replacements on airport security screening in the post-9/11 era," *Journal of Shoulder and Elbow Surgery*, vol. 16, no. 4, pp. 434 – 437, 2007. [Online]. Available: http://www.sciencedirect.com/science/article/pii/S1058274607002066

[19] Rapiscan Metor 6S product specification. Last visited 2015-07-11. [Online]. Available: http://www.rapiscansystems.com/en/products/ps/metor_6s

[20] The National Institute of Justice (NIJ) -standard 0601.02: Walk-through metal detectors for use in concealed weapon and contraband detection. Last visited 2015-07-29. [Online]. Available: https://www.ncjrs.gov/pdffiles1/nij/193510.pdf

[21] The National Institute of Justice (NIJ) website. Last visited 2015-07-29. [Online]. Available: http://www.nij.gov/

[22] H. M. Chen, S. Lee, R. M. Rao, M. A. Slamani, and P. K. Varshney, "Imaging for concealed weapon detection," *IEEE Signal Processing Magazine*, vol. 22, no. 2, pp. 52–61, Mar. 2005.

[23] A. Agurto, Y. Li, G. Y. Tian, N. Bowring, and S. Lockwood, "A review of concealed weapon detection and research in perspective," in *Networking, Sensing and Control, 2007 IEEE International Conference on*, Apr. 2007, pp. 443–448.

[24] A. R. Al-Qubaa, A. Al-Shiha, and G. Y. Tian, "Threat target classification using ANN and SVM based on a new sensor array system," *Progress In Electromagnetics Research B*, vol. 61, pp. 69–85, 2014. [Online]. Available: http://www.jpier.org/pierb/pier.php?paper=14050704

[25] A. Elgwel, S. W. Harmer, N. J. Bowring, and S. Yin, "Resolution of multiple concealed threat objects using electromagnetic pulse induction," *Progress In Electromagnetics Research M*, vol. 26, pp. 55–68, 2012.

[26] J. Kauppila, T. Ala-Kleemola, J. Vihonen, J. Jylhä, M. Ruotsalainen, A. Järvi, and A. Visa, "Classification of items in a walk-through metal detector using time series of eigenvalues of the polarizability tensor," in *Society of Photo-Optical Instrumentation Engineers (SPIE) Conference Series*, vol. 7303, May 2009.

[27] L. G. Roybal, P. M. Rice, and J. M. Manhardt, "New approach for detecting and classifying concealed weapons," in *Proc. SPIE*, vol. 2935, 1997, pp. 96–107. [Online]. Available: http://dx.doi.org/10.1117/12.266790

[28] D. K. Kotter, L. G. Roybal, and R. E. Polk, "Detection and classification of concealed weapons using a magnetometer-based portal," in *Proc. SPIE*, vol. 4708, 2002, pp. 145–155. [Online]. Available: http://dx.doi.org/10.1117/12.479303

[29] C. Baum, "Identification of hidden mines," in *Electromagnetics in Advanced Applications, 2007. ICEAA 2007. International Conference on*, Sep. 2007, pp. 692–695.

[30] C. Baum, "Identification of buried unexploded ordnance," in *Radar, 2008 International Conference on*, Sep. 2008, pp. 17–18.

[31] K. O'Neill and J. Fernández, "Electromagnetic methods for UXO discrimination," in *Unexploded Ordnance Detection and Mitigation*, ser. NATO Science for Peace and Security Series B: Physics and Biophysics, J. Byrnes, Ed. Springer Netherlands, 2009, pp. 197–221. [Online]. Available: http://dx.doi.org/10.1007/978-1-4020-9253-4_10

[32] C. E. Baum, "Discrimination of buried targets via the singularity expansion," *Inverse Problems*, vol. 13, no. 3, p. 557, 1997. [Online]. Available: http://stacks.iop.org/0266-5611/13/i=3/a=003

[33] R. O. Duda, P. E. Hart, and D. G. Stork, *Pattern Classification (2nd Edition)*. Wiley-Interscience, 2000.

[34] AK Steel: AISI 304/304L stainless steel product data sheet. Last visited 2015-04-18. [Online]. Available: http://www.aksteel.com/pdf/markets_products/stainless/austenitic/304_304l_data_sheet.pdf

[35] TIBTECH: Properties table of stainless steel, metals and other conductive materials. http://www.tibtech.com/conductivity.php last visited 2015-07-24.

[36] HyperPhysics: Magnetic properties of ferromagnetic materials. Last visited 2015-07-24. [Online]. Available: http://hyperphysics.phy-astr.gsu.edu/hbase/tables/magprop.html#c2

[37] HyperPhysics: Magnetic susceptibilities of paramagnetic and diamagnetic materials at 20 °C. Last visited 2015-07-24. [Online]. Available: http://hyperphysics.phy-astr.gsu.edu/hbase/tables/magprop.html

[38] J. C. Rautio, "The long road to Maxwell's equations. How four enthusiasts helped bring the theory of electromagnetism to light," *IEEE Spectrum*, Dec. 01, 2014, last visited 2015-11-04. [Online]. Available: http://spectrum.ieee.org/telecom/wireless/the-long-road-to-maxwells-equations

[39] H. Ammari, A. Buffa, and J.-C. Nédélec, "A justification of eddy currents model for the Maxwell equations," *SIAM J. Appl. Math.*, vol. 60, no. 5, pp. 1805–1823, May 2000. [Online]. Available: http://dx.doi.org/10.1137/S0036139998348979

[40] T. Bell, B. Barrow, and N. Khadr, "Shape-based classification and discrimination of subsurface objects using electromagnetic induction," in *Geoscience and Remote Sensing Symposium Proceedings, 1998. IGARSS '98. 1998 IEEE International*, vol. 1, Jul. 1998, pp. 509–513 vol.1.

[41] T. Bell, B. Barrow, J. Miller, and D. Keiswetter, "Time and frequency domain electromagnetic induction signatures of unexploded ordnance," *Subsurface Sensing Technologies and Applications*, vol. 2, no. 3, pp. 153–175, 2001. [Online]. Available: http://dx.doi.org/10.1023/A%3A1011978305379

[42] I. Won, D. Keiswetter, and T. Bell, "Electromagnetic induction spectroscopy for clearing landmines," *Geoscience and Remote Sensing, IEEE Transactions on*, vol. 39, no. 4, pp. 703–709, Apr. 2001.

[43] P. Gao, L. Collins, P. Garber, N. Geng, and L. Carin, "Classification of landmine-like metal targets using wideband electromagnetic induction," *Geoscience and Remote Sensing, IEEE Transactions on*, vol. 38, no. 3, pp. 1352–1361, May 2000.

[44] D. Williams, Y. Yu, L. Kennedy, X. Zhu, and L. Carin, "A bivariate Gaussian model for unexploded ordnance classification with EMI data," *Geoscience and Remote Sensing Letters, IEEE*, vol. 4, no. 4, pp. 629–633, Oct. 2007.

[45] M. Tran, C. Abeynayake, and L. Jain, "A target discrimination methodology utilizing Wavelet-based and morphological feature extraction with metal detector array data," *Geoscience and Remote Sensing, IEEE Transactions on*, vol. 50, no. 1, pp. 119–129, Jan. 2012.

[46] R. Chesney, Y. Das, J. McFee, and M. Ito, "Identification of metallic spheroids by classification of their electromagnetic induction responses," *Pattern Analysis and Machine Intelligence, IEEE Transactions on*, vol. PAMI-6, no. 6, pp. 809–820, Nov. 1984.

[47] H. Braunisch, C. Ao, K. O'Neill, and J. Kong, "Magnetoquasistatic response of conducting and permeable prolate spheroid under axial excitation," *Geoscience and Remote Sensing, IEEE Transactions on*, vol. 39, no. 12, pp. 2689–2701, Dec. 2001.

[48] J. Miller, T. Bell, J. Soukup, and D. Keiswetter, "Simple phenomenological models for wideband frequency-domain electromagnetic induction," *Geoscience and Remote Sensing, IEEE Transactions on*, vol. 39, no. 6, pp. 1294–1298, Jun. 2001.

[49] A. Sebak, L. Shafai, and Y. Das, "Near-zone fields scattered by three-dimensional highly conducting permeable objects in the field of an arbitrary loop," *Geoscience and Remote Sensing, IEEE Transactions on*, vol. 29, no. 1, pp. 9–15, Jan. 1991.

[50] A. Aliamiri, J. Stalnaker, and E. Miller, "Statistical classification of buried unexploded ordnance using nonparametric prior models," *Geoscience and Remote Sensing, IEEE Transactions on*, vol. 45, no. 9, pp. 2794–2806, Sep. 2007.

[51] C. E. Baum, "Low-frequency near-field magnetic scattering from highly, but not perfectly, conducting bodies," *Interaction note 499, Phillips Laboratory*, 1993.

[52] O. A. Abdel Rehim, J. L. Davidson, L. A. Marsh, M. D. O'Toole, D. W. Armitage, and A. J. Peyton, "Measurement system for determining the magnetic polarizability tensor of small metal targets," in *IEEE Sensors Applications Symposium*, Apr. 2015, pp. 23–27.

[53] HyperPhysics: Biot-Savart law. Last visited 2015-04-18. [Online]. Available: http://hyperphysics.phy-astr.gsu.edu/hbase/magnetic/biosav.html

[54] S. J. Norton, I. J. Won, and E. R. Cespedes, "Ordnance/clutter discrimination based on target eigenvalue analysis," *Subsurface Sensing Technologies and Applications*, vol. 2, no. 3, pp. 285–298, 2001. [Online]. Available: http://dx.doi.org/10.1023/A%3A1011930422217

[55] H. Ammari and H. Kang, *Polarization and moment tensors : with applications to inverse problems and effective medium theory*, ser. Applied mathematical sciences. New York: Springer, 2007. [Online]. Available: http://opac.inria.fr/record=b1125775

[56] J. A. Osborn, "Demagnetizing factors of the general ellipsoid," *Phys. Rev.*, vol. 67, pp. 351–357, Jun. 1945. [Online]. Available: http://link.aps.org/doi/10.1103/PhysRev.67.351

[57] H. Ammari, J. Chen, Z. Chen, J. Garnier, and D. Volkov, "Target detection and characterization from electromagnetic induction data," *Journal de Mathématiques Pures et Appliquées*, vol. 101, no. 1, pp. 54 – 75, 2014. [Online]. Available: http://www.sciencedirect.com/science/article/pii/S0021782413000792

[58] P. D. Ledger and W. R. B. Lionheart, "Characterizing the shape and material properties of hidden targets from magnetic induction data," *IMA Journal of Applied Mathematics*, 2015. [Online]. Available: http://imamat.oxfordjournals.org/content/early/2015/06/25/imamat.hxv015.abstract

[59] L. Carin, H. Yu, Y. Dalichaouch, A. R. Perry, P. V. Czipott, and C. E. Baum, "On the wideband EMI response of a rotationally symmetric permeable and conducting target." *IEEE T. Geoscience and Remote Sensing*, vol. 39, no. 6, pp. 1206–1213, 2001. [Online]. Available: http://dblp.uni-trier.de/db/journals/tgrs/tgrs39.html#CarinYDPCB01

[60] C. E. Baum, "Magnetic singularity identification of nonsymmetrical targets," *Interaction Note 549*, Dec. 1998. [Online]. Available: http://ece-research.unm.edu/summa/notes/In/0549.pdf

[61] S. J. Norton and I. J. Won, "Identification of buried unexploded ordnance from broadband electromagnetic induction data," *Geoscience and Remote Sensing, IEEE Transactions on*, vol. 39, no. 10, pp. 2253–2261, Oct. 2001.

[62] T. H. Bell, B. J. Barrow, and J. T. Miller, "Subsurface discrimination using electromagnetic induction sensors," *IEEE T. Geoscience and Remote Sensing*, vol. 39, no. 6, pp. 1286–1293, 2001.

[63] J. T. Smith and H. F. Morrison, "Estimating equivalent dipole polarizabilities for the inductive response of isolated conductive bodies," *Geoscience and Remote Sensing, IEEE Transactions on*, vol. 42, no. 6, pp. 1208–1214, Jun. 2004.

[64] B. Zhang, K. O'Neill, J. A. Kong, and T. M. Grzegorczyk, "Support vector machine and neural network classification of metallic objects using coefficients of the spheroidal MQS response modes," *Geoscience and Remote Sensing, IEEE Transactions on*, vol. 46, no. 1, pp. 159–171, Jan. 2008.

[65] F. Shubitidze, J. Fernandez, B. Barrowes, I. Shamatava, A. Bijamov, K. O'Neill, and D. Karkashadze, "The orthonormalized volume magnetic source model for discrimination of unexploded ordnance," *Geoscience and Remote Sensing, IEEE Transactions on*, vol. 52, no. 8, pp. 4658–4670, Aug. 2014.

[66] Massachusetts Institute of Technology, Dept. of Mech Eng. 2.14 Analysis and design of feedback control systems, lecture notes: Understanding poles and zeros. Last visited 2015-08-03. [Online]. Available: http://web.mit.edu/2.14/www/Handouts/PoleZero.pdf

[67] C. E. Baum, "On the singularity expansion method for the solution of electromagnetic interaction problems," DTIC Document, Tech. Rep., 1971.

[68] C. E. Baum, E. J. Rothwell, Y. F. Chen, and D. P. Nyquist, "The singularity expansion method and its application to target identification," *Proceedings of the IEEE*, vol. 79, no. 10, pp. 1481–1492, Oct. 1991.

[69] L. Riggs, J. Mooney, and D. Lawrence, "Identification of metallic mine-like objects using low frequency magnetic fields," *Geoscience and Remote Sensing, IEEE Transactions on*, vol. 39, no. 1, pp. 56–66, Jan. 2001.

[70] N. Geng, C. E. Baum, and L. Carin, "On the low-frequency natural response of conducting and permeable targets," *IEEE T. Geoscience and Remote Sensing*, vol. 37, no. 1, pp. 347–359, 1999. [Online]. Available: http://dx.doi.org/10.1109/36.739068

[71] A. B. Tarokh, E. L. Miller, I. J. Won, and H. Huang, "Statistical classification of buried objects from spatially sampled time or frequency domain electromagnetic induction data," *Radio Science*, vol. 39, no. 4, pp. n/a–n/a, 2004, rS4S05. [Online]. Available: http://dx.doi.org/10.1029/2003RS002951

[72] L. Collins, P. Gao, and L. Carin, "An improved Bayesian decision theoretic approach for land mine detection," *Geoscience and Remote Sensing, IEEE Transactions on*, vol. 37, no. 2, pp. 811–819, Mar. 1999.

[73] L. R. Pasion and D. W. Oldenburg, "Locating and determining dimensionality of UXO using time domain electromagnetic induction," in *Proc. SAGEEP*, 1999, pp. 763–772.

[74] S. Chilaka, D. Faircloth, L. Riggs, and H. Nelson, "Enhanced discrimination among UXO-like targets using extremely low-frequency magnetic fields," *Geoscience and Remote Sensing, IEEE Transactions on*, vol. 44, no. 1, pp. 10–21, Jan. 2006.

[75] G. Ramachandran, P. Gader, and J. Wilson, "GRANMA: Gradient angle model algorithm on wideband EMI data for land-mine detection," *Geoscience and Remote Sensing Letters, IEEE*, vol. 7, no. 3, pp. 535 – 539, Jul. 2010.

[76] M.-H. Wei, W. Scott, and J. McClellan, "Robust estimation of the discrete spectrum of relaxations for electromagnetic induction responses," *Geoscience and Remote Sensing, IEEE Transactions on*, vol. 48, no. 3, pp. 1169 – 1179, Mar. 2010.

[77] M.-H. Wei, J. McClellan, and W. Scott, "Estimation of the discrete spectrum of relaxations for electromagnetic induction responses using ℓ_p -regularized least squares for $0 \leq p \leq 1$," *Geoscience and Remote Sensing Letters, IEEE*, vol. 8, no. 2, pp. 233 – 237, Mar. 2011.

[78] S. L. Tantum, K. A. Colwell, K. D. Morton, W. R. Scott, L. M. Collins, and P. A. Torrione, "Feature extraction and processing of spatial frequency-domain electromagnetic induction sensor data for improved landmine discrimination," in *Proc. SPIE*, vol. 8357, 2012, pp. 835 708 – 835 708 – 8. [Online]. Available: http://dx.doi.org/10.1117/12.919421

[79] S. Tantum, W. Scott, K. Morton, L. Collins, and P. Torrione, "Target classification and identification using sparse model representations of frequency-domain electromagnetic induction sensor data," *Geoscience and Remote Sensing, IEEE Transactions on*, vol. 51, no. 5, pp. 2689 – 2706, May 2013.

[80] W. R. Scott, Jr. and G. D. Larson, "Measured dipole expansion of discrete relaxations to represent the electromagnetic induction response of buried metal targets," in *Proc. SPIE*, vol. 7664, 2010, pp. 76 640E – 76 640E – 11. [Online]. Available: http://dx.doi.org/10.1117/12.852669

[81] K. Krueger, W. R. Scott, and J. H. McClellan, "Location and orientation estimation of buried targets using electromagnetic induction sensors," in *Proc. SPIE*, vol. 8357, 2012, pp. 83 570D – 83 570D – 12. [Online]. Available: http://dx.doi.org/10.1117/12.919558

[82] F. Shubitidze, K. O'Neill, I. Shamatava, K. Sun, and K. Paulsen, "Fast and accurate calculation of physically complete EMI response by a heterogeneous metallic object," *Geoscience and Remote Sensing, IEEE Transactions on*, vol. 43, no. 8, pp. 1736 – 1750, Aug. 2005.

[83] Y. Zhang, L. Collins, H. Yu, C. E. Baum, and L. Carin, "Sensing of unexploded ordnance with magnetometer and induction data: theory and signal processing," *Geoscience and Remote Sensing, IEEE Transactions on*, vol. 41, no. 5, pp. 1005 – 1015, May 2003.

[84] H. Braunisch, C. Ao, K. O'Neill, and J. Kong, "Magnetoquasistatic response of a distribution of small conducting and permeable objects," in *Geoscience and Remote Sensing Symposium, 2000. Proceedings. IGARSS 2000. IEEE 2000 International*, vol. 4, 2000, pp. 1424 – 1426 vol.4.

[85] F. Shubitidze, J. P. Fernández, B. E. Barrowes, K. O'Neill, I. Shamatava, and A. Bijamov, "Comparison of the physically complete model with a simple dipole model for UXO detection and discrimination," in *Proc. SPIE*, vol. 7664, 2010, pp. 766 408 – 766 408 – 12. [Online]. Available: http://dx.doi.org/10.1117/12.850654

[86] A. Bijamov, J. Fernandez, B. Barrowes, I. Shamatava, K. O'Neill, and F. Shubitidze, "Camp Butner live-site UXO classification using hierarchical clustering and Gaussian mixture modeling," *Geoscience and Remote Sensing, IEEE Transactions on*, vol. 52, no. 8, pp. 5218–5229, Aug. 2014.

[87] B. Barrowes, K. O'Neill, T. Grzegorczyk, B. Zhang, and J. A. Kong, "Electromagnetic induction from highly permeable and conductive ellipsoids under arbitrary excitation: Application to the detection of unexploded ordnances," *Geoscience and Remote Sensing, IEEE Transactions on*, vol. 46, no. 4, pp. 1164–1176, Apr. 2008.

[88] L. A. Marsh, C. Ktistis, A. Järvi, D. W. Armitage, and A. J. Peyton, "Inversion of the Magnetic Polarisability Tensor at a Single Frequency from Walk-through Metal Detector Measurements," in *6th International Symposium on Process Tomography*, 2012.

[89] L. A. Marsh, C. Ktistis, A. Järvi, D. W. Armitage, and A. J. Peyton, "Three-dimensional object location and inversion of the magnetic polarizability tensor at a single frequency using a walk-through metal detector," *Measurement Science and Technology*, vol. 24, no. 4, p. 045102, Apr. 2013.

[90] HyperPhysics: Solenoid. Last visited 2015-04-17. [Online]. Available: http://hyperphysics.phy-astr.gsu.edu/hbase/magnetic/solenoid.html

[91] D. W. Marquardt, "An algorithm for least-squares estimation of nonlinear parameters," *SIAM Journal on Applied Mathematics*, vol. 11, no. 2, pp. 431–441, 1963. [Online]. Available: http://dx.doi.org/10.1137/0111030

[92] H. P. Gavin. The Levenberg-Marquardt method for nonlinear least squares curve-fitting problems. 2013. Last visited 2015-07-24. [Online]. Available: http://people.duke.edu/~hpgavin/ce281/lm.pdf

[93] L. Beran and D. Oldenburg, "Selecting a discrimination algorithm for unexploded ordnance remediation," *Geoscience and Remote Sensing, IEEE Transactions on*, vol. 46, no. 9, pp. 2547–2557, Sep. 2008.

[94] Federal Bureau of Investigation guide to concealable weapons. Last visited 2015-10-29. [Online]. Available: https://fas.org/irp/agency/doj/fbi/weapons.pdf

[95] J. P. Fernández, F. Shubitidze, I. Shamatava, B. E. Barrowes, and K. O'Neill, "Realistic subsurface anomaly discrimination using electromagnetic induction and an SVM classifier," *EURASIP J. Adv. Signal Process*, vol. 2010, pp. 15:1–15:11, Mar. 2010. [Online]. Available: http://dx.doi.org/10.1155/2010/305890

[96] F. Shubitidze, J. P. Fernandez, I. Shamatava, L. R. Pasion, B. E. Barrowes, and K. O'Neill, "Application of the normalized surface magnetic source model to a blind unexploded ordnance discrimination test," *Applied Computational Electromagnetics Society Journal*, vol. 25, no. 1, p. 89–98, 2010.

[97] N. Khadr, B. J. Barrow, T. H. Bell, and H. H. Nelson, "Target shape classification using electromagnetic induction sensor data," in *Proc. UXO Forum*, 1998. [Online]. Available: http://citeseerx.ist.psu.edu/viewdoc/download?doi=10.1.1.41.5558&rep=rep1&type=pdf

[98] B. Barrow and H. Nelson, "Model-based characterization of electromagnetic induction signatures obtained with the MTADS electromagnetic array," *Geoscience and Remote Sensing, IEEE Transactions on*, vol. 39, no. 6, pp. 1279–1285, Jun. 2001.

[99] R. E. Grimm and T. A. Sprott, "Model-based sensor design optimization for UXO classification," 2002. [Online]. Available: https://www.boulder.swri.edu/~grimm/UXO_Forum_02_grimm.pdf

[100] D. Ambruš, D. Vasić, and V. Bilas, "Model-based target classification using spatial and temporal features of metal detector response," in *Sensors Applications Symposium (SAS), 2015 IEEE*, Apr. 2015, pp. 1–6.

[101] J. P. Fernández, B. Barrowes, K. A. O'Neill, K. Paulse, I. Shamatava, F. Shubitidze, K. Sunin, J. T. Broach, R. S. Harmon, and J. H. Holloway, "Evaluation of SVM classification of metallic objects based on a magnetic-dipole representation," in *eds., Detection and Remediation Technologies for Mines and Minelike Targets XI, Proc. SPIE*, vol. 6217, 2006, p. 621703.

[102] H. Huang and I. Won, "Characterization of UXO-like targets using broadband electromagnetic induction sensors," *Geoscience and Remote Sensing, IEEE Transactions on*, vol. 41, no. 3, pp. 652–663, Mar. 2003.

[103] A. H. Trang, P. V. Czipott, and D. A. Waldron, "Characterization of small metallic objects and nonmetallic antipersonnel mines," vol. 3079, 1997, pp. 372–383. [Online]. Available: http://dx.doi.org/10.1117/12.280863

[104] S. Tantum and L. Collins, "A comparison of algorithms for subsurface target detection and identification using time-domain electromagnetic induction data," *Geoscience and Remote Sensing, IEEE Transactions on*, vol. 39, no. 6, pp. 1299–1306, Jun. 2001.

[105] A. Aliamiri, J. Stalnaker, and E. Miller, "A Bayesian approach for classification of buried objects using non-parametric prior model," in *Geoscience and Remote Sensing Symposium, 2006. IGARSS 2006. IEEE International Conference on*, Jul. 2006, pp. 3911–3914.

[106] L. R. Pasion, S. D. Billings, and D. W. Oldenburg, "UXO discrimination using time domain electromagnetic induction," in *UXO Forum*, 2001.

[107] C. Burges, "A tutorial on support vector machines for pattern recognition," *Data Mining and Knowledge Discovery*, vol. 2, no. 2, pp. 121–167, 1998. [Online]. Available: http://dx.doi.org/10.1023/A%3A1009715923555

[108] C.-W. Hsu and C.-J. Lin, "A comparison of methods for multiclass support vector machines," *Neural Networks, IEEE Transactions on*, vol. 13, no. 2, pp. 415–425, Mar. 2002.

[109] B. Fei and J. Liu, "Binary tree of SVM: a new fast multiclass training and classification algorithm," *Neural Networks, IEEE Transactions on*, vol. 17, no. 3, pp. 696–704, May 2006.

[110] K. Sun, K. O'Neill, L. Liu, F. Shubitidze, I. Shamatava, and K. D. Paulsen, "Analytical solutions for EMI scattering from general spheroids with application in signal inversion for UXO identification," vol. 5089, 2003, pp. 1035–1045. [Online]. Available: http://dx.doi.org/10.1117/12.487240

[111] E. B. Fails, P. A. Torrione, W. R. Scott, and L. M. Collins, "Performance of a four parameter model for modeling landmine signatures in frequency domain wideband electromagnetic induction detection systems," in *Proc. SPIE*, vol. 6553, 2007, pp. 65 530D–65 530D–8. [Online]. Available: http://dx.doi.org/10.1117/12.719460

[112] H. Huang and I. Won, "Automated identification of buried landmines using normalized electromagnetic induction spectroscopy," *Geoscience and Remote Sensing, IEEE Transactions on*, vol. 41, no. 3, pp. 640–651, Mar. 2003.

[113] J. E. Mcfee and Y. Das, "A classifier for feature vectors whose prototypes are a function of multiple continuous parameters," *Pattern Analysis and Machine Intelligence, IEEE Transactions on*, vol. 10, no. 4, pp. 599–606, Jul. 1988.

[114] R. Moskowitz and E. Della Torre, "Theoretical aspects of demagnetization tensors," *Magnetics, IEEE Transactions on*, vol. 2, no. 4, pp. 739–744, Dec 1966.

[115] J. Remus, K. Morton, P. Torrione, S. Tantum, and L. Collins, "Comparison of a distance-based likelihood ratio test and k-nearest neighbor classification methods," in *Machine Learning for Signal Processing, 2008. MLSP 2008. IEEE Workshop on*, Oct. 2008, pp. 362–367.

[116] S. A. Dudani, "The distance-weighted k-Nearest-Neighbor rule," *Systems, Man and Cybernetics, IEEE Transactions on*, vol. SMC-6, no. 4, pp. 325–327, Apr. 1976.

[117] S. L. Tantum, K. A. Colwell, W. R. Scott, P. A. Torrione, L. M. Collins, and K. D. Morton, "Sparse model inversion and processing of spatial frequency-domain electromagnetic induction sensor array data for improved landmine discrimination," vol. 8709, 2013, pp. 87 091E–87 091E–8. [Online]. Available: http://dx.doi.org/10.1117/12.2016063

[118] J. Remus and L. Collins, "Phenomenolgical model inversion with Fisher information metrics for unexploded ordnance detection," in *Geoscience and Remote Sensing Symposium (IGARSS), 2010 IEEE International*, Jul. 2010, pp. 691–694.

[119] S. E. Walker, L. R. Pasion, D. W. Oldenburg, and S. D. Billings, "Investigating the effect of data quality on time domain electromagnetic discrimination," *Journal of Applied Geophysics*, vol. 61, no. 3–4, pp. 254 – 278, 2007, state-of-the-Art {UXO} Detection and Characterization. [Online]. Available: http://www.sciencedirect.com/science/article/pii/S0926985106001005

[120] T. M. Grzegorczyk, B. Barrowes, F. Shubitidze, J. P. Fernández, I. Shamatava, and K. A. O'Neill, "Kalman filters applied to the detection of unexploded ordnance," vol. 7664, 2010, pp. 766 402–766 402–9. [Online]. Available: http://dx.doi.org/10.1117/12.848564

[121] L. Beran, S. Billings, and D. Oldenburg, "Incorporating uncertainty in unexploded ordnance discrimination," *Geoscience and Remote Sensing, IEEE Transactions on*, vol. 49, no. 8, pp. 3071–3080, Aug. 2011.

[122] V. J. Hodge and J. Austin, "A survey of outlier detection methodologies," *Artificial Intelligence Review*, vol. 22, no. 2, pp. 85–126, 2004. [Online]. Available: http://dx.doi.org/10.1007/s10462-004-4304-y

[123] A. R. Al-Qubaa, G. Y. Tian, and J. Wilson, "Electromagnetic imaging system for weapon detection and classification," in *SENSORCOMM 2011 : The Fifth International Conference on Sensor Technologies and Applications*, 2011, pp. 317–321. [Online]. Available: https://www.thinkmind.org/download.php?articleid=sensorcomm_2011_12_40_10257

[124] A. Al-Qubaa and G. Tian, "Automatic threat object classification based on extracted features from electromagnetic imaging system," in *Imaging Systems and Techniques (IST), 2012 IEEE International Conference on*, Jul. 2012, pp. 164–169.

[125] W. Hu, S. Tantum, and L. Collins, "EMI-based classification of multiple closely spaced subsurface objects via independent component analysis," *Geoscience and Remote Sensing, IEEE Transactions on*, vol. 42, no. 11, pp. 2544–2554, Nov. 2004.

[126] D. Economou, F. Shubitidze, B. Barrowes, and N. Uzunoglu, "MUSIC algorithm applied to advanced EMI sensors data for UXO classification," in *Electromagnetics in Advanced Applications (ICEAA), 2011 International Conference on*, Sep. 2011, pp. 1160–1163.

[127] J. Remus and L. Collins, "Matching pursuits decomposition for discrimination of unexploded ordnance: Isolated and overlapping signatures," in *Geoscience and Remote Sensing Symposium, 2008. IGARSS 2008. IEEE International*, vol. 2, Jul. 2008, pp. II–21–II–24.

[128] T. M. Grzegorczyk, B. E. Barrowes, F. Shubitidze, J. P. Fernandez, and K. O'Neill, "Simultaneous identification of multiple unexploded ordnance using electromagnetic induction sensors," *Geoscience and Remote Sensing, IEEE Transactions on*, vol. 49, no. 7, pp. 2507–2517, Jul. 2011.

[129] L. A. Marsh, C. Ktistis, A. Järvi, D. W. Armitage, and A. J. Peyton, "Determination of the magnetic polarizability tensor and three dimensional object location for multiple objects using a walk-through metal detector," *Measurement Science and Technology*, vol. 25, no. 5, p. 055107, 2014. [Online]. Available: http://stacks.iop.org/0957-0233/25/i=5/a=055107

[130] A. Benavides, M. E. Everett, and C. Pierce Jr, "Unexploded ordnance discrimination using time-domain electromagnetic induction and self-organizing maps," *Stochastic Environmental Research and Risk Assessment*, vol. 23, no. 2, pp. 169–179, 2009. [Online]. Available: http://dx.doi.org/10.1007/s00477-007-0211-5

[131] Q. Liu, X. Liao, and L. Carin, "Detection of unexploded ordnance via efficient semisupervised and active learning," *Geoscience and Remote Sensing, IEEE Transactions on*, vol. 46, no. 9, pp. 2558–2567, Sep. 2008.

[132] J. Makkonen, R. Kerminen, I. D. D. Curcio, S. Mate, and A. Visa, "Detecting events by clustering videos from large media databases," in *Proceedings of the 2nd ACM International Workshop on Events in Multimedia*, ser. EiMM '10. New York, NY, USA: ACM, 2010, pp. 9–14. [Online]. Available: http://doi.acm.org/10.1145/1877937.1877942

[133] L. R. Pasion, S. D. Billings, D. W. Oldenburg, and S. E. Walker, "Application of a library based method to time domain electromagnetic data for the identification of unexploded ordnance," *Journal of Applied*

Geophysics, vol. 61, no. 3–4, pp. 279 – 291, 2007. [Online]. Available: http://www.sciencedirect.com/science/article/pii/S0926985106001017

Publications

Publication I

Makkonen J., Marsh L. A., Vihonen, J., Visa, A., Järvi, A., Peyton, A. J. "Classification of metallic targets using a single frequency component of the magnetic polarisability tensor", *Journal of Physics: Conference Series, 450(1):012038, IOP Sensors & their Applications, Dubrovnik, Croatia, 2013.*
dx.doi.org/10.1088/1742-6596/450/1/012038

Classification of metallic targets using a single frequency component of the magnetic polarisability tensor

J Makkonen[1,4], L A Marsh[2], J Vihonen[1], A Visa[1], A Järvi[3] and A J Peyton[2]

[1] Tampere University of Technology, Department of Signal Processing, Korkeakoulunkatu 10, P.O. Box 553, FIN-33101 Tampere, Finland
[2] School of Electrical and Electronic Engineering, The University of Manchester, Manchester, M13 9PL, UK
[3] Rapiscan Systems Oy, Klovinpellontie 3, Torni 2, FIN-02180 Espoo, Finland

E-mail: jarmo.makkonen@tut.fi

Abstract. A k-nearest neighbour (KNN) classification algorithm has been added to a walk-through metal detection system which is capable of inverting the magnetic polarisability tensor of metallic targets at a frequency of 10 kHz. Pre-computed library data is used to determine the class of the object, e.g. 'knife' or 'mobile phone', and is consequently capable of determining if an object is considered a threat. The results presented show a typical success rate of 95%. An investigation into classification accuracy between different candidates is also presented to determine the significance of the *body effect* on the success of the classification.

1. Introduction

Modern walk-through metal detectors are incredibly sensitive, precision measurement systems. Their widespread use for detection of threats in environments such as airports, prisons and public buildings, combined with the competition between several leading manufacturers has ensured that the current generation of technology is capable of detecting very small items such as handcuff keys and integrated circuits [1]. In the aviation industry metallic threats are principally considered to be knives and guns and are thus considerably larger than the smallest detectable objects. Improved signal-to-noise ratios may continue to be sought by manufacturers in an attempt to increase the detectability of non-magnetic, low conductivity materials such as some stainless steels, however the most significant challenge is no longer to detect the objects, but to determine whether they present a threat or not.

It is reported that between 2000 and 2010 a total of 17 out of an estimated 310 million commercial flights were hijacked worldwide [2]. Using these numbers it is estimated that in this ten year period the chances of a plane being hijacked was in the region of 1 in 18.2 million. This statistically rare threat can be contrasted with the fact that in environments such as airports it is common for people to carry several innocuous items such as mobile phones, jewellery, or keys, and current regulations require that travellers must remove these items prior to screening. This causes a great deal of disruption and inconvenience, and requires a large number of staff to administer. These facts demonstrate that any method capable of determining which items located on a person are threatening, and which are innocuous has the potential to greatly improve the aviation industry.

[4] To whom any correspondence should be addressed.

In this study, a tomographic metal detection system [3] which is capable of inverting the magnetic polarisability tensor, $\overleftrightarrow{\mathbf{M}}$, from a single walk-through scan has been used as the measurement system. A library of tensors produced by this system has been recorded for a variety of different objects. To examine the capacitive and inductive effect of the human body on the measurements, known as the *body effect*, a separate library using two candidates has been collected. A classification algorithm based on the k-nearest neighbour (KNN) approach has been implemented, and the performance of the algorithm is tested for both the general library case, and the body effect case.

Although the method which is reported here is done so with focus on the aviation industry, the methods documented in this paper may be applied to any system which is capable of yielding the magnetic polarisability tensor; including detection systems for UXO/landmines.

2. Method

2.1. Producing the library

The library was constructed by simple walkthroughs using the WTMD described in [3]. This system uses eight pairs of transmit-receive coils, each of which operate at a different frequency. These frequencies range from 8 kHz to 13.8 kHz and are arranged lowest to highest from floor level upwards, with a separation of approximately 700 Hz between neighbouring channels. The system inverts a single tensor, and consequently offers only a single point on the tensor's continuously varying frequency spectrum [5]. Theoretically the inverted tensor is valid at the frequency corresponding to the parallel channel which is level with the object, however to for simplification and as the range of operating frequencies is relatively small the tensors are assumed to correspond to a frequency of 10 kHz – the median frequency value centred about the average height of candidates.

The library was constructed by repeatedly conducting walkthrough measurements. One object was carried through the detector at a time per scan, and its orientation and position on the candidate was varied between scans. The library contains a total of 33 different objects, and was built using data from 1316 walk-through scans. These scans were conducted using three different candidates. The objects belong to 10 different classes which are shown below. Numbers in brackets represent the total number of measurements per class.

- **Belts (40)**
  - *1 belt*
- **Coins (80)**
  - *3 sets of coins*
- **Keys (90)**
  - *3 sets of keys*
- **Knives (424)**
  - *11 knives*
- **MP3 Players (80)**
  - *4 MP3 players*
- **Pocket Mirrors (50)**
  - *1 pocket mirror*
- **Mobile Phones (120)**
  - *4 mobile phones*
- **Wristwatches (40)**
  - *1 wristwatch*
- **Guns and gun parts (352)**
  - *2 guns*
  - *1 set of bullets*
- **Scissors (40)**
  - *1 pair of nail scissors*
  - *1 pair of office scissors*

The data recorded for each walk-through consists of the estimated tensor value, $\breve{\mathbf{M}}$, the residual of the inversion algorithm, r, and the estimated coordinates for the path of the object, $\mathbf{P}$. The main library, subsequently referred to as '*Main, all'* contains of all the recorded measurements.

A second library, called *'Reduced'*, was produced which consisted of a single object per class. This was done to balance the probability of classification, as the outcome of KNN algorithms is known to be dependent upon the number of samples per class. The data consisted of measurements from two different locations, in the left trouser pocket and along the central line of the portal at chest height; these are labelled *'Left pocket'* and *'Chest'*. At each position, 10 scans were performed, resulting in 20 measurements for each object. Thus, the total size of this second library was 200 measurements.

Previous testing with a calibration object has indicated that some tensor components deviate by up to 50% when the same object is scanned in different regions of the portal. Typically this variation occurs as the object trajectory moves from one side panel of the detector to the other. In order to demonstrate this effect and to evaluate the performance of the KNN algorithm in such circumstances, the results from the *'Chest'* and '*Left pocket'* libraries described above have been compared.

Tensor reliability can be estimated from the residual value, *r*, of the inversion algorithm described in [3]. The residual is calculated by taking the L2-norm of the difference between the actual measurements, ρ, and the forward response as a function of the inverted tensor and 3D coordinates, $\hat{\rho}$, and dividing this value by the L2-norm of the inverted measurements, $\hat{\rho}$; this is defined in (1).

$$r = \frac{\sqrt{\sum_{k=1}^{n} \left| \rho_k - \hat{\rho}_k \right|^2}}{\sum_{k=1}^{n} \left| \hat{\rho}_k \right|^2} \tag{1}$$

Experience has shown that residual values greater than 0.50 indicate unreliable tensors, and that anything in excess of 0.35 can be considered to be a poor representation of the object's tensor. As a result of this observation a further two versions of each library have been created. These have been made by selecting all of the samples that have a residual less than 0.5 and 0.35. The libraries are called *'X, r < 0.5'* and *'X, r < 0.35'* respectively, where *X* represents the base library name.

A total of ten objects were used to construct the library for investigation of the body effect, five of which were threat objects and the remaining five were innocuous ones. The threat objects were the aluminium and steel NIJ handguns [6] and three knives - *Opinel Lame Acier 12*, the *Opinel Inox 8* and a large kitchen knife with a stainless steel blade.

Two adult candidates of substantially differing heights were used to conduct this experiment. Candidate A had a height of 1.86 m and candidate B had a height of 1.55 m. Each person performed the same number of walkthroughs, 10 for each object, which resulted in 100 measurements per candidate. The object location was chosen to be central with respect to the distance between the side panels, and at chest height of candidate A. The same height was maintained for candidate B, resulting in keeping the object at approximately neck level.

Figure 1 shows a typical response of how the inverted tensors vary with different candidates. The different colours represent the two candidates, and the different markers represent the three different eigenvalues. The two test objects, made of aluminium and stainless steel, in the case shown represent guns. Due to the clustering of the points for each candidate it is believed that the differences correspond to the body effect rather than noise from the inversion algorithm.

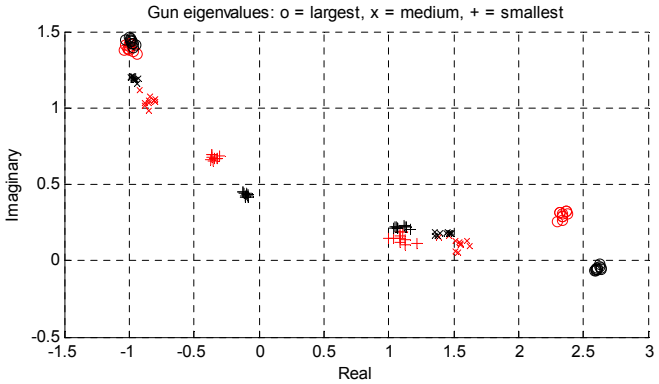

Figure 1. Body effect on eigenvalues

2.2. Implementation of the algorithm

The method is based on the classification algorithm presented in [4]. The magnetic polarisability tensor, $\overleftrightarrow{\mathbf{M}}$, takes the form of a complex, symmetric 3×3 matrix as shown below:

$$\overleftrightarrow{\mathbf{M}}(f) = \begin{bmatrix} M_{11} + jN_{11} & M_{12} + jN_{12} & M_{13} + jN_{13} \\ M_{12} + jN_{12} & M_{22} + jN_{22} & M_{23} + jN_{23} \\ M_{13} + jN_{13} & M_{23} + jN_{23} & M_{33} + jN_{33} \end{bmatrix}$$

The algorithm firstly calculates the eigenvalues of the tensor, $\vec{\lambda}$. These eigenvalues are a rotation-invariant representation of $\vec{\mathbf{M}}$. As $\vec{\mathbf{M}}$ is complex its eigenvalues form a vector containing three complex values. These three values are then sorted in order of increasing magnitude, $\vec{\lambda}_s$. The magnitude is calculated by multiplying each value by its complex conjugate.

Each object is classified by using (2) to compare the Euclidean distance, D_i between the object's sorted eigenvalues and all of the samples in the library, where the subscript *i* refers to the library index. The vector of distances is sorted in order of smallest to largest values to produce $\vec{\mathbf{S}}$, and the first K values are selected. The classification outcome, ζ, is calculated by taking the statistical mode, Mo(), of the class of each of the K nearest distances as shown in (3); often *K* is an odd number to reduce the chances of even numbers of neighbours belonging to different, most popular classes.

$$D_i\left(\vec{\lambda}_a, \vec{\lambda}_b\right) = \sqrt{\left(\lambda_{a1} - \lambda_{b1}\right)^2 + \left(\lambda_{a2} - \lambda_{b2}\right)^2 + \left(\lambda_{a3} - \lambda_{b3}\right)^2} \tag{2}$$

$$\zeta = \mathrm{Mo}\left(\mathrm{Class}\left\{S_1 \quad \ldots \quad \ldots \quad S_k\right\}\right) \tag{3}$$

The results of the classification are evaluated according to two criteria. Firstly, by the accuracy of determining whether an object is considered to be threatening or innocuous, and secondly, by the accuracy of correctly identifying which of the 10 classes the object belongs to. Normalised values for the latter case have also been calculated to correct for differences in class sizes. This is defined as the average recall for all classes.

False negatives, i.e. classifying an object as innocuous when it is really a threat, are not acceptable in the application area. Therefore, the threat recall score should be 100% while still maintaining an acceptable level of overall accuracy. In a security screening application, this means that all threats are spotted while maintaining a low false alarm rate.

2.3. Limitations of the method

The results presented in this paper consider only situations where a single metallic object is within the detection volume of the portal. The classification algorithm would theoretically perform equally well regardless of how many objects are detected, providing that the quality of all tensors remains the same. The case of multi-object classification remains untested for measured data.

Although the algorithm utilises the tensor approximation (which is location invariant), and tensor eigenvalues (which are rotation invariant), the inversion algorithm is sensitive to certain locations within the detector space and also to variations in orientation as the object passes through the detector. In addition to this, it is known that the orthogonal field components are not of equal magnitude, and that as a result the direction with respect to floor-to-ceiling displacement tends to be noisier. Also, the areas at the very top and very bottom of the detector have a reduced concentration of coils, and consequently the tensor quality decreases in these regions. The effect on the classification outcome can be equated to that of cases with large residual values (typically $r > 0.35$).

As a final point it should be noted that KNN algorithms are highly dependent upon the underlying example library. If the library is not exhaustive, samples that are numerically far away from all of the examples tend to be classified as the class that has the most examples.

3. Results and Discussion

The results of the KNN are shown in Table 1. The algorithm was run once for each library with the parameter value K=1. For the library *'Main, all'* the algorithm was run also with parameter values K=3 and K=5. Leave-one-out cross validation was used, unless stated otherwise. The results show that the classifier performance seems to be the best with K=1 when the library *'Main, all'* is used. This is most likely due to the fact that there are only a few samples from some classes and a large number of samples from others. As discussed previously this is a limitation of KNN.

Table 1. Full results of experiment.

Library	K	Accuracy (%), threat/innoc.	Accuracy (%), class	Accuracy (%), class, norm.	Recall (%), threat
Main, all	1	98.9	97.6	96.0	99.4
Main, all	3	98.3	97.1	94.9	99.4
Main, all	5	98.6	96.7	94.1	99.5
Main, R < 0.5	1	99.3	98.9	97.9	99.8
Main, R < 0.35	1	99.5	99.0	97.7	99.7
Chest	1	99.3	97.4	97.4	99.0
Chest, R < 0.5	1	100	99.7	99.8	100
Chest, R < 0.35	1	100	99.4	98.6	100
Left Pocket	1	99.6	96.7	97.2	100
Left Pocket, R < 0.5	1	100	98.1	98.3	100
Left Pocket, R < 0.35	1	100	97.5	97.4	100
Reduced	1	100	98.5	98.5	100
Body Effect, all^	1	100	98.5	97.9	100
Body Effect, all*	1	96.5	88.0	82.9	100
Candidate A	1	100	100	100	100
Candidate B	1	100	97.0	95.7	100

^ based on a 'leave-one-out' classification approach
* based on a classification of Candidate A's measurements using Candidate B's library data and vice versa

Table 1 shows that the classifier appears to execute properly with all of the libraries tested. Recall is 99% or higher for all tested libraries; from a practical point of view this value needs to be higher to prevent security breaches, however this could be improved by improving the complexity of the classification algorithm, and also by biasing the threat objects in the library.

The testing with Candidates A and B shows that the body effect seems to be noticeable in classification results. In the results the recall of threat objects remained at the required value of 100%, however the ability to classify the objects fell substantially. Also, there were a greater number of false positive classifications where innocuous objects were misclassified as threats. In the testing, the performance was reduced when the library and test data was swapped such that the library was for Candidate A's data, whilst Candidate B was being scanned, and vice versa.

It can be seen that removing high residual samples generally improves the performance by a noticeable amount, cutting down misclassifications by 36-55%. However, it can be noticed that in some instances the removal of all samples with a residual higher than 0.35 does not improve performance. This is because there are fewer examples of some object classes such as keys and coins that tend to yield noisy tensor values. This causes bias towards the classes with a higher number of examples, and larger items which are more readily detectable.

The results show that, as expected, the classifier performs better when using only data from a single location, e.g. pocket data, instead of using a mixed set of data.

4. Conclusions and Future Work

The results of this study show that the modified KNN algorithm is capable of classifying targets consistently and with a typical normalised accuracy of over 95%, and a recall value of in excess of 99%. Based on this, it is clear that this improvement shows great promise to the field of inductive

metal detection. However, there are a number of improvements that could be made to this algorithm and there is further research which can be conducted which the authors expect would improve the results shown here.

As previously discussed, the KNN approach is a relatively simple algorithm which is subject to several limitations. It is probable that the success of the method reported here could be improved by implementing a more complex algorithm. One way to enhance the method is to use heuristics and the 3D location information of the metallic object that is given by the detector system. For example, if an object was to be classified as a wristwatch, then statistically it is very unlikely that it would be near the floor level. Also, given the variation in tensor components as a function of location within the detector, the location information of the object to be classified could be used to increase the trust in those object samples in the library that have been recorded from the same region of the detector space. An extra level of validation could be added to the algorithm which would take this into account, thereby improving the result.

The results presented in this paper indicate that the detector and classifier are sensitive to substantial changes in the body size of the candidate. Even if samples were to be recorded in the absence of the candidate, e.g. with a robotic arm, there is still a correction that must be made for the body effect. One possible way to reduce this capacitive coupling would be to introduce screening between the coils and the person being measured. Although this paper has shown that the classification remains successful regardless of the contribution of the body effect from the candidate, further study is needed to determine the extent of this effect and how it may be overcome.

Given the strong frequency dependency of the tensor, it is considered that the most significant adaptation which could be made to improve the effectiveness of the classification algorithm would be to use the broadband tensor components rather than those at a fixed frequency; the classification would be fitting a curve rather than a single point. This remains a topic for future research.

5. References

[1] Rapiscan Systems (2012, 13/02/2013) Metor 6S| Rapiscan Systems. Available: http://www.rapiscansystems.com/en/products/item/metor_6s

[2] Bodington, T (2011, 13/02/2013) Is the perceived threat of terrorism greater than the actual threat?, Available: http://www.tsvc.lincoln.ac.uk/papers/submission.php?paper=118

[3] Marsh L A, Ktistis K, Järvi A, Armitage D W and Peyton A J 2013 Three-dimensional object location and inversion of the magnetic polarisability tensor at a single frequency using a walk-through metal detector *Meas. Sci. Technol.* vol. 24 045102 doi:10.1088/0957-0233/24/4/045102

[4] Kauppila J, Ala-Kleemola T, Vihonen J, Jylhä J, Ruotsalainen M, Järvi A and Visa A, 2009 Classification of items in a walk-through metal detector using time series eigenvalues of the polarizability tensor *Proc. SPIE 7303, Detection and Sensing of Mines, Explosive Objects, and Obscured Targets XIV*, pp. 73030P-1~73030P-10

[5] Norton S J and Won I J, 2001 Identification of Buried Unexploded Ordnance From Broadband Electromagnetic Induction Data *IEEE Trans. Geosci. Remote Sens,* vol. 39, pp. 2253-2261

[6] Paulter N and Larson D 2009 NIJ Metal Detector Test Objects Report, National Institute for Justice, Gaithersburg, Maryland

Acknowledgments

This work was supported by the Academy of Finland under the project “Magnetic Induction and Data Analyses for Sophisticated Sensing”, grant no. 251777. The authors are also very grateful to Sarah Penny at the University of Manchester for her participation in this experiment.

Publication II

Makkonen J., Marsh L. A., Vihonen, J., Järvi, A., Armitage, D. W., Visa, A., Peyton, A. J. "KNN Classification of Metallic Targets using the Magnetic Polarizability Tensor", *Measurement Science and Technology, 25(5):055105, 2014.*
dx.doi.org/10.1088/0957-0233/25/5/055105

IOP Publishing Measurement Science and Technology
Meas. Sci. Technol. **25** (2014) 055105 (9pp) doi:10.1088/0957-0233/25/5/055105

KNN classification of metallic targets using the magnetic polarizability tensor

J Makkonen[1], L A Marsh[2], J Vihonen[1], A Järvi[3], D W Armitage[2], A Visa[1] and A J Peyton[2]

[1] Tampere University of Technology, Department of Signal Processing, Korkeakoulunkatu 10, PO Box 553, FI-33101 Tampere, Finland
[2] School of Electrical and Electronic Engineering, The University of Manchester, Manchester, M13 9PL, UK
[3] Rapiscan Systems Oy, Klovinpellontie 3, Torni 2, FI-02180 Espoo, Finland

E-mail: jarmo.makkonen@tut.fi

Received 20 September 2013, revised 7 January 2014
Accepted for publication 15 January 2014
Published 27 March 2014

Abstract

Walk-through metal detectors are used at check points for preventing personnel and passengers from carrying threatening metallic objects, such as knives and guns, into a secure area. These systems are capable of detecting small metallic items, such as handcuff keys and blades, but are unable to distinguish accurately between threatening objects and innocuous items. This paper studies the extent to which a K-nearest-neighbour classifier can distinguish various kinds of metallic objects, such as knives, shoe shanks, belts and containers. The classifier uses features extracted from the magnetic polarizability tensor, which represents the electromagnetic properties of the object. The tests include distinguishing threatening objects from innocuous ones, classifying a set of objects into 13 classes, and distinguishing between several similar objects within an object class. A walk-through metal detection system is used as source for the test data, which consist of 835 scans and 67 objects. The results presented show a typical success rate of over 95% for recognizing threats, and over 85% for correct classification. In addition, we have shown that the system is capable of distinguishing between similar objects reliably. Overall, the method shows promise for the field of security screening and suggests the need for further research.

Keywords: eigenvalues, KNN, classification

(Some figures may appear in colour only in the online journal)

1. Introduction

Walk-through metal detectors (WTMDs) are used in environments such as airports, prisons and public buildings for detection of threat objects. Their widespread use, combined with the competition between several leading manufacturers, has ensured that the current generation of technology is capable of detecting very small items such as handcuff keys and integrated circuits [1]. In the aviation industry, metallic threats are principally considered to be knives, guns and gun parts. They are thus considerably larger than the smallest detectable objects. Improved signal-to-noise ratios may continue to be sought by manufacturers in an attempt to increase the detectability of non-magnetic, low conductivity materials such as some stainless steels, however the most significant challenge is no longer to detect the objects, but to determine whether they present a threat or not.

It is reported that between 2000 and 2010 a total of 17 out of an estimated 310 million commercial flights were hijacked worldwide [2]. Using these numbers, it is estimated that in this ten year period the chances of a plane being hijacked was in the region of 1 in 18.2 million. In contrast to this threat, in environments such as airports, it is common for people to carry several innocuous items containing metal, such as mobile phones, jewellery and keys. Current regulations require that travellers must remove these items prior to WTMD screening. This causes a degree of disruption and inconvenience, and

requires a large number of staff to administer. Any method capable of reliably recognizing the items located on a person can remove the need for manual inspections, or even make it possible to be screened without removing metallic items. To the best of our knowledge, there are few published studies on performing an intelligent classification apart from [3].

This paper describes a K-nearest-neighbour (KNN) based classifier algorithm, first proposed by [3], and studies the extent to which it can distinguish between different objects that may typically be encountered with a WTMD. This is demonstrated with several test cases. Real walk-through data are used for the testing. An advanced metal detection system [4], which is capable of calculating the position and magnetic polarizability tensor, $\overleftrightarrow{\mathbf{M}}$, of one or more metallic objects from a single walk-through scan, has been used as the WTMD and the measurement system. A library of tensors produced by this system has been recorded for a variety of different objects.

The purpose of this paper is to investigate the potential of the methods proposed above using data from the WTMD portal. The portal is the first of its type and the deviation in the tensor components between different object locations and orientations can be significant. However, in theory, the eigenvalues for measured object tensors are considered to be rotation and location invariant, as discussed in section 3.2. Hence, we work under this assumption and use measurements from a single location and object orientation known to yield results with good signal-to-noise ratio; these results should then be generalizable for other locations and orientations.

The data library used in this paper is not exhaustive. The classes have been chosen arbitrarily, but are a representative sample of the range of objects that are commonly carried by people. Moreover, the classes contain only a sparse sample of the range of objects that might be included in a real world scenario. Finally, the overall number of measurements is considered to be sufficient to prove whether further collection of a larger library is justifiable.

The rest of the paper is organized as follows. The following section contains background and work related to this study. The third section describes the experimental system, i.e. WTMD and tensor inversion, along with the data library for the study. The fourth section presents the method. The fifth section describes the experimental results while the sixth section discusses the results. Finally, section 7 concludes the paper and provides suggestions for future research. Although the focus of this paper is on the aviation industry, the methods documented may be applied to other types of metal detection systems capable of yielding the magnetic polarizability tensor, e.g. detection systems for unexploded ordnance (UXO) and landmines.

2. Background

WTMDs have been in use since the 1970s, and technical development has lead them to be highly accurate systems. However, there have been few attempts to add intelligence to them. Steps to this direction have been taken by Kauppila *et al* [3], and Marsh *et al* [4] that have made it possible to determine the polarizability tensor and the path of a metallic object passing through a real working WTMD. This is based on an inversion algorithm that is covered in section 3.2.

Pattern classification is an old research problem, and its theory has developed throughout decades. The KNN classifier is one of the simplest and most well-known algorithms for this, and countless modifications have been made to it for tackling a variety of classification problems. It is easy to implement, needs only few parameters, and it can be applied to many kinds of data. Also, the algorithm is capable of modelling arbitrary decision surfaces based on the data. However, its performance is highly dependent on the underlying example library, which has to be large enough. The large database might lead to slow classification performance and increased system memory requirements. Moreover, performance depends on the explicitly defined distance function that is used for comparing samples [5].

KNN has been applied to landmine and UXO detection by Fails *et al* and Tantum *et al* [6, 7]. Compared to our work, these use distinct methods of characterizing the electromagnetic responses of the objects. Bell *et al* [8] and Norton *et al* [9] have used eigenvalues of the magnetic polarizability tensor for distinguishing between UXO and clutter, but have not used KNN for the classification. Kauppila *et al* [3] have extended the idea and used a KNN classifier for classifying the eigenvalues. We use the same algorithm, but on a more advanced WTMD system.

3. The walk-through metal detector measurement system

This section provides background information on the measurement system, the inversion algorithm and their use for measurements. Together they provide the data for the study. The WTMD measurement system will be referred to as *the portal*. It should be noted that the method reported in this paper may be used with any system capable of consistently inverting the magnetic polarizability tensor.

3.1. The portal hardware

The WTMD described in [4] was used as a data acquisition system. This system uses 16 coils, 8 of which are transmitters which operate at different frequencies. These frequencies range from 8 to 13.8 kHz and are arranged from lowest to highest from floor level upwards, with a separation of approximately 700 Hz between neighbouring channels. The coil geometry, along with the portal, is shown in figure 1. The system is capable of taking 320 complex measurements per second across this detector volume and is capable of inverting the magnetic polarizability tensor to a typical accuracy of 10% within 5 s of a single walk-through scan.

3.2. Tensor inversion

The system measures the change in signal caused by objects passing through the portal space. We would like to get information on the characteristics of the object, i.e. its material, size and shape. To achieve this, we estimate what kind of an

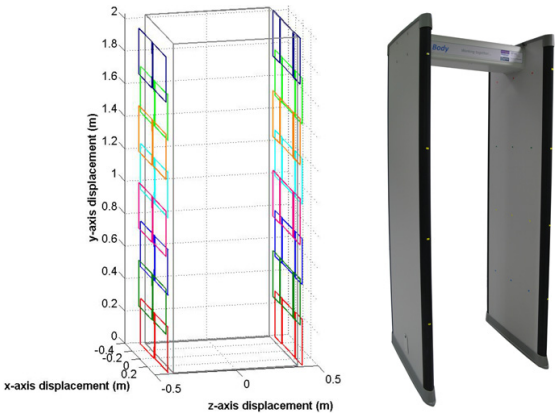

Figure 1. Left: coil geometry of WTMD data acquisition system. Right: the portal hardware.

object could have caused the measured change in signal. For this purpose, we use a magnetic polarizability tensor model. It refers typically to a complex-valued symmetrical 3-by-3 matrix

$$\overleftrightarrow{\mathbf{M}}(f) = \begin{bmatrix} m_{x,x} & m_{x,y} & m_{x,z} \\ m_{y,x} & m_{y,y} & m_{y,z} \\ m_{z,x} & m_{z,y} & m_{z,z} \end{bmatrix} = \begin{bmatrix} M_{x,x}+\jmath N_{x,x} & M_{x,y}+\jmath N_{x,y} & M_{x,z}+\jmath N_{x,z} \\ M_{y,x}+\jmath N_{y,x} & M_{y,y}+\jmath N_{y,y} & M_{y,z}+\jmath N_{y,z} \\ M_{z,x}+\jmath N_{z,x} & M_{z,y}+\jmath N_{z,y} & M_{z,z}+\jmath N_{z,z} \end{bmatrix} \quad (1)$$

which provides a point representation of the conductive and magnetic properties of an object. The tensor is symmetric such that $m_{x,y} = m_{y,x}$, $m_{x,z} = m_{z,x}$ and $m_{y,z} = m_{z,y}$ and it is possible to model the system response by

$$\rho(\mathbf{p}) = \mathbf{H}_{\mathrm{t}}^{T}(\mathbf{p})\, \overleftrightarrow{\mathbf{M}}\, \mathbf{H}_{\mathrm{r}}(\mathbf{p}) \quad (2)$$

given that the object centre position vector $\mathbf{p} = [xyz]^T$, the transmitter and receiver coil magnetic field vectors $\mathbf{H}_{\mathrm{t}}$ and $\mathbf{H}_{\mathrm{r}}$, and the object tensor $\overleftrightarrow{\mathbf{M}}$ are known. Consequently, in our WTMD application, $\overleftrightarrow{\mathbf{M}}$ and $\mathbf{p}$ are unknown and need to be estimated based on the system response and the model (2). This leads to an optimization problem to find the tensor $\overleftrightarrow{\mathbf{M}}$ that produces an approximate response ρ, minimizing the function

$$F = \|\rho_{\mathrm{mes}} - \rho\|_2^2 \quad (3)$$

where ρ_{mes} represents the measured system responses. This is solved with the Levenberg–Marquardt algorithm.

The reliability of the inversion, i.e. how well can the model fit the measured signal, can be estimated from the residual value, r. The residual is calculated by taking the L2-norm of the difference between the actual measurements, ρ_{mes}, and the forward response as a function of the inverted tensor and 3D coordinates, ρ, and dividing this value by the L2-norm of the inverted measurements, $\hat{\rho}$; this is defined in (4). The residual value can be also seen as a confidence value for the tensor:

$$r = \frac{\sqrt{\sum_{k=1}^{n} |\rho_k - \rho_{\mathrm{mes}[k]}|^2}}{\sqrt{\sum_{k=1}^{n} |\rho_{\mathrm{mes}[k]}|^2}}. \quad (4)$$

Table 1. The contents of *Library B*. Numbers in brackets represent the total number of measurements per class. The number of scans per object varies, but there is a minimum of five scans per object.

1. Knives (200)	*2. Model guns / bullet cases (180)*	*3. Scissors (30)*
14 Knives	8 Model guns	1 Pair of nail scissors
	2 Sets of phantom bullet cases	1 Pair of office scissors
4. Shoe shanks (90)	*5. Containers (70)*	*6. Belts (25)*
6 Shoe shanks	5 Containers	4 Belts
7. Wristwatches (20)	*8. Keys (20)*	*9. Lighters (20)*
3 Wristwatches	4 Sets of keys	2 Lighters
10. Jewellery (30)	*11. Coins (75)*	*12. Artificial joints (15)*
1 Bracelet 1 Necklace	9 Sets of coins	1 Hip joint
	13. Mobile electronics (60)	
	3 Mobile phones	
	2 MP3 players	

3.3. Test library production

Test data were recorded by repeatedly conducting walk-through scans. One object was carried through the portal at a time, keeping the orientation and position constant. The position was approximately in the centre of the portal horizontally, and at chest height vertically. The orientation was as follows. For a flat rectangular object, the object was kept flat against the chest, in such a way that the longest edge of the object was aligned horizontally. The data recorded for each walk-through consists of the estimated tensor value, $\overleftrightarrow{\mathbf{M}}$, the residual of the inversion algorithm, r, and the estimated coordinates for the path of the object, $\mathbf{P}$.

Since there were several problems to be studied, two test libraries were recorded. The first one, *Library A*, contains knives, metallic containers (different tins), shoe shanks and a model gun with phantom bullet cases. The knives consist of six hunting knives (HK) and four Swiss army knives (SK, Swiss knife). The HKs that we used are Opinel brand, while the Swiss army knives were of various brands. The model gun is a phantom of a Glock 17 [10], with a ferrous steel barrel and slide and polymer handle and magazine. Also, there is a set of phantom bullet cases made of brass. For the model gun with phantom bullet cases, five different objects, i.e. using a varying number of phantom bullet cases inside the model gun, were defined and 20 measurements were conducted per object. For the rest of the objects; ten knives, six containers and six shoe shanks; ten measurements each were conducted. The total size of *Library A* is 320 scans for 27 objects. The contents of *Library A* are shown in table 2.

A broader range of objects was used for *Library B*. It contains *Library A* as a whole, but the additional measurements performed increased the total size to 835 scans for 67 objects. The contents of the library are shown in table 1. Some items are shown in figure 2.

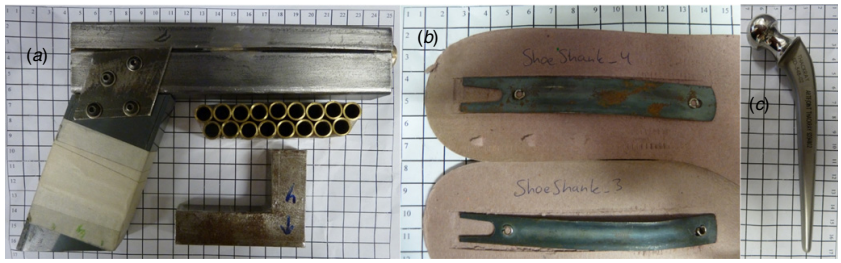

Figure 2. Some objects from Library B. (*a*) NIJ test object, phantom stainless steel gun, and the model gun with some phantom bullet cases. (*b*) Shoe shanks . (*c*) Artificial hip joint.

Table 2. *Library A* contents, excluding the model gun and phantom bullet cases. HK stands for hunting knife, SK for Swiss knife, SS for shoe shank, CS for carbon steel and StS for stainless steel. The dimensions are the blade lengths for the HKs, and *height* × *width* for the shoe shanks as they are thin objects.

Object	Material	Dim (mm)	Object	Material	Dim (mm)
HK1	CS	80	SK1	StS	90 × 26 × 17
HK2	CS	85	SK2	StS	85 × 27 × 19
HK3	CS	90	SK3	StS	90 × 26 × 17
HK4	CS	100	SK4	StS	58 × 19 × 9
HK5	CS	120	Tobacco tin (C1)	Unknown	100 × 76 × 29
HK6	StS	85	Cigarette box (C2)	Unknown	96 × 81 × 15
SS1	Unknown	100 × 23	Lighter box (C3)	Unknown	97 × 46 × 20
SS2	Unknown	110 × 12	Pocket mirror (C4)	Unknown	92 × 60 × 9
SS3	Unknown	110 × 15	Credit card holder (C5)	Unknown	93 × 55 × 6
SS4	Unknown	120 × 12	Zippo (C6)	Unknown	57 × 30 × 10
SS5	Unknown	128 × 14			
SS6	Unknown	135 × 15			

4. Classification algorithm

The method is based on the classification algorithm presented in [3]. For the rest of the paper, this is referred to as the *classifier*, whereas the whole method including tensor inversion is referred to as the *method*. The KNN classifier is a simple algorithm that assumes that the training data are clustered using a certain feature space, that a similarity metric that is derived from the distance between samples, is enough to find the correct class for the sample. The algorithm firstly calculates the features for each data point, i.e. tensor $\overleftrightarrow{\mathbf{M}}$. These are the eigenvalues of the tensor, given by

$$\boldsymbol{\lambda} = [\lambda_1 \lambda_2 \lambda_3]. \tag{5}$$

They are a rotation-invariant representation of $\overleftrightarrow{\mathbf{M}}$. This is shown by the following short proof.

Let $\mathbf{R}$ be any rotation matrix that satisfies the conditions $\mathbf{R}^T = \mathbf{R}^{-1}$, $\det(\mathbf{R}) = 1$ and $\mathbf{R}\mathbf{R}^T = I$, where I is the identity matrix. For any 3-by-3 matrix, a rotated version $\overleftrightarrow{\mathbf{M}}_R$ of $\overleftrightarrow{\mathbf{M}}$ is as follows:

$$\overleftrightarrow{\mathbf{M}}_R = \mathbf{R}\,\overleftrightarrow{\mathbf{M}}\,\mathbf{R}^{-1}. \tag{6}$$

Consider an eigenvalue λ of $\overleftrightarrow{\mathbf{M}}_R$ and the corresponding eigenvector $\mathbf{v}$. By definition, $\overleftrightarrow{\mathbf{M}}_R\,\mathbf{v} = \lambda\mathbf{v}$, given that $\mathbf{v} \neq 0$. Noting that $I\mathbf{v} = \mathbf{v}$, we may write $(\overleftrightarrow{\mathbf{M}}_R - \lambda I)\mathbf{v} = 0$. Evaluation of the characteristic polynomial yields

$$\det(\overleftrightarrow{\mathbf{M}}_R - \lambda I) = \det(\mathbf{R}\,\overleftrightarrow{\mathbf{M}}\,\mathbf{R}^{-1} - \lambda I) = \det(\mathbf{R}\,\overleftrightarrow{\mathbf{M}}\,\mathbf{R}^{-1} - \mathbf{R}\lambda\mathbf{R}^{-1}) = \det(\mathbf{R}(\overleftrightarrow{\mathbf{M}} - \lambda I)\mathbf{R}^{-1}) = \det(\overleftrightarrow{\mathbf{M}} - \lambda I).$$

Therefore, the eigenvalues of $\overleftrightarrow{\mathbf{M}}$ and $\overleftrightarrow{\mathbf{M}}_R$ are the same. Hence, the eigenvalues are rotation invariant.

As $\overleftrightarrow{\mathbf{M}}$ is complex, its eigenvalues form a vector containing three complex values. These three values are then sorted in order of increasing *magnitude*, $||\lambda_k||$. In a 2D complex plane, it is the distance from the origin of the eigenvalue. The magnitude is given by

$$||\lambda_k|| = \sqrt{\lambda_k \cdot \overline{\lambda_k}} \tag{7}$$

where $\overline{\lambda_k}$ is the complex conjugate of λ_k. The eigenvalues are sorted because the distance calculation uses a pairwise comparison between them, and therefore the sorting acts like a guess to minimize the distance to the other objects in the class. The eigenvalues can be seen to exist in a polar coordinate system, and therefore in addition to the magnitude, the *angle* $\phi(\lambda_k)$ of the eigenvalue, as seen from the origin, is given by

$$\phi(\lambda_k) = \varphi = \mathrm{atan2}(\mathrm{Re}(\lambda_k), \mathrm{Im}(\lambda_k)) \tag{8}$$

where atan2 is the arctangent function, and Re and Im are the real and imaginary parts of the eigenvalue, respectively.

Each object is classified by using (9) to compare the Euclidean distance, D_i, between the objects sorted eigenvalues and all of the samples in the library, where the subscript i refers to the library index. The vector of distances is sorted in order of smallest to largest values to produce $\overleftrightarrow{\mathbf{M}}$, and the first K values are selected. The calculation of the Euclidean distance in the case of eigenvalues is shown in figure 3. The classification

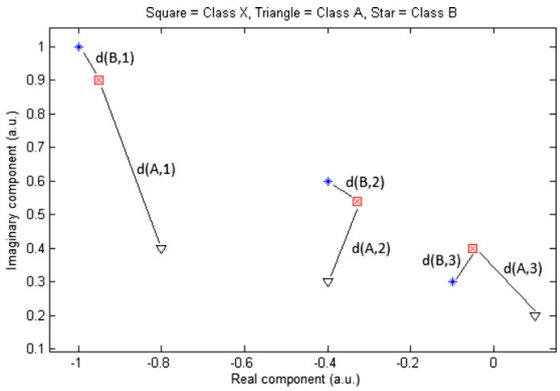

Figure 3. Principle of KNN Euclidean distance calculation based on eigenvalues. The distance here is shorter to class B, and is $D = d(B, 1) + d(B, 2) + d(B, 3)$. The x-axis represents the real component of the eigenvalue, whereas the y-axis represents the imaginary component.

outcome, ζ, is calculated by taking the statistical mode of the class of each of the K nearest distances as shown in (10); often K is an odd number to reduce the chances of even numbers of neighbours belonging to different, most popular classes:

$$D(\vec{\lambda}_a, \vec{\lambda}_b) = \sqrt{(\vec{\lambda}_{a,1} - \vec{\lambda}_{b,1})^2 + (\vec{\lambda}_{a,2} - \vec{\lambda}_{b,2})^2 + (\vec{\lambda}_{a,3} - \vec{\lambda}_{b,3})^2} \quad (9)$$

$$\zeta = Mo(Class\{S_1, \ldots, S_k\}) \quad (10)$$

where Mo is the statistical mode.

5. Test cases and results

We investigate the performance of the algorithm by using four different scenarios. The first one is the most typical case for a WTMD: distinguishing between threatening objects (threat, T) and innocuous, i.e. non-threatening, objects (non-threat, T'). The second case is classifying objects into 13 object classes. The third one studies distinguishing knives from shoe shanks. The final one is a more fine-grained analysis, as we investigate the ability to distinguish a variety of knives from one another. Also, the same is done for shoe shanks and the model gun and phantom bullet cases.

The evaluations are carried out using a *leave one sample out* (LOO) cross validation (CV), and a 4-fold CV over 100 iterations. For the folds, three scenarios are used: 25% of the samples are used as test data and 75% are used as the library (training) data (25/75-CV); 50%–50% (50/50-CV); and 75% test–25% library (75/25-CV). The results quoted are the averages of all iterations.

Accuracy refers to the percentage of the samples that were correctly classified. Recall describes the percentage of the samples of a specific class that were correctly classified. Normalized accuracy (Norm. acc) is used for eliminating the effect of varying sample numbers between the classes. It is defined as the average recall over all the classes.

Table 3. Results for TC1 and TC2. T recall (%) indicates what percentage of the threat objects was correctly classified. Class. (%) is the overall accuracy that indicates what percentage of all samples was correctly classified into 13 classes. Norm. (%) is the normalized accuracy that indicates the average recall over all 13 classes.

Library	K	CV	T versus T' (%)	T recall (%)	Class. (%)	Norm. (%)
B	1	LOO	97.6	97.9	94.7	91.1
B	1	25/75-CV	97.5	97.8	94.5	90.8
B	1	50/50-CV	97.0	97.2	93.3	89.3
B	1	75/25-CV	95.4	95.8	90.1	85.0
B	3	LOO	97.0	97.3	93.3	89.2
B	5	LOO	96.3	95.3	91.1	86.6
B, $r < 0.35$	1	LOO	99.8	99.5	99.1	94.6
B, $r < 0.50$	1	LOO	98.6	99.1	97.1	94.2

5.1. Test case 1 (TC1): threats versus innocuous objects

For the usefulness of the algorithm, its capability of separating threats and non-threats is crucial. Generally, threats are weapons and other dangerous objects. These are sharp items such as knives and scissors; and guns, their parts and bullet cases. Moreover, we consider metallic containers threats because they can conceal the aforementioned objects from the scanner, as the magnetic field does not enter them. Hence, if one were to put a knife in a metallic box, the knife may not be seen by a scanner. It should be noted that this threat definition differs from earlier studies [3], and therefore, comparing the results is not straightforward.

We have divided Library B into threats and non-threats by tagging guns and parts, knives, scissors and containers as threats. All remaining items are tagged non-threats. Hence, the library for this test case is as follows: 480 threats and 355 non-threats. For further testing, we have created additional libraries by removing all samples from the library that have a residual r greater than a threshold value. We call these libraries *B, r < Threshold*, where *Threshold* is replaced by the actual value.

The NIJ [11] defines general requirements for WTMD performance [12]. False negatives, i.e. classifying an object as a non-threat when it is really a threat, are not acceptable in the application area. Therefore, in official tests, any commercial WTMD must recognize all introduced threat objects correctly while maintaining a low false alarm rate. According to the NIJ, the false positive rate can be up to 25%. This means that one out of four non-threats can be classified as a threat. The false positives are not considered to be dangerous; however they cause unnecessary time delays as there is a subsequent need for manual inspection.

The results for TC1 are shown in table 3. The threat recall scores (T recall (%)) mean that one object of class T in 20 to 200 would be falsely classified as T'. Furthermore, the high overall accuracies (Class. (%)) gained indicate a much lower false alarm rate than required by NIJ.

5.2. Test case 2 (TC2): object classification

We have divided Library B into 13 classes of objects, as shown in table 1. As in 5.1, additional libraries called *B, r < Threshold*

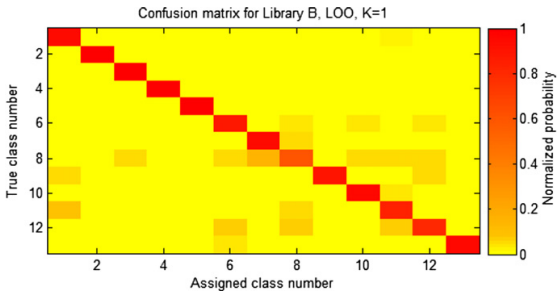

Figure 4. Normalized confusion matrix for *Library B, K=1, LOO*. Each row represents an object class. The colours show to which object classes the classifier has assigned the samples. Correctly classified samples are on the diagonal.

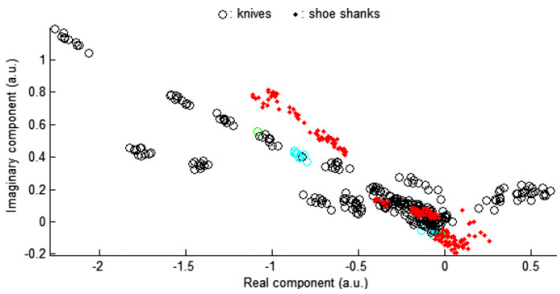

Figure 5. Eigenvalues for knives and shoe shanks. The circles represent knives, while the dots are shoe shanks. The light shaded circles are the ten knife samples that were misclassified in the *leave one object out* case.

are also used. The classifier was run with the same test setups as in TC1.

The results for all tests are shown in table 3. The normalized confusion matrix for the case *Library B, K = 1, LOO* is shown in figure 4. It should be noted that object classes *Keys* and *Artificial Joints* have ceased to exist in library *B, r < 0.35*, since these classes yield high residual scores. Therefore, the result is for 11 classes instead of 13. The lowest overall accuracy was 85%. On the other hand, the best accuracy of around 99% demonstrates great potential.

5.3. Test case 3 (TC3): knives versus shoe shanks

Shoe shanks present a difficult problem for WTMDs, since they have a similar shape and material as some knives. Furthermore, many people do not realize that their shoes could contain metal and therefore will trigger the WTMD to alarm. In addition, taking one's shoes off and putting them back on is considered to be a time consuming and a frustrating operation. Some airports, though, enforce this in order to reduce false alarms.

To study this problem, we set up a library of six shoe shanks and ten knives, ten measurements per object. Hence, the library contains only two classes. Figure 5 shows the eigenvalues for the used test data. It can be seen that the angles of the eigenvalues differ between the two object groups.

Table 4. Results for TC3.

K	CV	Accuracy (%)	Knife recall (%)
1	LOO	100	100
1	25/75-CV	100	100
1	50/50-CV	100	100
1	75/25-CV	99.5	99.3
1	Leave one object out	93.8	90.0

Table 5. Results for TC4.

K	CV	Knives (%)	Shoe shanks (%)	Containers (%)	Model gun/bullet cases (%)
1	LOO	99.0	93.0	100	98.0
1	25/75-CV	99.0	92.8	99.1	96.9
1	50/50-CV	99.0	91.3	98.1	95.2
1	75/25-CV	99.0	88.0	94.2	91.7

The classification algorithm was run with the same CVs as in the previous experiments, but a *leave one object out* CV was added. This means that there were no samples of the object to be recognized in the KNN library, and therefore the problem is much harder for the classifier. This gives us an idea whether the classifier can make generalizations of the two classes by using a limited number of objects in the library. The results are shown in table 4. The results demonstrate that the classifier can distinguish between knives and shoe shanks with an accuracy greater than 93% in all cases.

5.4. Test case 4 (TC4): resolution studies

In order to get an idea of the resolution of the method, we have classified different groups of similar objects in Library A: knives, shoe shanks, metallic containers and the model gun with phantom bullet cases. The classification results of the test cases are shown in table 5.

5.4.1. Knife distinction. There are ten different knives in Library A, and they differ by size, shape and material. Many of the knives are very similar, typical difference in length being 1 cm between nearest examples. The HKs have a thin metallic blade and a wooden handle, supported by a metallic ring. The Swiss knives are thick pieces of metal containing many small blades and tools, in addition to a larger blade that is approximately the length of the knife as a whole. The details for the knives are shown in table 2.

The eigenvalues for the six different HKs are shown in figure 6. The knives HK1–HK5 are made of the same carbon steel material. This can be clearly seen from the fact that their largest eigenvalues seem to have the same angle. The magnitude of the sample cluster centre gives an indication of the length of the blade of the particular knife. However, the stainless steel knife, HK6, has a distinct angle. The blade of the knife is of the same length as the HK2, but the magnitudes of the two knife cluster centres differ significantly. This suggests that only when sample clusters have the same angle can assumptions of the object size be made.

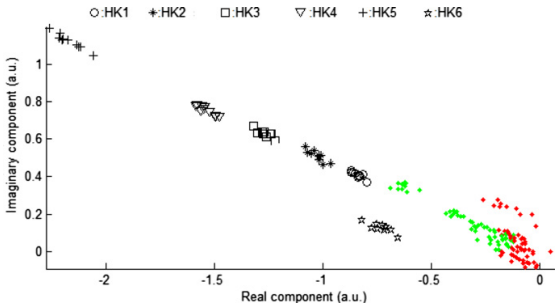

Figure 6. Eigenvalues of hunting knives. The dots represent the middle and smallest eigenvalues, and the different symbols the largest ones.

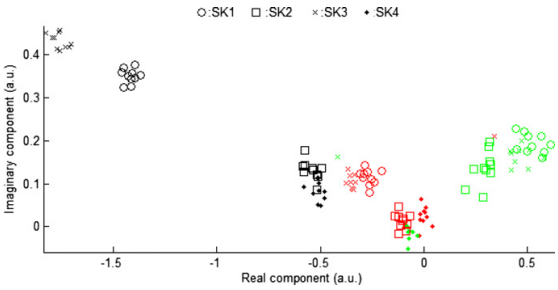

Figure 7. Eigenvalues for the Swiss army knives.

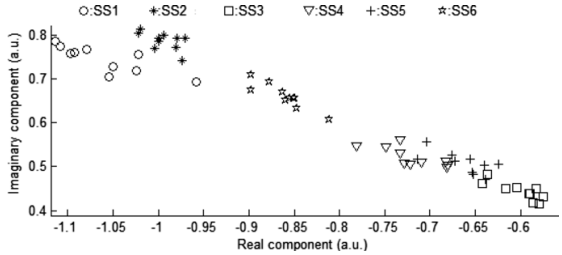

Figure 8. Largest eigenvalues for the shoe shanks. The middle and smallest eigenvalues are clustered together near the origin since the objects are thin and narrow strips of metal.

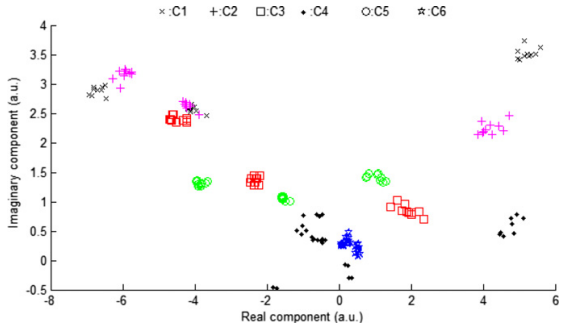

Figure 9. Eigenvalues for the containers.

Figure 7 shows the eigenvalues of the Swiss knives. It can be seen that the eigenvalues follow the same trend as the ones for the HKs, but that the magnitude of the middle eigenvalue component cluster centre is different. This is due to the thickness of the knives. Clearly, SK3 is the largest and SK4 the smallest one. The proportions are somewhat related to those seen in table 2. These observations suggest that assumptions on object material and dimensions might be made based on the eigenvalues.

All test cases for the knife distinction yielded an excellent 99% accuracy, as shown in table 5.

5.4.2. Shoe shank distinction. Shoe shanks are seemingly made of more or less the same material, and their dimensions and shape tend to be similar. The dimensions of the shoe shanks in Library A are shown in table 2, and their largest eigenvalue components are shown in figure 8; the two other components are small and clustered together. It can be seen that although some of the clusters overlap, they seem mostly separable. The classification accuracy was an acceptable 88%–93%. The results for this test are shown in table 5.

5.4.3. Container distinction. As can be seen from figure 9, the eigenvalues give information on the material and the physical dimensions of the objects. This is in line with the observations of the other tests presented in this section.

The tobacco tin (C1) is the largest object in size and consequently the magnitudes of its eigenvalues are the largest of the group. They form three clusters, the centres of which have large magnitudes. The cigarette tin (C2), on the other hand, is slightly smaller in two dimensions and significantly smaller in the other and that is mirrored in the eigenvalues. There are two clusters of the two objects that are close to each other and one cluster each that are separated. It is possible to see that the objects are made of a similar material, because the angles of the cluster centres are similar for both objects.

The rectangular markers representing the credit card holder (C5) suggest similar results. The cluster centres have the same angles as the aforementioned objects, suggesting a similar metal being used to construct it. However, in this case, one cluster is close to the clusters of the other two objects, while the other two clusters are much closer to the origin. This indicates that one dimension of the objects is close to the two other objects, and the two other dimensions are significantly smaller.

The zippo (C6), shown with pentagram markers, is the smallest object of the group, since all the eigenvalues are grouped near the origin, i.e. have small magnitude. The pocket mirror (C4) and the lighter box (C3) eigenvalues cluster centres have different angles, compared to the rest of the objects. Moreover, despite having one dimension approximately as large as the largest object, the cluster centre magnitudes are all significantly smaller than the ones of C1 and C2. This suggests that the magnitude is only comparable along the same angle when comparing object dimensions.

The results for the LOO CV yields 100% accuracy of classifying the containers. Despite the physical similarity of

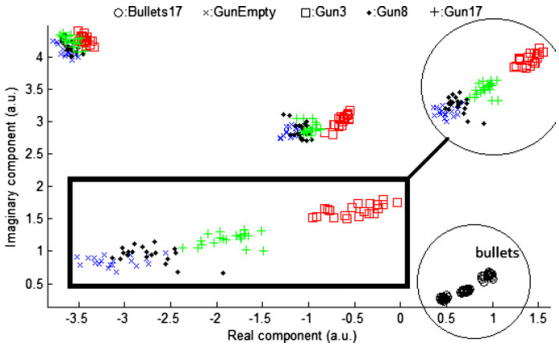

Figure 10. Eigenvalues for the model gun and phantom bullet cases. A set of clusters is zoomed in to show the similarity in shape between the phantom bullet case eigenvalue clusters and the others. The bullet signal appears to be summed on the phantom gun-signal

the objects, this is hardly a surprise, given the clear separability between the eigenvalue clusters shown in figure 9.

5.4.4. Distinction of model gun with phantom bullet cases. For testing the algorithms' capability of distinguishing small differences in objects, we use the steel model gun with a plastic handle. The model gun body (barrel) should yield a certain strong signal, whereas the phantom bullet cases should look distinct in the feature space. We try to see whether the number of phantom bullet cases within the handle can be derived from the eigenvalues only. The test cases that we consider are: empty (no phantom bullet cases), 3, 8 and full 17 phantom bullet cases. For each of these cases, 20 measurements are taken in one location.

The eigenvalues for the model gun and phantom bullet cases are shown in figure 10. Clearly, the electromagnetic properties of the phantom bullet cases (shown with ○ markers) differ significantly from the other cases. The largest eigenvalues of the model gun cases seem to be clustered around the same value. This is due to the large tensor component caused by the steel barrel of the model gun. However, the three phantom bullet cases situation is already some distance from the others in terms of the middle eigenvalue, and even further away in terms of the smallest eigenvalue. The other model gun cases are separated only in terms of the smallest eigenvalue. This suggests that the separation of the three phantom bullet cases is due to a positioning issue of the phantom bullet cases, rather than the amount of phantom bullet case metal in the object. In the latter case, the samples for the empty model gun and the three phantom bullet cases situation should be closer to one another.

The results shown in table 5 indicate that the cases can be classified with over 91% accuracy. This is encouraging for the KNN algorithm, as the separability of the cases is not clear based on figure 10.

6. Discussion

The results of TC1 suggest that threats and non-threats can be effectively distinguished by the method. However, the recall scores were inadequate for a real life application since they are not considered to be sufficiently accurate. Only when high residual values were removed from the library, and therefore some problematic items disappeared from the library altogether, were they close to 100% and therefore could pass commercial testing. This, however, suggests that the method is capable of reaching this level of accuracy if the underlying hardware can yield consistent, accurate data. Different CVs demonstrate that having only a few measured samples of the object in the library signifies a drop in accuracy. Increasing the value of K has a negative effect on accuracy scores.

TC2 shows that the method can distinguish between 13 classes at a very good accuracy, with the normalized values varying between 85% and 91%. This is not much lower than the scores in TC1, where there were only two classes. The results behave similarly to TC1 as a function of library size, the value of parameter K and the quality of the tensors used. The confusion matrix shows that some classes are more difficult to recognize than others; these include belts, keys and coins.

TC3 and TC4 suggest that it is possible to distinguish between intuitively similar objects. For all of the test scenarios, very high accuracy scores were recorded. Furthermore, the figures of the eigenvalues show clearly that the classes are indeed separable by a simple classifier. Moreover, especially the hunting knife comparison has suggested that object material and size can be yielded from the eigenvalues, suggesting there is more work needed on the separability of different materials, shapes and sizes of metallic objects.

This material and size information could be used for enhancing the classifier performance by using heuristics. Furthermore, there are more possibilities for doing this. For example, positional information derived from the inversion algorithm could be used for distinction between shoe shanks and other objects. Shoes are always near the floor level. Therefore, objects at chest level should not be classified as shoe shanks. Similarly, if an object was to be classified as a wristwatch then statistically it is very unlikely that it would be around the feet. On the other hand, knives could be hidden in boots or socks, and therefore making any assumptions like this should be done with great consideration. We have left this for future research.

The most obvious limitation of the KNN, the need for a large set of examples in the library, has so far prevented us from getting a realistic estimate on the true performance of a WTMD that uses our method. The worst case scenario for the classifier, and a realistic one, is that the actual test object to be classified is not in the training library. There are two ways of overcoming such a situation. The first one is to have a classifier capable of forming a generalization of the classes that could fit unseen objects reliably into them. The *leave one object out* CV that we performed in TC3 suggested that the classifier can cope with the scenario. The second, and probably easier way, is to attach a certain level of trust into the classifications. Thus, in cases of uncertainty, a manual inspection could be conducted to determine the cause of the alarm. Moreover,

this could allow the new previously unknown object to be added to the underlying library, hence enabling online learning.

7. Conclusions and future work

The results shown in this paper demonstrate that the algorithm is capable of classifying targets consistently and with a typical normalized accuracy of over 95%, and a recall value in excess of 99%. This is considered to be sufficient to suggest that this improvement shows great promise in the field of inductive metal detection. The tests have shown that similar objects of slightly different sizes can be distinguished with accuracies typically in the range of 85%–100%.

However, there are a number of improvements that could be made to this algorithm and there is further research which can be conducted which the authors expect would improve the results shown here. The observations made on the eigenvalues of the hunting knives, along with similar results in TC4, suggest that information on object sizes and materials might be derived from these data. This indicates that some further heuristics could be applied to the classification algorithm. We aim to study the separability of different materials, shapes and sizes of objects to get an understanding on the limitations of these heuristics. Also, a much broader library is needed for testing the algorithm's capability to make a generalization of the classes. This library should contain samples of different object locations and orientations to enable testing of heuristics that are based on location information given by the inversion algorithm.

Acknowledgments

This work was supported by the Academy of Finland under the project Magnetic Induction and Data Analyses for Sophisticated Sensing, grant no 251777.

References

[1] Rapiscan 2013 Rapiscan metor 6s product specification http://www.rapiscan.com
[2] Bodington T 2011 Is the perceived threat of terrorism greater than the actual threat? http://tsvc.lincoln.ac.uk/papers/submission.php?paper=118
[3] Kauppila J, Ala-Kleemola T, Vihonen J, Jylhä J, Ruotsalainen M, Järvi A and Visa A 2009 Classification of items in a walk-through metal detector using time series of eigenvalues of the polarizability tensor. *Proc. SPIE* **7303** 73030P
[4] Marsh L A, Ktistis C, Järvi A, Armitage D W and Peyton A J 2013 Three-dimensional object location and inversion of the magnetic polarizability tensor at a single frequency using a walk-through metal detector *Meas. Sci. Technol.* **24** 045102
[5] Duda R O, Hart P E and Stork D G 2000 *Pattern Classification* 2nd edn (New York: Wiley-Interscience)
[6] Fails E B, Torrione P A, Scott W R Jr and Collins L M 2007 Performance of a four parameter model for modeling landmine signatures in frequency domain wideband electromagnetic induction detection systems *Proc. SPIE* **6553** 65530D
[7] Tantum S L, Colwell K A, Scott W R, Torrione P A, Collins L M and Morton K D 2013 Sparse model inversion and processing of spatial frequency-domain electromagnetic induction sensor array data for improved landmine discrimination *Proc. SPIE* **8709** 87091E
[8] Bell T H, Barrow B J and Miller J T 2001 Subsurface discrimination using electromagnetic induction sensors *IEEE Trans. Geosci. Remote Sens.* **39** 1286–93
[9] Norton S J, Won I J and Cespedes E R 2001 Ordnance/clutter discrimination based on target eigenvalue analysis *Subsurface Sens. Technol. Appl.* **2** 285–98
[10] Glock 2013 Glock 17 product specification http://us.glock.com/products/model/g17
[11] The national institute of justice 2013 http://nij.gov/
[12] The national institute of justice (nij) 2013 The national institute of justice (nij)-standard 0601.02: Walk-through metal detectors for use in concealed weapon and contraband detection https://ncjrs.gov/pdffiles1/nij/193510.pdf

Publication III

Marsh L. A., Makkonen J., Vihonen, J., Visa, A., Järvi, A., Armitage, D. W., Peyton, A. J. "Investigation of the significance of the 'body effect' on sensitivity to metallic objects in a walk-through metal detector", *Journal of Physics: Conference Series, 450(1):012037, IOP Sensors & their Applications, Dubrovnik, Croatia, 2013.*
dx.doi.org/10.1088/1742-6596/450/1/012037

Investigation of the significance of the 'body effect' on sensitivity to metallic objects in a walk-through metal detector

L A Marsh[1,4], J Makkonen[2], J Vihonen[2], A Visa[2], A Järvi[3], D W Armitage[1] and A J Peyton[1]

[1]School of Electrical and Electronic Engineering, The University of Manchester, Manchester, M13 9PL, UK
[2]Tampere University of Technology, Department of Signal Processing, Korkeakoulunkatu 10, P.O. Box 553, FIN-33110, Tampere, Finland
[3]Rapiscan Systems Oy, Klovinpellontie 3, Torni 2, FIN-02180 Espoo, Finland

E-mail: liam.marsh@manchester.ac.uk

Abstract. An investigation has been carried out to determine the extent to which a walk-through metal detection system is affected by the capacitive and inductive coupling between candidates' bodies and the coil array – known as the 'body effect'. In this experiment both small and large items are investigated to determine ratio of the signal contribution from the candidate compared to the object, and a comparison is made between the response of a small object both with and without the candidate. Also an experiment is presented to demonstrate the inductive / capacitive nature of this signal.

1. Introduction

Walk-through metal detectors (WTMDs) are widely used for personnel screening in security and checkpoint applications. The sensitivity of these detectors is limited by either interference, electronic noise in the receiver circuitry or by spurious inductive or capacitive coupling associated with the presence of the candidate, often known as the *body effect*. A similar limitation is encountered with other metal detection systems such as the *product effect* with on-line conveyor type metal detectors and the *ground effect* with metal detectors for detection of buried objects. This paper investigates the significance of the body effect signal compared to that of metallic targets. There has been little research into this area despite the potential sensitivity limit it presents. It is expected that by better understanding the body effect it should be possible to overcome this restriction.

In this paper a walkthrough metal detector (WTMD) capable of calculating the magnetic polarisability tensor of metallic objects, $\overleftrightarrow{\mathbf{M}}$, is used as a measurement system. The operation of this system is reported elsewhere [1]. Previous studies [2] have shown that the inductive signal from metallic objects can be related to the magnetic field via the magnetic polarisability tensor, $\overleftrightarrow{\mathbf{M}}$, which is represented as a complex, symmetric 3×3 matrix.

[4] To whom any correspondence should be addressed

System measurements, λ, are related to the magnetic polarisability tensor and the incident magnetic field vectors as shown in equation 1. In this expression the vectors $\vec{\mathbf{H}}_{tx}$ and $\vec{\mathbf{H}}_{rx}$ correspond to the values of H-field for the transmit and receive coils respectively. The system inverts the tensor from the computed magnetic field data and measurements. However, this expression does not contain any terms which take into account the effect of the capacitive signal. Consequently any signals of capacitive nature cause errors in the data fitting in the inversion algorithm. In order to improve the data fit, and consequently to perform more accurate tensor inversion it is necessary to account for the capacitive input to the system prior to performing the inversion.

$$\lambda = \overleftrightarrow{\mathbf{M}}\vec{\mathbf{H}}_{tx} \bullet \vec{\mathbf{H}}_{rx} \tag{1}$$

2. Background

Like all electrically conductive objects the human body can store electric charge and display capacitive propoerties. This behaviour is exploited by devices such as touch-screens, however the build-up of static electricity can cause damage to sensitive electronic components and in some electrostatically sensitive processes the operators must also be earthed via a tethered conductor. Typically the human body has a capacitance in the region of 100 pF [3].

In a similar way as eddy currents flow around metallic targets, they are also able to flow around the human body. This leads to the possibility of a distributed inductive response from the candidate as induced eddy currents circulate through conductive and dielectric body tissues. The electrical conductivity of human muscle is approximately 2.5×10^{-1} Sm^{-1} at 10 kHz [4]. Although this is considerably smaller than that of metallic targets e.g. alumimium at $3.58 \times 10^{7} Sm^{-1}$ [5] it is still measurable. As the human body is considerably larger than the pairs of transmit-receive coils throughout the detector the effect is distributed and consequently does not follow a response similar to the case of small metallic targets. Most biological tissues contain water, which is weakly diamagnetic, having a real magnetic susceptibility, χ, of about -9×10^{-6} [6] at room temperature. As a consequence of this it is known that the magnetic properties of water influence the magnetic properties of biological tissues.

An example of an inductive response from a metal object, in this case a model aluminium gun [7] as defined by the *US National Institute for Justice* (NIJ) is shown in figure 1; the x-axis has been normalised such that the object is defined at being in the centre of the detector at *t=0s*. It is possible to compare this signal with the coil geometry used to acquire it, which is shown in figure 3, note the symmetry of the object response, which results from the symmetrical design of the coil array. The coils shown in figure 3 display the fact that the transmit coil (shown in the solid line) contains a single crossover at the point *x=0m* and the receive coil (shown with a dashed line contains two crossover points at $x=\pm 0.18m$). These three crossover points are shown on figure 1 at the points *t=-0.23, 0* and *0.2s*.

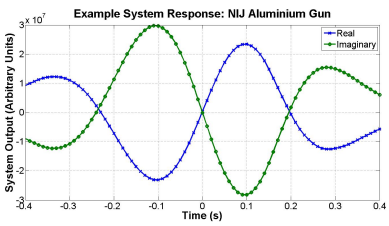

Figure 1. Example inductive signal

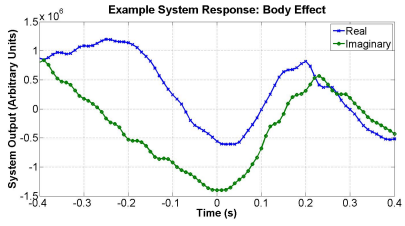

Figure 2. Example body effect signal

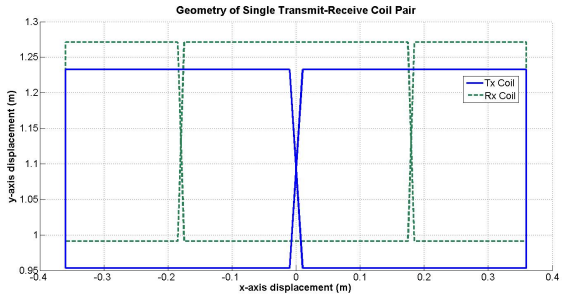

Figure 3. Example tx-rx coil pair

Unlike the high conductivity inductive signal shown in figure 1 a typical body effect signal does not follow a trend. An example of the signal produced by a 'clean scan' – i.e. from the passage of a candidate free from metallic objects is shown in figure 2. The data for this figure was obtained using the same coil pair used for the measurements shown in figure 1. Now however, there is no zero-crossing in the centre of the signal, no symmetry and the real and imaginary components are no longer proportional to each other (i.e. a straight line in the impedance plane), as is the case for the high conductivity inductive measurements.

3. Experimental Setup

Five candidates each made a total of 40 passes through the detector whilst wearing clothing which was free from metallic elements. Ten passes were recorded for when the candidate had no metallic items in their possession, and for the case when they carried steel and aluminium NIJ handguns and an NIJ aluminium knife [7]. On each occasion when the candidate was carrying an item it was placed at the midpoint of the detector with respect to the panel-to-panel displacement, a height of 1.1m with respect to the ground level and all points in the direction of transit through the detector (shown as the x, y and z-axes respectively on figure 4).

In order to determine the nature of the body effect, i.e. if it is predominantly capacitive or inductive, a second investigation has been conducted. This experiment consists of demonstrating the effect that grounding the candidate has on the portal, and the system response to saline of varying conductivity. In the first test a candidate entered the detector and remained inside the portal whilst stretching their right arm outside the sensitive region of the detector. After several seconds the candidate had a grounded wire touched against their right hand for several more seconds; this was then removed. Due to the fact that grounding the candidate is a capacitive action, a change in signal level is expected should the portal be sensitive to the capacitance of the body. The second test involved recording the signal response for a 10 L bucket of saline of varying conductivity from 13.83 mSm^{-1} to 11.18 Sm^{-1}.

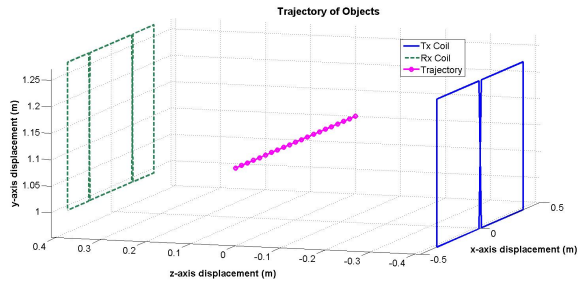

Figure 4. Approximate object trajectory

For each candidate a series of physical measurements were taken to allow for estimation of their body size. In total five parameters were measured – height, the peak width of shoulders, the peak chest size, the waist size and the height of the waist from the ground.

4. Results

The main results from this experiment are shown in figures 5 to 8. In each figure a total of ten walkthrough scans for each of the five candidates is shown. It is possible to see from figures 6 and 8 that the signal from the guns is so strong that it is difficult to see the effect of the body on the measurements. This is reflected in the fact that all of the scans are fully overlaid on one another. Figures 5 and 7 however show that the different candidates give distinguishable responses which are consistent across each of the candidate's walkthroughs. Also inculded in figure 7 are the results for ten scans in the case when the object is not attached to a candidate. To achieve these measurements the object was attached to an insulating pole, and passed through the WTMD.

Although the measurements for the aluminium knife have a far smaller signal than that of the aluminium gun (approximately an order of magnitude difference) it is still possible to see that the two signals share a common phase bias; this is as a result of the response of the aluminium. However, in the case of the knife it is possible to see that this response is superimposed onto that of the body signal to produce the different candidate clusters shown. In the case of the candidate-free scan for the aluminium knife it is possible to see that the response (labelled 'No Candidate'on figure 7) is very linear. This figure clearly shows that the presence of a body along with the object can significantly obscure the target response.

Table 1 shows the Pearson correlation coefficient of the NIJ aluminium gun and aluminium knife for each candidate, averaged across all ten walk-through scans. It also shows the average for the candidate-free scan of the aluminium knife. The aluminium gun measurements show very strong correlation for all candidates with all values in excess of -0.99, thereby verifying that the body signal produced by the candidates has not significantly distorted the response. However, in the case of the aluminium knife the correlation is significantly worse for each candidate, ranging from -0.639 to -0.742. In contrast to these values the coefficient for the 'no candidate' case is in excess of -0.99. These results confirm that the system is capable of measuring a clear, linear response for small targets, however that they are adversely affected by the body effect.

In the case of the clean scans it is also possible to identify clustering of different candidates, however, as would be expected, this is not as obvious as with the aluminium knife. The results show that all five candidates show a distinctly repeatable response when walking through the detector, and with the exception of a single scan for 'candidate 5' the walk-through profiles do not significantly deviate from the main cluster for each candidate.

Table 1. Pearson correllation coefficient for aluminium targets.

Object	Candidate 1	Candidate 2	Candidate 3	Candidate 4	Candidate 5	No Candidate
`Knife`	-0.7420	-0.6329	-0.7017	-0.6536	-0.6388	-0.9994
`Gun`	-0.9974	-0.9989	-0.9967	-0.9996	-0.9993	n/a

Table 2 shows the recorded dimensions of each of the five candidates. The table shows that candidates 3, 4 and 5 are generally larger than candidates 1 and 2. However, the region of interest (1.1 m from the ground) corresponds approximately with waist-level for all candidates; the order of candidates from largest to smallest waist size is $[4; 2; 3; 5; 1]$. Analysis of the data in figure 5 shows that there is no clear correlation between waist size, or between the candidates' physical size and the magnitude or phase of the response. This implies that the relationship between the candidate and the clean scan response is not directly based upon physical size of the body.

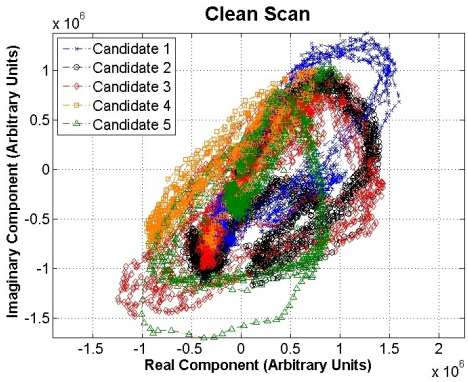

Figure 5. Results of clean scan

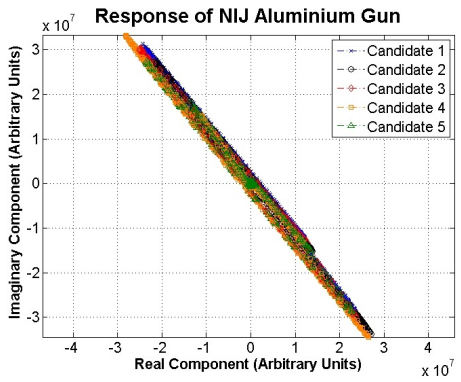

Figure 6. Results for NIJ aluminium gun

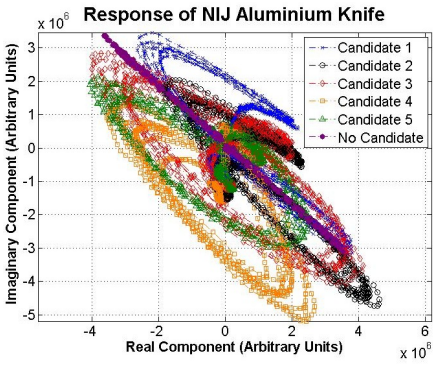

Figure 7. Results for NIJ aluminium knife

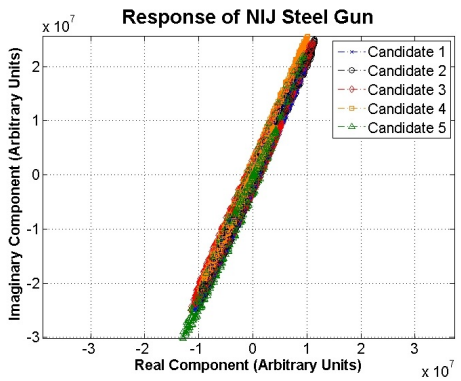

Figure 8. Results for NIJ steel gun

Table 2. Selected dimensions of candidates.

Dimension	Candidate 1	Candidate 2	Candidate 3	Candidate 4	Candidate 5
`Height`	1.79 m	1.74 m	1.87 m	1.86 m	1.85 m
`Shoulders`	1.15 m	1.04 m	1.34 m	1.23 m	1.17 m
`Chest`	0.96 m	0.99 m	1.09 m	1.10 m	1.02 m
`Waist`	0.86 m	1.06 m	1.02 m	1.10 m	0.94 m
`Waist Height`	0.98 m	0.95 m	1.07 m	1.05 m	1.00 m

4.1. Investigation of the Nature of the Body Response

Figure 9 shows the results of the tests for capacitive coupling. In figure 9(a) at sample reference *S=0* the detector is empty. At approximately *S=400* 'candidate 1' stepped into the detector space; the response jumps up at the point and settles down. At *S=750* the candidate was grounded, and remained grounded until *S=2350*. The candidate then remained in the portal until *S=2850*. Each of these phases are clearly visible on the figure. The clear change that occurs when the candidate is grounded demonstrates that the body signal contains a significant capacitive component. In figure 9(b) the response is seen to vary almost entirely in the quadrature component as a function of conductivity. The offset of this linear response is also indicative of capacitive coupling between the coils and the saline.

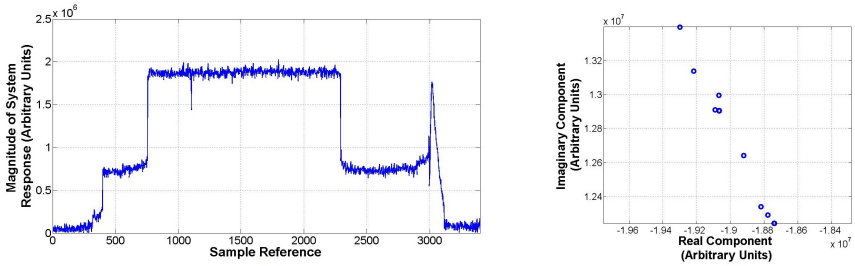

(a) **(b)**

Figure 9. Tests for capacitive coupling between the candidate and the detector

5. Conclusions and Future Work

The results from this paper show that calibration for the body effect is not required for highly detectable objects such as the NIJ handguns; this is due to the fact that the inductive signal dominates in such cases as figures 6 and 8 show. However, there is a visible body signal in the case of both no metallic targets, and for small metallic targets as in figures 5 and 7 respectively. The experiments presented in this paper have demonstrated that a significant proportion of this body signal occurs as a result of capacitive coupling between the candidate and the coil array. The magnitude of this body effect response compared to that of small targets demonstrates a need for either calibration to account for the body signal, or screening to reduce it.

The results of this experiment demonstrate that the body effect appears to be distinct for each candidate. This is reflected in the fact that each of the five candidates produces a clustered response which is shown for all ten scans. This is an encouraging result as it demonstrates that the body effect is both measurable, and repeatable, which are two requirements for the development of a calibration routine.

The next step for this research, having identified the capacitive element of the body effect, is to establish a measurable, theoretical link which can be used to model it. This would then allow for the inclusion of the body effect into the forward model (equation 1) which would subsequently improve the quality of the measured data.

References

[1] Marsh L A, Ktistis K, Järvi A, Armitage D W and Peyton A J 2013 Three-dimensional object location and inversion of the magnetic polarisability tensor at a single frequency using a walk-through metal detector Meas. Sci. Technol. vol. 24 045102 doi:10.1088/0957-0233/24/4/045102

[2] Norton S J and Won I 2001 Identification of buried unexploded ordnance from broadband electromagnetic induction data IEEE Trans. Geosci. Remote Sens. 39 2253-2261

[3] Electrostatic Discharge Association 2010.ESD Part 5: DeviceSensitivity Testing – Human Body Testing, ESD Association, Rome, NY. pp 1.

[4] Gabriel C, Gabriel S and Corthout E 1996 The dielectric properties of biological tissues: I. Literature survey Phys. Med. Biol. vol 41 pp. 2231-2249

[5] Electrical Conductivity and Resistivity for Aluminum and Aluminum Alloys 1999. Retrieved April 22, 2013 from http://www.ndt-ed.org/GeneralResources/MaterialProperties/ET/ET_matlprop_Aluminum.htm

[6] Arrighini G P ,Maestro M and Moccia R 1968 Magnetic Properties of Polyatomic Molecules: Magnetic Susceptibility of H_2O, NH_3, CH_4, H_2O_2. J. Chem. Phys. 49 (2): 882-889. doi:10.1063/1.1670155

[7] Paulter N and Larson D 2009 NIJ Metal Detector Test Object Report (Gaithersburg, MD: National Institute for Justice)

Acknowledgements

The authors would like to thank *Find A Better Way* and the *Academy of Finland* for their financial support of this research under the programmes *SEMIS* and *MIDAS II (grant no. 251777)* respectively. They are also grateful to Michael O'Toole, Omar Abdel Rehim and John Wilson at the University of Manchester for their participation in this experiment.

Publication IV

Makkonen J., Marsh L. A., Vihonen, J., O'Toole, M. D., Armitage, D. W., Järvi, A., Peyton, A. J., Visa, A. "Determination of Material and Geometric Properties of Metallic Objects using the Magnetic Polarisability Tensor", *IEEE Sensors Applications Symposium (SAS), Zadar, Croatia, 13-15 April, 2015.*
dx.doi.org/10.1109/SAS.2015.7133641

Determination of Material and Geometric Properties of Metallic Objects using the Magnetic Polarisability Tensor

Jarmo Makkonen[a*], Liam A Marsh[b], *Member, IEEE*, Juho Vihonen[a], Michael D O'Toole[b], David W Armitage[b], Ari Järvi[c], Anthony J Peyton[b], *Fellow, IEEE*, and Ari Visa[a], *Senior Member, IEEE*

[a]Tampere University of Technology, FIN-33720 Tampere, Finland
[b]School of Electrical and Electronic Engineering, The University of Manchester, M13 9PL, UK
[c]Rapiscan Systems Oy, Klovinpellontie 3, Espoo, Finland
*Email: jarmo.makkonen@tut.fi

***Abstract*—A walk-through metal detector system has been used for measuring the magnetic polarisability tensor for a variety of metallic objects. We propose a method for classifying objects by their metallic composition using features of the tensor. Furthermore, we investigate the potential of using the tensor representation as an indication geometric properties of the object. The method used is shown to be accurate for classification of material composition. Furthermore, the results suggest that it is possible to use the tensor to distinguish between similar objects of different sizes in limited scenarios. These findings demonstrate the potential for this method, but also suggest the need for further studies.**

I. Introduction

In the European Union (EU), scrap metal is currently sorted using a variety of methods. Ferrous materials represent approximately 70% of processed waste, and can be readily extracted by magnetic means [1]; some light metals such as aluminium, magnesium and their alloys are identied by eddy current separation [2], accounting for a further 7.5%. However, there is no automated method that allows for the separation of the remaining 22.5% of materials including copper, zinc, brass, bronze, lead, and stainless steel, in addition to non-metals. It is predicted that the metallic composition of the heavy metals may be identified by their magnetic polarisability tensor, a measure previously demonstrated in electromagnetic metal detection systems.

Metal detector systems are used for a variety of purposes including security screening, detection of buried or visually obscured objects and identifying stray metallic components in food and drug processing lines [3]. The response of these types of inductive metal detectors is known to vary by phase and magnitude due to the presence of samples consisting of different metallurgical properties, e.g. iron, stainless steel and copper. As a consequence of this, it is anticipated that such a system could be used to classify different metallic samples.

Previous studies [4] have shown that the magnetic polarisability tensor can be derived by measurement inversion; this frequency dependent quantity is known to represent the object in terms of geometric aspect ratio, metallurgical composition and orientation. Inverted polarisability tensors have been used for classification of metallic objects in the case of a walk-through metal detector (WTMD) [5], [6]. Also, the tensor representation has been used for discriminating landmines or unexploded ordnance from metallic clutter objects [7]–[9]. The development and application of robust classification algorithms such as the one presented in this paper has the potential to significantly improve the industry sector, facilitating large-scale automation of scrap metal recycling. Such systems could be used to dramatically increase the amount of scrap materials that is successfully recycled.

The ability to coarsely classify objects by their size is also advantageous as it would enable on-line validation of results by means of comparison with an augmented visual shape scanning system. As such metal sorting systems operate at high speed, and using a single-pass of the object, it is essential to be able to determine the reliability of the measurements prior to any sorting.

In this study a walk-through metal detector system has been used [4] to perform a series of measurements of objects. A range of metal types have been considered, including those which can currently be separated, e.g. aluminium and iron, as well as samples which are currently sorted by hand, such as stainless steel and brass. A simple classifier is presented for classifying the objects by material. Also, analysis is performed to identify how differences in geometric proportions, and metallic composition impact the terms of the magnetic polarisability tensor, and hence how they may be used to determine these object properties.

The rest of the paper is organized as follows. Firstly, a description of some of the underlying theory behind the tensor model is provided, along with how it can be used for object classification. This is followed by a description which details the mechanism by which metallurgy affects object response. Results are presented for both material classification and determination of geometric properties of objects. Finally, some further discussion, conclusions and future work is provided.

II. Background

A. Measurement system and data collection method

The WTMD-portal, which operates at a single frequency as described in [4] has been used as the measurement system, and it will be referred to in short as *the portal*. However, the methods described and results provided in this paper are independent of the measurement system. This means that the same principles can be used implemented in more application specific geometries *e.g.* conveyor-based systems.

Measurements were obtained by conducting consistent, natural walk-through scans which were performed by a volunteer carrying a single metallic object. Predefined step markings on the portal floor were used to provide repeatable walking patterns, and a special apron for carrying the test objects on the body was used for maintaining a fixed trajectory for each scan.

B. The polarisability tensor model

The measurement system operates by detecting changes in its background magnetic field, and records these perturbations as the system response ρ. The system then uses this response to estimate the magnetic polarisability tensor of the target object by means of inversion. This inversion is based on a modified Levenberg-Marquardt algorithm, and is described fully in [4]. Target objects are assumed to be linear, and the tensor model defines a point representation of the conductive and magnetic properties of an object as a complex 3-by-3 matrix $\overleftrightarrow{\mathbf{M}}(f)$, given by

$$\overleftrightarrow{\mathbf{M}}(f) = \begin{bmatrix} M'_{x,x}+jM''_{x,x} & M'_{x,y}+jM''_{x,y} & M'_{x,z}+jM''_{x,z} \\ M'_{y,x}+jM''_{y,x} & M'_{y,y}+jM''_{y,y} & M'_{y,z}+jM''_{y,z} \\ M'_{z,x}+jM''_{z,x} & M'_{z,y}+jM''_{z,y} & M'_{z,z}+jM''_{z,z} \end{bmatrix} \quad (1)$$

The tensor is symmetric in such a way that $M_{x,y} = M_{y,x}$, $M_{x,z} = M_{z,x}$, and $M_{y,z} = M_{z,y}$.

The eigenvalues of the tensor $\overleftrightarrow{\mathbf{M}}$ form a vector of three complex values that are ordered ascendingly by their absolute values, given by

$$\boldsymbol{\lambda} = [\lambda_1\ \lambda_2\ \lambda_3] \quad (2)$$

$\boldsymbol{\lambda}$ has been shown to be useful for classifying metallic objects [5], [6]. The magnitude of an eigenvalue is given by

$$r = ||\lambda_k|| = \sqrt{\lambda_k \cdot \overline{\lambda_k}} \quad (3)$$

where $\overline{\lambda_k}$ is the complex conjugate of λ_k. The same order as in $\boldsymbol{\lambda_j}$ applies, and hence $\mathbf{r} = [r_1\ r_2\ r_3]$ where $r_1 \leq r_2 \leq r_3$. For each eigenvalue, r is the distance from the origin in a 2-dimensional complex plane. Similarly, the *phase angle* $\phi(\lambda_k)$ of the eigenvalue in relation to the origin, is given by

$$\phi(\lambda_k) = \varphi_k = \mathrm{atan2}(Re(\lambda_k), Im(\lambda_k)) \quad (4)$$

where *atan2* is the arctangent function, and *Re* and *Im* are the real and imaginary parts of the eigenvalue, respectively. Thus, the angles form the vector $\boldsymbol{\varphi} = [\varphi_1\ \varphi_2\ \varphi_3]$, where the subscript indices refer to the same order as for $\boldsymbol{\lambda}$ and $\boldsymbol{r}$. The angle corresponds to the *phasor response* θ of measurement signal ρ.

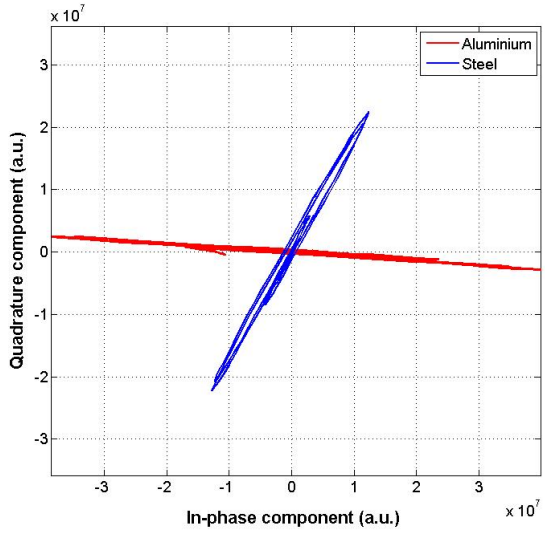

Fig. 1. Variation of object response for identical steel and aluminium samples at 12.5 kHz.

C. Classification of material and geometric properties of metallic objects

Fig. 1 shows an example of the difference in response ρ for aluminium and steel samples of identical dimensions. The figure shows that metallurgy plays a significant role in the response of an object to an inductive measurement system, and that it has the potential for use as a feature for classification. Everyday items such as automotive parts, electrical conductors and construction materials tend to be made from common steels, aluminium alloys, or copper. However, specialist machinery and other bespoke components tend to be made of less common steels and aluminium alloys; therefore a broad range of metallurgies has to be considered. Fig. 1 and underlying theory dictates that the phasor response (θ) is particularly dependent upon object material composition; this angular variation is reflected in the tensor and its eigenvalues $\boldsymbol{\varphi}$. Hence, we want to investigate whether $\boldsymbol{\varphi}$ is a good feature for metal classification.

The difference in the phasor response of objects is dictated by its mechanism of field scattering; for magnetic, non-conducting objects *e.g.* ferrite, the incident field tends to be concentrated through the object, and the phasor response is close to zero degrees. For objects which are highly conductive *e.g.* aluminium and copper, a secondary field is produced as a result of induced eddy currents, producing a variation in the phasor response.

The magnitude of the tensor components varies in accordance with the physical dimensions of the object. Due to skin effect induced eddy currents tend to circulate close to the surface of the object, and hence the relationship is dominated by surface area rather than volume.

TABLE I. THE APPROXIMATE ELECTROMAGNETIC PROPERTIES OF TEST OBJECT MATERIALS.

Metal type	Conductivity (MS/m)	Permeability
Stainless steel	1.41	1.05
Aluminium	20.2	1.00
Fe	4.28	60
Brass	15.66	1.01

TABLE II. THE TEST OBJECT TYPES, MATERIALS AND NUMBER OF SAMPLES. THE THICKNESS OF THE STRIPS IS APPROX. 1.5 MM. THE NUMBER OF SAMPLES FOR EACH OBJECT IS PRESENTED IN PARENTHESIS.

Cylinders	**diameter x height (mm) (number of samples)**
Aluminium	25x25 (10), 30x30 (20), 35x35 (10)
Fe	25x25 (10), 30x30 (10), 35x35 (10) 25x50 (5), 25x75 (5), 25x100 (5)
Stainless steel	25x25 (10), 30x30 (20), 35x35 (10) 25x50 (5), 25x75 (5), 25x100 (5)
Strips	**height x width (mm) (number of samples)**
Aluminium	199x30 (5), 199x25 (5), 200x20 (5) 200x15 (5), 175x20 (5), 175x25 (5)
Fe	200x30 (5), 200x20 (5), 200x25 (5) 200x15 (5), 175x25 (5), 175x20 (5)
Brass	77x20 (10), 113x24 (20)

III. EXPERIMENTS

A. Material classification

Materials are difficult to define specifically due to the fact that most metallic objects are made of alloys instead of pure metals. However, the samples under test consisted of aluminium (*Al*), brass (*Br*), an alloy made of mainly copper and zinc), standard stainless steel (*SS*), a steel typically containing chromium, carbon or manganese in varied quantities, and ferrous steel (*Fe*). The electromagnetic properties of the different materials are shown in Table I. We selected a total of 29 objects shown in Table II for these four classes. Each object is made of a single alloy, and there were two types of objects - cylinders and strips; these are shown in Fig. 3. Out of these objects, 11 were selected for the material classification experiment: the brass strips (2 pcs), and aluminium (3), stainless steel (3) and iron (3) cylinders. The cylinders chosen were spherical, i.e. their diameter and height are equal. The measurements for these objects were recorded around the same operating point within the portal. Their eigenvalues are shown in Fig. 2.

As it can be seen from Fig. 2, each material yields distinct φ_3 values, and that non-magnetic materials (aluminium, brass, stainless steels) are easily separable from ferrous materials. Therefore, phase angle based discrimination is key for material classification.

To test the separation ability of the features (r_3 vs. φ_3), we present a simple multiclass linear discriminant classifier $\zeta(\boldsymbol{x})$. The linear discriminant functions for the classifier are given by

$$g_i(\boldsymbol{x}) = \boldsymbol{w}_i^T \boldsymbol{x} + w_0, \;\; i = 1...4, \tag{5}$$

where $\boldsymbol{x}$ is the feature vector to be classified, $\boldsymbol{w}_i$ a weight vector and w_0 the necessary bias factor, see [10]. Let possible outputs of $\zeta(\boldsymbol{x})$ be ω_1 = brass, ω_2 = stainless steel, ω_3 = aluminium, ω_4 = iron. The output is selected to be ω_i if $g_i(\boldsymbol{x}) > g_j(\boldsymbol{x})$ for all $j \neq i$.

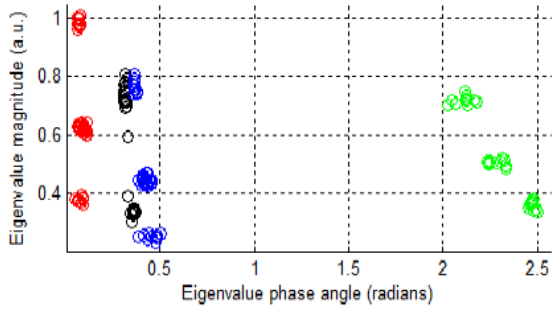

Fig. 2. Eigenvalues (r_3 vs. φ_3) of brass strips (black), aluminium cylinders (red), and AISI/304 stainless steel cylinders (blue), and iron cylinders (green). While the magnitude r_3 as such is clearly insufficient for classification, the phase φ_3 seems to separate the materials fairly well.

TABLE III. RESULTS (CONFUSION MATRIX, %) FOR MATERIAL CLASSIFICATION USING ONE FEATURE. OVERALL NORMALIZED ACCURACY WAS 94.8% (10-FOLD CV) AND 94.9% (2-FOLD CV). NORMALIZED ACCURACY FOR BR/SS-CLASSIFICATION WAS 89.5% (10-FOLD CV), AND 89.9% (2-FOLD CV).

	10-fold CV				2-fold CV			
class	Br	SS	Al	Fe	Br	SS	Al	Fe
Br	96.4	3.6	0	0	95.7	4.3	0	0
SS	17.3	82.7	0	0	15.9	84.1	0	0
Al	0	0	100	0	0	0	100	0
Fe	0	0	0	100	0	0	0	100

TABLE IV. RESULTS (CONFUSION MATRIX, %) FOR MATERIAL CLASSIFICATION USING TWO FEATURES. OVERALL NORMALIZED ACCURACY WAS 99.4% (10-FOLD CV) AND 99.1% (2-FOLD CV). NORMALIZED ACCURACY FOR BR/SS-CLASSIFICATION WAS 98.7% (10-FOLD CV) 98.2% (2-FOLD CV).

	10-fold CV				2-fold CV			
class	Br	SS	Al	Fe	Br	SS	Al	Fe
Br	100	0	0	0	100	0	0	0
SS	2.6	97.4	0	0	3.6	96.4	0	0
Al	0	0	100	0	0	0	100	0
Fe	0	0	0	100	0	0	0	100

We set up the classifier by using MATLAB [11] to train the weights. Two versions of the classifier were created: The first classifier uses only ϕ_3 as a feature, whereas the second classifier uses also r_3. Fig. 4 shows the principle of the classifiers and demonstrates the separability of brass, aluminium, and stainless steel. The decision border H1 uses only ϕ_3, whereas H2 uses also r_3.

For a scientific evaluation, the performance of the classifier was tested with a nested stratified cross-validation (CV). 10-fold and 2-fold cross-validations were used over 100 iterations. The results for the first classifier are shown in Table III, and for the second classifier in Table IV. The results show that the use of two features yields significantly better results in terms of distinguishing between brass and stainless steel.

B. Determination of geometric properties

For the second experiment regarding geometric properties of metallic objects, we selected 27 objects, i.e. all the objects shown in Table II, except the two brass strips. Fig. 5 shows that

Fig. 3. Brass strips, aluminium, iron, and stainless steel cylinders, and iron and aluminium strips.

while a fairly linear correlation exists between the eigenvalue magnitudes and the dimensions of similar objects, it is not feasible to generalize the finding to different types of items. However, this property could be exploited in scenarios where the number of classes is limited and objects have known parameters *e.g.* sorting component sizes on a production line.

The best overall correlation that we found was between the surface area of the object and the length of eigenvalue magnitude vector $\boldsymbol{r}$. As expected, the volume of the items did not seem to correlate with the eigenvalues. The metallic strips might be problematic in this sense as their surface area is large,

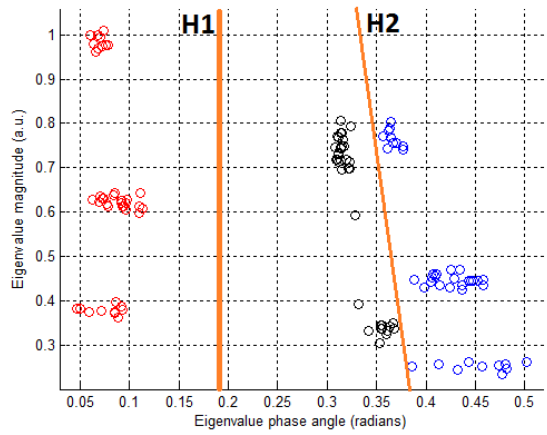

Fig. 4. Brass (black), aluminium (red), and AISI/304 stainless steel (blue) separated by decision borders H1 and H2. H1 utilizes only the phase angle, whereas H2 uses a linear combination of phase angle and magnitude.

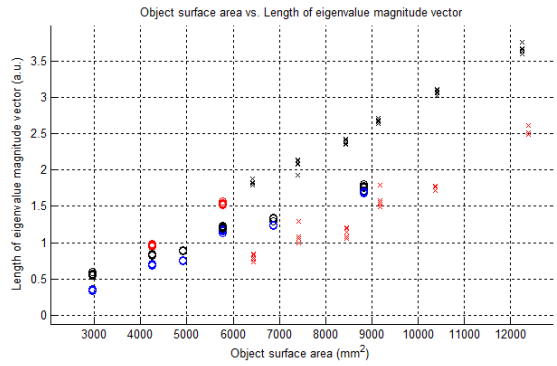

Fig. 5. Length of the eigenvalue magnitude vector of aluminium (red), stainless steel (blue), and magnetic (black) cylinders (o) and strips (x) are plotted against their surface area.

whilst at least one of the dimensions is relatively small.

IV. Discussion and Conclusions

Because the measurement system used for this study is designed mainly for detecting fairly large threat objects (knives, sharps objects, guns, etc.), and each measurement involves a person introducing a body effect in the measured signal, the system is not optimized for material determination. A tailored system is likely to produce a much better signal-to-noise ratio and therefore more reliable results. Although exact composition of metal alloys is unknown, we have shown that a fingerprint for each material type can be identified in the eigenvalues.

A linear discriminant classifier was used for testing the eigenvalue features. However, there are various other classifier types that might be used for the purpose, such as support vector machines, and the choice depends on the application area in question. Here the use of the linear discriminant was motivated

mostly by its simplicity rather than fine-tuned classification performance.

Based on the results, we argue that it is possible to consistently classify objects according to material type. We have also shown that it is possible to use eigenvalues to distinguish between similar objects of different sizes in limited scenarios. The correlation between surface area and eigenvalue magnitude has also been established.

Given the results presented in this paper, the next step for this research is to construct an application-specific measurement system *i.e.* a conveyor-based arrangement to further investigate object properties in a manner in which would be expected for such a system. In addition to this change in detector geometry it would also be advantageous to expand the system, and the algorithm, to perform multi-frequency investigation of targets. It is anticipated that this approach would significantly enhance the process, due to the fact that material response is known to vary significantly as a function of frequency [8], [12].

ACKNOWLEDGMENT

This work was supported jointly by the Academy of Finland under the project *Magnetic Induction Data Analyses for Sophisticated Sensing* - grant no. 251777, and the European Union under the project *Selective recovery of non-ferrous metal automotive shredder by combined electromagnetic tensor spectroscopy and laser-induced plasma spectroscopy* - grant no. 603676.

REFERENCES

[1] F. Passarini, L. Ciacci, A. Santini, I. Vassura, and L. Morselli, "Auto shredder residue lca: implications of asr composition evolution," *Journal of Cleaner Production*, vol. 23, no. 1, pp. 28 – 36, 2012. [Online]. Available: http://www.sciencedirect.com/science/article/pii/S0959652611004148

[2] (2014, Oct.) Eddy current separators — master magnets. http://www.mastermagnets.com/product/eddy-current-separators/.

[3] C. V. Nelson, "Metal detection and classification technologies," *John Hopkins APL Technical Digest*, vol. 25, no. 1, pp. 62–67, 2004. [Online]. Available: http://techdigest.jhuapl.edu/td/td2501/nelson.pdf

[4] L. A. Marsh, C. Ktistis, A. Järvi, D. W. Armitage, and A. J. Peyton, "Three-dimensional object location and inversion of the magnetic polarisability tensor at a single frequency using a walk-through metal detector," *Measurement Science and Technology*, vol. 24, no. 4, p. 045102, Apr. 2013.

[5] J. Makkonen, L. A. Marsh, J. Vihonen, A. Visa, A. Järvi, and A. J. Peyton, "Classification of metallic targets using a single frequency component of the magnetic polarisability tensor," *Journal of Physics: Conference Series*, vol. 450, no. 1, p. 012038, 2013. [Online]. Available: http://stacks.iop.org/1742-6596/450/i=1/a=012038

[6] J. Makkonen, L. A. Marsh, J. Vihonen, A. Järvi, D. W. Armitage, A. Visa, and A. J. Peyton, "Knn classification of metallic targets using the magnetic polarisability tensor," *Measurement Science and Technology*, vol. 25, no. 5, p. 055105, 2014. [Online]. Available: http://stacks.iop.org/0957-0233/25/i=5/a=055105

[7] S. J. Norton, I. Won, and E. R. Cespedes, "Ordnance/clutter discrimination based on target eigenvalue analysis," *Subsurface Sensing Technologies and Applications*, vol. 2, no. 3, pp. 285–298, 2001. [Online]. Available: http://dx.doi.org/10.1023/A%3A1011930422217

[8] S. J. Norton and I. Won, "Identification of buried unexploded ordnance from broadband electromagnetic induction data," *Geoscience and Remote Sensing, IEEE Transactions on*, vol. 39, no. 10, pp. 2253–2261, Oct 2001.

[9] T. H. Bell, B. J. Barrow, and J. T. Miller, "Subsurface discrimination using electromagnetic induction sensors," *IEEE T. Geoscience and Remote Sensing*, vol. 39, no. 6, pp. 1286–1293, 2001.

[10] R. O. Duda, P. E. Hart, and D. G. Stork, *Pattern Classification (2Nd Edition)*. Wiley-Interscience, 2000.

[11] MATLAB, *8.3.0.532 (R2014a)*. Natick, Massachusetts: The MathWorks Inc., 2014.

[12] O. A. Abdel Rehim, J. L. Davidson, L. A. Marsh, M. D. O'Toole, D. W. Armitage, and A. J. Peyton, "Measurement system for determining the magnetic polarizability tensor of small metal targets," in *IEEE Sensors Applications Symposium, Accepted for publication*, 2014.

Publication V

Makkonen J., Marsh L. A., Vihonen, J., Järvi, A., Armitage, D. W., Visa, A., Peyton, A. J. "Improving Reliability for Classification of Metallic Objects using a WTMD Portal", *Measurement Science and Technology, 26(10):105103, 2015.*
http://stacks.iop.org/0957-0233/26/i=10/a=105103

IOP Publishing Measurement Science and Technology
Meas. Sci. Technol. 26 (2015) 105103 (11pp) doi:10.1088/0957-0233/26/10/105103

Improving reliability for classification of metallic objects using a WTMD portal

J Makkonen[1], L A Marsh[2], J Vihonen[1], A Järvi[3], D W Armitage[2], A Visa[1] and A J Peyton[2]

[1] Department of Signal Processing, Tampere University of Technology, Korkeakoulunkatu 10, PO Box 553, FIN-33101 Tampere, Finland
[2] School of Electrical and Electronic Engineering, The University of Manchester, Manchester M13 9PL, UK
[3] Rapiscan Systems Oy, Klovinpellontie 3, Torni 2, FIN-02180 Espoo, Finland

E-mail: jarmo.makkonen@tut.fi

Received 20 April 2015, revised 12 June 2015
Accepted for publication 22 June 2015
Published 26 August 2015

Abstract

In this paper, a walk-through metal detection (WTMD) portal is used for classification of metallic objects. The classification is based on the inversion of the magnetic polarisability tensor (*tensor*) of the object. The nature of bias and noise components in the tensor are examined by using real walk-through data, and consequently, a novel classifier is introduced. Furthermore, a novel method for detecting poorly inverted tensors is presented, enabling self-diagnostics for the WTMD portal. Based on the results, the novel methods increase the accuracy of metal object classification and have the potential to improve the reliability of a WTMD system.

Keywords: WTMD, classification, eigenvalues, electromagnetic polarisability, tensor, bias, noise

(Some figures may appear in colour only in the online journal)

Acronyms

Acronym	Definition
CWD	Concealed weapon detection
EM	Electromagnetic
FEM	Finite element modelling
KNN	K-nearest neighbour
LMA	Levenberg–Marquardt algorithm
LR	Nested binomial logistic regression analysis
NIJ	National Institute of Justice
SNR	Signal-to-noise ratio
UIT	Unreliably inverted tensor
UXO	Unexploded ordnance
WTMD	Walk-through metal detection

1. Introduction

Walk-through metal detection (WTMD) portals are generally used for ensuring that forbidden metallic objects are not taken into security-critical areas. They are used especially at airports and important government buildings. Recently, the fear of terrorism has led to adoption of this security scanning technology in, for example, trains and sports events. This creates a demand for novel technology that would enable fast, unobtrusive scanning of large amounts of people. The current WTMD portal technology often requires the removal of all metallic objects before scanning, which is often considered to be inconvenient. Modern WTMD portals are accurate in detecting metallic objects. However, there have been few attempts further to classify the objects that have triggered an alarm at the portal, for example, as innocuous and threatening objects. Such capability might enable screened people to walk through the WTMD portal with metal, making the scanning process faster and less obtrusive. However, this requires a high accuracy and reliability of classification.

Metallic objects can be efficiently described using a magnetic polarisability tensor model [1, 2]. It has been shown that an inversion algorithm can be used for estimating the tensor model parameters and the trajectory of the object by using measured data from a purpose-built WTMD portal [3]. Our previous work [4, 5] has shown that firstly, a k-nearest

neighbour (KNN) algorithm along with the inverted tensor data from the WTMD portal can be used for object classification at high accuracy (over 85% for classification into 10–13 object types, and 95% for separating threatening objects from innocuous ones) and secondly, that the measured WTMD portal data contains enough information for this type of classification. Also, the results are repeatable and even small differences in object dimensions can be distinguished. Moreover, we have presented a simple method for recognising and discarding poor quality samples and hence improving classification accuracy [4].

However, the test data in [4, 5] were generally recorded by using a single object orientation and by passing the object along the same trajectory through the WTMD portal. Although the classification features of the tensor data should, in theory, be rotation and position invariant, i.e. independent of the orientation of the object and its trajectory, due to practical reasons this is not the case in the WTMD portal used in the aforementioned studies, and thus an element of bias is introduced to the data. In addition, the inversion method is suspect to noise, especially the so-called *body effect* [6]. These facts have not been taken into account by [4, 5] and therefore their results are not generalisable as such.

In this paper, we take the next step towards robust classification of metallic objects by reducing the effect of bias and noise on the reliability of the methods. Firstly, we investigate the properties of the noise and the bias caused by the orientation and position dependency. Secondly, we introduce a novel classification method that can cope with biased and noisy tensor data. Thirdly, we propose a novel method for detecting unreliable tensor data, thus enhancing the reliability of the classification.

The paper is organised as follows. The next section describes the background information for the paper, along with related studies. The third section contains the analysis of noise and bias in the signals, and describes the novel classifier and its performance. Section four presents the novel algorithm for detection of unreliable data. Section five discusses the results and their significance, and finally, section six concludes the paper and gives suggestions for future research.

2. Background and related work

2.1. Related work

Concealed weapon detection (CWD) has been studied widely and a variety of solutions have been proposed [7]. However, metal detectors such as WTMD portals at airports still play a large role in CWD. The portals detect metallic objects, but are generally unable to classify them further into threatening and innocuous items.

The magnetic polarisability tensor representation can be used for characterising the electromagnetic (EM) properties of metallic objects [2]. It describes any metallic object as a 3×3 matrix. Previously, the eigenvalues of the tensor matrix have been proposed as features for classification purposes, including landmine detection [8, 9] and for discriminating unexploded ordnance (UXO) from clutter [8, 10–13].

Kauppila *et al* [1] have proposed the use of tensor eigenvalues for classifying metallic objects in a WTMD portal scenario. Furthermore, we have shown that metallic objects can be accurately classified using a purposely designed portal and eigenvalues of the tensor matrix [4, 5], and that the measurement system is affected by a phenomenon called the body effect [6]. It has also been shown that the technology can accurately distinguish between different types of metal [14].

There is some also other previous research on the subject of metallic object classification using a WTMD portal. An approach based on EM imaging technology has been proposed by Al-Qubaa *et al* [15]. However, the used test set is limited, and although the results are not directly comparable, the reported classification accuracies seem lower than in our studies [4, 5].

2.2. The walk-through metal detector measurement system and data acquisition

This study uses the same WTMD measurement system and setup as [3–5], which will be referred to as *the portal*. However, the methods reported in this paper are not dependent on the portal, and they may be used with any system capable of consistently inverting the magnetic polarisability tensor as described in section 2.3. This system uses 16 coils, eight of which are transmitters operating at different frequencies, ranging from 7 kHz to 14 kHz. The coil geometry is shown in figure 1 [3]. The portal volume is $0.75\ \text{m} \times 2.05\ \text{m} \times 0.83\ \text{m}$, and the design of the portal is largely similar to those in use at airports.

The data for the experiments has been collected by repeated, natural walk-throughs performed by test persons carrying an object. The object has been placed on the body of the person by using a specialised apron with markings. This enables the test objects to be passed through the portal in a repeatable way, along predefined paths. The portal floor is marked with a foot placement grid in order to keep the walk-throughs as similar as possible. The data collection setup is shown in figure 1.

2.3. EM signals, tensor inversion, and basic concepts

A WTMD measurement system, such as the portal described here, is able to detect changes in its excited magnetic field caused by the passage of a metal object. The resultant measurements consist of a series of these changes. When a large enough metallic object is passed through the portal, the detection system is triggered, and the corresponding time series of measurements is recorded as the system response $\hat{\boldsymbol{\rho}}$.

Our aim is to classify the object that has caused the detection system to trigger, and therefore information on the characteristics of the object, i.e. its material, size and shape, are needed. To achieve this, we estimate what kind of an object could have resulted in $\hat{\boldsymbol{\rho}}$ using the magnetic polarisability tensor model. The model defines a point representation of the conductive and magnetic properties of an object as a complex 3×3 matrix $\overleftrightarrow{\mathbf{M}}(f)$, given by

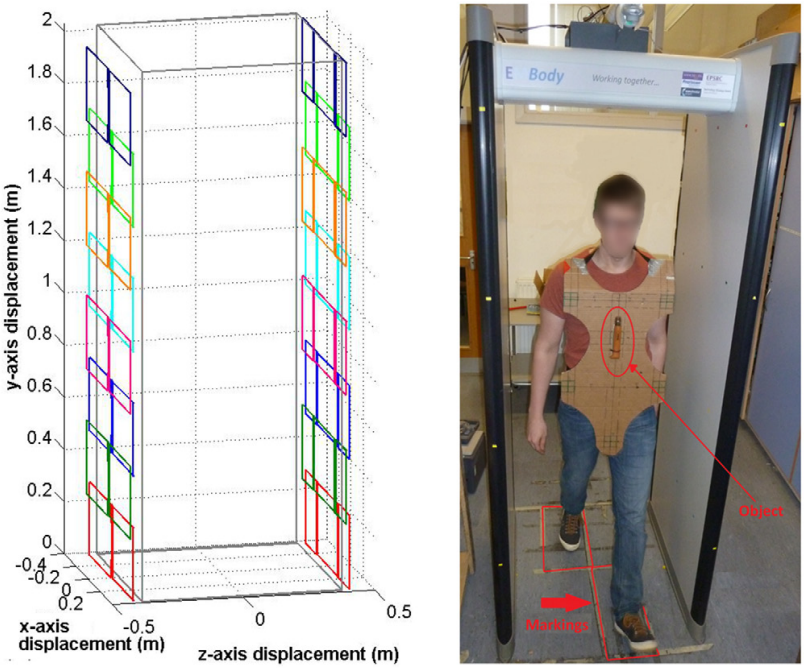

Figure 1. Left: coil geometry of WTMD data acquisition system (reproduced from [3]). Right: the portal hardware and the data acquisition setup. The candidate is wearing an apron with location markings. The target object is marked in the picture, along with the step markings on the floor.

$$\overleftrightarrow{\mathbf{M}}(f) = \begin{bmatrix} m_{x,x} & m_{x,y} & m_{x,z} \\ m_{y,x} & m_{y,y} & m_{y,z} \\ m_{z,x} & m_{z,y} & m_{z,z} \end{bmatrix} = \begin{bmatrix} M_{x,x} + \jmath N_{x,x} & M_{x,y} + \jmath N_{x,y} & M_{x,z} + \jmath N_{x,z} \\ M_{y,x} + \jmath N_{y,x} & M_{y,y} + \jmath N_{y,y} & M_{y,z} + \jmath N_{y,z} \\ M_{z,x} + \jmath N_{z,x} & M_{z,y} + \jmath N_{z,y} & M_{z,z} + \jmath N_{z,z} \end{bmatrix} \tag{1}$$

where f is the excitation frequency of the system. The tensor is symmetric such that $m_{x,y} = m_{y,x}$, $m_{x,z} = m_{z,x}$, and $m_{y,z} = m_{z,y}$ and it is possible to model the system response by the forward response model (*the model*), given by

$$\rho(\mathbf{p}, \overleftrightarrow{\mathbf{M}}) = \mathbf{H}_\mathrm{t}^T(\mathbf{p}) \overleftrightarrow{\mathbf{M}} \mathbf{H}_\mathrm{r}(\mathbf{p}) \tag{2}$$

given that the object centre position vector $\mathbf{p} = [x\ y\ z]^T$, the transmitter and receiver coil magnetic field field vectors $\mathbf{H}_\mathrm{t}$ and $\mathbf{H}_\mathrm{r}$, and the object tensor $\overleftrightarrow{\mathbf{M}}$ are known. Consequently, in our WTMD application, $\overleftrightarrow{\mathbf{M}}$ and $\mathbf{p}$ are unknown and need to be estimated as follows. Based on the model (2) and the measured signal $\hat{\boldsymbol{\rho}}$, it is an inverse optimisation problem to find the tensor estimate $\widehat{\overleftrightarrow{\mathbf{M}}}$ that fits the best to the model, i.e. minimises the difference between the measured response $\hat{\boldsymbol{\rho}}$ and the response ($\boldsymbol{\rho} = \boldsymbol{\rho}(\hat{\mathbf{p}}, \widehat{\overleftrightarrow{\mathbf{M}}})$) calculated with the model. The function to be optimised may be written as

$$F = \|\hat{\boldsymbol{\rho}} - \boldsymbol{\rho}\|_2^2. \tag{3}$$

We call this optimisation process the *inversion*, and it is solved with the Levenberg–Marquardt algorithm (LMA). The solution of the inversion is defined as $\beta = \{\widehat{\overleftrightarrow{\mathbf{M}}}, \hat{\mathbf{P}}\}$, where $\hat{\mathbf{P}}$ is the object path, i.e. a vector consisting of estimated object centre positions $\widehat{\mathbf{p}_i}$.

The eigenvalues $\boldsymbol{\lambda}$ of tensor $\overleftrightarrow{\mathbf{M}}$ are given by an ordered vector (*eigenvalue vector* or *triplet*) of three complex values

$$\boldsymbol{\lambda}(\overleftrightarrow{\mathbf{M}}) = \boldsymbol{\lambda} = [\lambda_1\ \lambda_2\ \lambda_3]. \tag{4}$$

They are a rotation-invariant representation of $\overleftrightarrow{\mathbf{M}}$ (see e.g. [5]), and therefore a useful tool for object classification. The vector $\boldsymbol{\lambda}$ is sorted in order of increasing magnitude of each eigenvalue λ_i, i.e. that λ_1 is the smallest, and λ_3 the largest by magnitude. The magnitude of an eigenvalue λ_k is given by

$$\tau(\lambda_k) = \tau = \|\lambda_k\| = \sqrt{\lambda_k \cdot \overline{\lambda_k}} \tag{5}$$

where $\overline{\lambda_k}$ is the complex conjugate of λ_k. Hence, the sorted vector of magnitudes is $\boldsymbol{\tau} = [\tau_1\ \tau_2\ \tau_3]$ where $\tau_1 \leqslant \tau_2 \leqslant \tau_3$. In a 2D complex plane, τ is the distance from the origin of the eigenvalue.

The eigenvalues can be seen to exist in a polar coordinate system, and therefore in addition to the magnitude, the angle $\varphi(\lambda_k)$ of the eigenvalue, as seen from the origin, is given by

$$\varphi(\lambda_k) = \varphi = \mathrm{atan}(\mathrm{Re}(\lambda_k), \mathrm{Im}(\lambda_k)) \tag{6}$$

where atan is the four-quadrant arctangent function, and Re and Im are the real and imaginary parts of the eigenvalue, respectively. The angle values for the eigenvalue vector $\boldsymbol{\lambda}$ can be then written as $\boldsymbol{\varphi} = [\varphi_1\ \varphi_2\ \varphi_3]$, where the vector is also ordered by increasing magnitude τ.

Eigenvalue vector $\boldsymbol{\lambda}(\widehat{\mathbf{M}})$ and β including the estimated path $\hat{\mathbf{P}}$ are in this referred to as *a sample* for simplicity.

3. Noise and bias in the measured signal

3.1. Definitions of noise and bias

In an ideal scenario, the measured system response would consist of only the signal caused by the target object. However, in reality, a bias and different noise components are present. The overall measured response can be written in a simplistic form

$$\hat{\boldsymbol{\rho}}(\mathbf{p}, \boldsymbol{\Theta}) = \boldsymbol{\rho} + \boldsymbol{\mu}(\mathbf{p}, \boldsymbol{\Theta}) + \mathbf{N}_{\text{body}} + \mathbf{N}, \tag{7}$$

where $\boldsymbol{\Theta}$ is the orientation of the object, $\boldsymbol{\rho}$ the theoretical response for the object, $\boldsymbol{\mu}(\mathbf{p}, \boldsymbol{\Theta})$ a bias term, $\mathbf{N}_{\text{body}}$ the so-called body effect [6], and $\mathbf{N}$ a general noise term.

The theoretical system response term $\boldsymbol{\rho}$ is unknown, but can be estimated for a known object by simulation using finite element modelling (FEM), or approximated by using a solenoid-type measurement system with Helmholz coils.

Introduction of orientation and positional biases to the signal is a typical problem that might arise in any WTMD portal architectures like the one shown in figure 1. The main reason for the orientation bias is that the sensitivity of the system is not equal for all main axes, and therefore rotation causes a modified response. Positional bias is due to the fact that the signal-to-noise ratio (SNR) is dependent on coil geometry and thus not equal within the portal. Also, the model (2) is a point presentation and assumes that the magnetic field is parallel for the whole object. Particularly, if the object is too close to the coils, this is not valid. Furthermore, because the tensor eigenvalues are frequency dependent, the fact that neighbouring transmit coils are excited at distinct frequencies (approximately 500 Hz–1 kHz apart) may introduce some bias. Hence, $\boldsymbol{\mu}(\mathbf{p}, \boldsymbol{\Theta})$ that depends on position $\mathbf{p}$ and orientation $\boldsymbol{\Theta}$ of the object, is introduced.

The body effect $\mathbf{N}_{\text{body}}$ is a noise term that depends on the person walking through the portal, and the electromagnetic properties and size of the object. The body effect is mainly caused by capacitive coupling between the human body and the coils.

The term $\mathbf{N}$ is the overall ambient noise that consists of elements from the noise sources, roughly given by $\mathbf{N} = N_{\text{A}} + \varepsilon_{\text{P}} + N_{\text{IQ}}$ where N_{A} is the amplifier noise, inclusive of voltage, current and thermal noise; ε_{P} parasitic voltages induced into receive coil (due to cross-coupling), and N_{IQ} is the noise from demodulation and filtering.

In theory, at any given frequency, the eigenvalues $\boldsymbol{\lambda}$ of the inverted tensor $\widehat{\mathbf{M}}$ should be invariant in relation to the orientation $\boldsymbol{\Theta}$ of the object and its position $\mathbf{p}$ within the portal. However, LMA fits biased and noisy measurement values to the model (2). Therefore the estimated tensor values will also contain noise and a bias, and moreover, due to the nature of the optimisation algorithm, the effect of these phenomena to the tensor values is non-linear. Based on noisy measurement definition in (7), the tensor eigenvalue vector consisting of inverted noisy eigenvalues can be written as

Table 1. Libraries for bias experiments.

Object	Num. Ors	N/Or	N (OrLib)	Num. Locs	N/Loc	N (LocLib)
HK10	4	40	160			
HK12	4	40	160	12	5	60
Alugun	4	40	160	12	5	60
Steelgun	4	40	160			
OrLib			640			
LocLib						120

Note: LocLib = location experiment library. OrLib = orientation experiment library. N = number of samples. Num.Ors = Number of orientations. Num. Locs = Number of locations. N/Or = Samples per orientation. N/Loc = Samples per location. *HK10* and *HK12* = Hunting Knives, *Opinel* brand, sizes 10 and 12, respectively. NIJ [16] gun phantoms *Alugun* (aluminium) and *Steelgun* (steel) Alugun ja Steelgun = NIJ aluminium and steel model guns, respectively.

$$\boldsymbol{\lambda}(\hat{\mathbf{M}}) = \boldsymbol{\lambda}(\overleftrightarrow{\mathbf{M}}) + \boldsymbol{\mu}_{\lambda} + \mathbf{N}_{\lambda}, \tag{8}$$

where each term denotes the contribution of the corresponding terms in (7). $\mathbf{N}_{\lambda}$ contains the combined noise effect caused by $\mathbf{N}_{\text{body}}$ and $\mathbf{N}$. As we will show in section 3.2, it is convenient to describe the different components in the above simplistic way.

3.2. Data analysis

To study the bias components, two data libraries (see table 1) were collected: library *OrLib* (4 objects, 4 orientations) for the orientation bias, and library *LocLib* (2 objects, 12 locations) for the positional bias. As explained in section 2.2, a special apron was used for marking the locations (location in this context refers to the placement of the object on the body of the candidate, resulting in characteristic paths when walking through the portal) in the upper body of the candidate and carrying the object fixed onto the body. The upper body area was divided into a 4×3 grid, resulting in 12 locations. See figure 2 for details of the locations (figure 2(a)) and orientations (figure 2(b)) used for the data collection.

Figure 3 presents a selection of data in *OrLib* and *LocLib*. From figure 3(a), we observe that for each orientation there exists a distinct cluster, and hence the orientation-dependent bias exists. Furthermore, the size of the clusters, i.e. the variance of the eigenvalues, can be generally seen to be caused by the noise component λ_{N}. Also, because λ_{N} can be assumed to be constant for every orientation, the variation of size between clusters is due to the orientation bias.

Furthermore, analyzing figure 3(b), we see that firstly, the orientation bias can be mostly seen in the magnitude τ and that the effect on τ is significant, up to around 20% for τ_3. Secondly, angle φ of an eigenvalue is not affected to a great extent by the bias if τ for the particular eigenvalue component λ_i is large enough. Therefore, angle φ and magnitude τ represent eigenvalues in a way that might be better suited for classification purposes than the Cartesian version in figure 3(a).

Also, in figure 3(c) a bias component is present as similar markers form small, distinct clusters. It should also be noted that vertical location does not seem to affect the bias component significantly. On the other hand, the poor SNR area of the

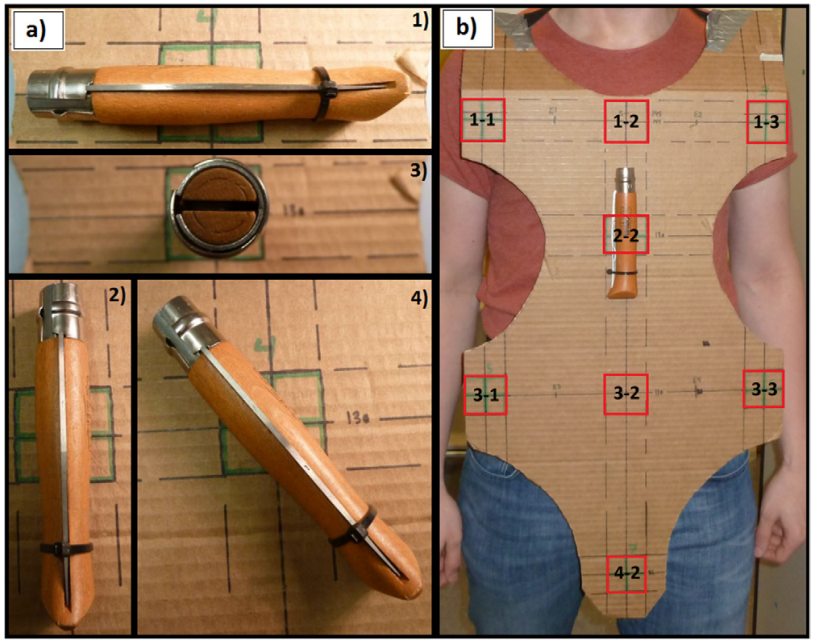

Figure 2. (a) Orientations for library *OrLib* shown on the apron. (b) Locations (marked on the apron) for library *LocLib*. Note that locations 2–1, 2–3, 4–1 and 4–3 are not marked.

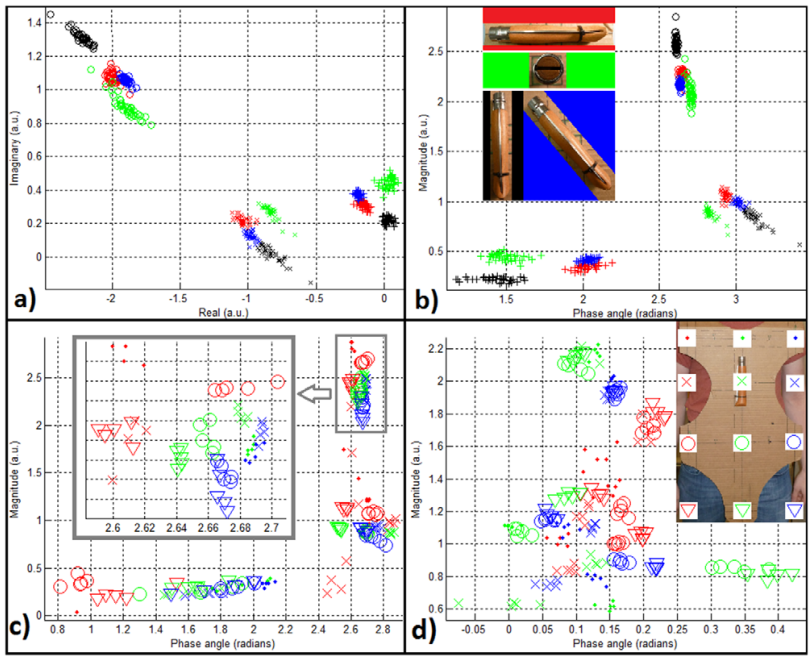

Figure 3. (a) *HK12* eigenvalues (cartesian coordinates) for 4 orientations. See colour coding in (b). (b) *HK12* (polar coordinates, *pc*). Colour coding of orientations applies for all three symbols (that stand for λ_1, λ_2, and λ_3). (c) *HK12* eigenvalues (*pc*) for 12 locations. See legend for horizontal and vertical location markers. See legend of (d). (d) *Alugun* eigenvalues for 12 locations. Legend in upper right hand corner refers to the locations shown in figure 2.

portal (red markers) produces, as expected, more noisy and scattered values compared with the areas shown with green and blue markers. Finally, in figure 3(d), distinct locations yield distinct clusters, and therefore a bias is present, and is mostly a function of horizontal location.

As a conclusion, we argue that significant orientation and positional biases $\boldsymbol{\rho}_{\boldsymbol{\mu}}$ and $\boldsymbol{\lambda}_{\boldsymbol{\mu}}$ exist, and are mainly present in magnitude τ of the eigenvalues. This result means that any classifier must take this dependency into account, and a single sample of an object cannot serve as a prototype for classification.

3.3. Novel classifier for countering noise and bias

In our previous studies [4, 5], we used a modified KNN-algorithm for classifying the samples. The distance D between the sample to be classified, $\hat{x}$, and each sample x_i in the *template library*, the collection of known reference samples, was calculated using a distance measure, given by

$$D(\boldsymbol{\lambda}_a, \boldsymbol{\lambda}_b) = \sqrt{(\lambda_{a,1} - \lambda_{b,1})^2 + (\lambda_{a,2} - \lambda_{b,2})^2 + (\lambda_{a,3} - \lambda_{b,3})^2} \tag{9}$$

where $\boldsymbol{\lambda}_i$ are eigenvalue vectors sorted by magnitude, as stated in section 2.3, and $\lambda_{i,j}$ are the corresponding sorted eigenvalues.

This conventional method assumes that ordering eigenvalues by magnitude τ results in small distance values for samples from the same object/class. However, sometimes the τ-values are similar for two eigenvalues of the same object/class, and noise might change the order of comparison. As we have shown in section 3.2, bias term $\boldsymbol{\mu}_{\lambda}$ and noise term $\mathbf{N}_{\lambda}$ have a significant impact on the variation of magnitude τ-values. Therefore, two samples recorded for the same object might yield large distance values. Figure 4 demonstrates the problem situation and how it affects distance calculation.

As a solution, we introduce a novel classification algorithm. We calculate distance D for all six sample order permutations $\sigma = \{\sigma_1\ \sigma_2\ \sigma_3\ \sigma_4\ \sigma_5\ \sigma_6\}$ of eigenvalue vector $\boldsymbol{\lambda}$, i.e. $\boldsymbol{\lambda}(\sigma_2) = [\lambda_2\ \lambda_1\ \lambda_3]$. The class of sample x_i with the smallest resulting distance is selected as the classification outcome. We can write

$$D_{\sigma}(\boldsymbol{\lambda}_a, \boldsymbol{\lambda}_b) = \min_{j \in \{1\ldots6\}} (D(\boldsymbol{\lambda}_a, \boldsymbol{\lambda}_b(\sigma_j))). \tag{10}$$

Instead of using K samples for deciding the classification outcome, we select the sample with smallest D_{σ}-value, i.e. the nearest neighbour.

We tested the new method by classifying a set of libraries (see table 2) with the previously defined ((9), parameter $K = 1$) and new methods. The results are shown in table 3. Furthermore, the libraries *OrLib* and *LocLib* (see section 3.2) were combined and the resulting library (720 samples) was classified into knives and guns by using Library E as the template library. The results show that the novel classifier increases classification accuracy significantly compared with the previously reported method, reducing misclassifications by 5–46% for libraries D–H. Also, the novel classifier is able to cope with biased tensor values in LocLib and OrLib.

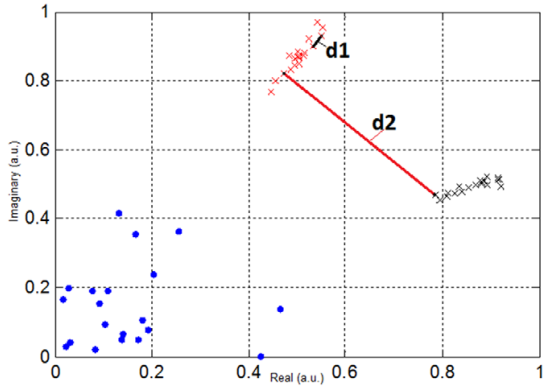

Figure 4. When calculating the distance between two sets of eigenvalues λ, a problematic situation arises when there are two eigenvalue λ clusters that have approximately the same magnitude τ. If the samples are ordered using τ for distance calculation, the algorithm may end up calculating the inter-cluster distance $d2$ instead of the small intra-cluster distance $d1$.

Table 2. Libraries for testing the novel classifier.

Library	Samples	Classes
D (2013)	1316	10 classes [4]
E (2014)	835	13 classes [5]
G	3990	115 objects as separate classes
H	369	40 objects as separate classes

Note: D and E were used in our earlier papers. G is a large library for classifying samples into objects (e.g. HK12) rather than object classes (such as knives). H is similar to G, but smaller in size and the samples are measured using apron location 1–3 (see figure 2) that yields good SNR.

4. Self-diagnostics for improving classification reliability

4.1. Inversion reliability and unreliably inverted tensor detection

The quality of solution β found by the inversion algorithm LMA (as described in section 2.3) is crucial for classification reliability. Especially, if the estimated tensor $\widehat{\mathbf{M}}$ is poor, the sample in consideration is Unreliable from a classification point of view. We call these samples unreliably inverted tensor (UIT), and the rest of the samples *good samples* for brevity. In this section, we introduce a method for self-diagnostics of the WTMD portal. The purpose of the method is to detect any UITs before using them for classification. Hence, the method has the potential to increase the reliability of classification of metallic objects.

The quality of solution β depends, firstly, on the quality of the measurement $\hat{\boldsymbol{\rho}}$, i.e. SNR. If e.g. the body effect dominates the signal $\hat{\boldsymbol{\rho}}$, inverting the tensor for the metallic object becomes impossible. Secondly, the quality of the initial guess solution $\beta_0 = \{\widehat{\mathbf{M}}_0, \hat{\mathbf{P}}_0\}$ made by LMA is crucial. Finally, independent of measurement quality, the solution depends on the validity of the model (2) for the scenario, in particular the shape of the object and the properties of the excited magnetic field.

Table 3. Results for the novel classifier (All %).

Library	T(o)	**T(n)**	I(T)	C(o)	**C(n)**	I(C)	N(o)	**N(n)**
D (2013)	98.9	**99.0**	9.1	97.6	**97.9**	12.5	96.0	**96.4**
E (2014)	97.6	**98.7**	45.8	94.7	**96.5**	34.0	91.1	**93.4**
G	97.2	**97.4**	7.1	86.1	**86.9**	5.8	79.6	**80.2**
H	N/A	**N/A**	—	93.2	**95.1**	27.9	93.0	**94.9**
LocLib + OrLib	N/A	**N/A**	—	99.9	**99.9**	0	99.9	**99.9**

Note: T = Accuracy for distinguishing between threatening and innocuous objects. C = classification accuracy. N = normalised classification accuracy i.e. average precision. o = KNN classifier presented in our earlier papers. n = novel classifier. I = percentage of reduced misclassifications (for C or T).

The quality assessment of sample β should consider both $\widehat{\mathbf{M}}$ and the estimated path $\hat{\mathbf{P}}$. The quality of $\widehat{\mathbf{M}}$ can be intuitively defined by how well it corresponds to the theoretical tensor $\overleftrightarrow{\mathbf{M}}$ for the detected object. This, however, cannot be solved since the detected object and therefore $\overleftrightarrow{\mathbf{M}}$ are unknown. Instead, the reliability of $\widehat{\mathbf{M}}$ has to be determined by secondary, indicative measures. Previously, the *residual* r, a measure for inversion performance, has been proposed as an indicator of the quality of $\widehat{\mathbf{M}}$ [4]. The residual and the definition of the quality of $\widehat{\mathbf{M}}$ will be discussed in section 4.2.

The quality of $\hat{\mathbf{P}}$ has not been addressed previously. On the other hand, it has been shown that $\hat{\mathbf{P}}$ is realistic for good samples [3, 17], i.e. the quality of $\widehat{\mathbf{M}}$ and $\hat{\mathbf{P}}$ go hand in hand. Moreover, assumptions on the possible trajectory of the object can be made based on *a priori* knowledge. Hence, we argue that it is possible to use heuristic principles for determining the quality of $\hat{\mathbf{P}}$.

We propose a novel UIT detection method (path analysis) based on the analysis of $\hat{\mathbf{P}}$ (see section 4.3): we hypothesize that if $\hat{\mathbf{P}}$ is not credible, i.e. it does not reflect the supposed trajectory of the object, then the sample in consideration is likely a UIT. Consequently, we argue that path $\hat{\mathbf{P}}$ contains additional information on the UIT detection problem compared to using solely the residual r, and therefore features derived from $\hat{\mathbf{P}}$ could be used for detecting UITs either on their own, or in conjunction with r.

To test these claims, we will compare the performance of three UIT detection methods, respectively based on residual analysis, the novel path analysis, and a combination the two (combined analysis). Subsequently, section 4.4 describes the experiments and results of comparison between the aforementioned three methods.

4.2. Residual analysis UIT detection method

The residual value, r, is a measure for prediction error within the inversion, i.e. quality of β. In this case, the residual is calculated by taking the L2-norm of the difference between the actual measurements $\hat{\boldsymbol{\rho}}$, and the forward response $\boldsymbol{\rho}$ as a function of the inverted tensor $\widehat{\mathbf{M}}$ and path $\hat{\mathbf{P}}$, and dividing this value by the L2-norm of the measurements $\hat{\boldsymbol{\rho}}$, given by

$$r = \frac{\|\boldsymbol{\rho} - \hat{\boldsymbol{\rho}}\|}{\|\hat{\boldsymbol{\rho}}\|} \tag{11}$$

where $\hat{\boldsymbol{\rho}}$ contains measurement values over time for all transmitter-receiver coil pairs.

The lower the residual, the better the solution found by the inversion represents the measured signal $\hat{\boldsymbol{\rho}}$ when using the model (2). However, it does not represent only the quality of the solution, but the suitability of the model itself for representing the signal. Therefore, it is possible that a poor quality solution yields a low residual value.

The residual analysis-based UIT detection method, as we have described previously in [4], works as follows. Let r_T be a residual threshold between 0 and 1. For any sample, if its residual $r > r_\mathrm{T}$, it is deemed a UIT. However, our data analysis suggests that for each set {object, $\boldsymbol{\Theta}$, $\mathbf{P}$} there exists a typical residual value (usually between 0.1 and 0.5) for the successfully inverted samples, and therefore, choosing r_T is challenging.

4.3. Path analysis UIT detection method

It is known *a priori* that when a person walks through the portal, any metallic object placed on the torso should follow a relatively straight trajectory, any curvature resulting from gait and the slight angle in which the portal is entered. Hence, if e.g. path $\hat{\mathbf{P}}$ is not following a roughly straight line, the sample might be a UIT. Examples of estimated paths for good samples and UITs are shown in figures 5 and 6. Note a special case shown as the black straight line in figure 5. Here, the estimated path $\hat{\mathbf{P}} = \hat{\mathbf{P}}_0$, and the inversion has failed to find a sensible solution.

To model the typical behaviour of the paths for good samples and UITs, a set of heuristic *path features* are calculated using $\hat{\mathbf{P}}$. Example features include the coordinate ranges of $\hat{\mathbf{P}}$ in horizontal and vertical directions. Subsequently, the path analysis-based UIT detection method uses a set of these features to form a classifier based on linear discriminant analysis [18]. The classifier parameters are trained, i.e. optimised, using a recent machine learning technique.

4.4. Experiments and results

A set of annotated data labeled as UITs and good samples is needed for training and testing the UIT detection methods. In order to label samples, we need to define what kind of samples are UITs in this context. The most important issue for reliability, from classification point of view, is repeatability. Normally, for each unique set {object, $\boldsymbol{\Theta}$, $\mathbf{P}$}, the eigenvalues of the tensor estimates form clusters (see e.g., figure 3(a)).

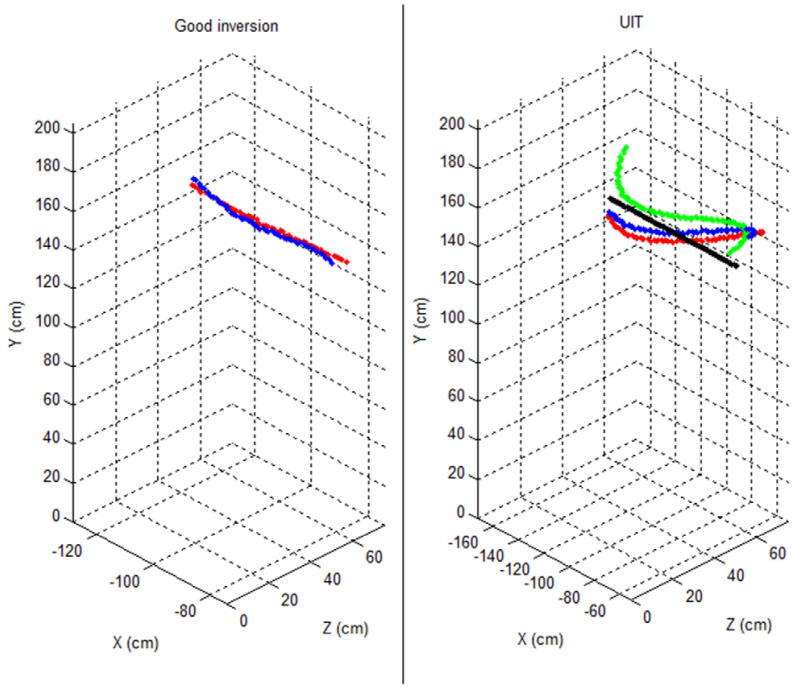

Figure 5. Examples of inverted paths in 3D for good samples (left) and UITs (right). See figure 1 for reference.

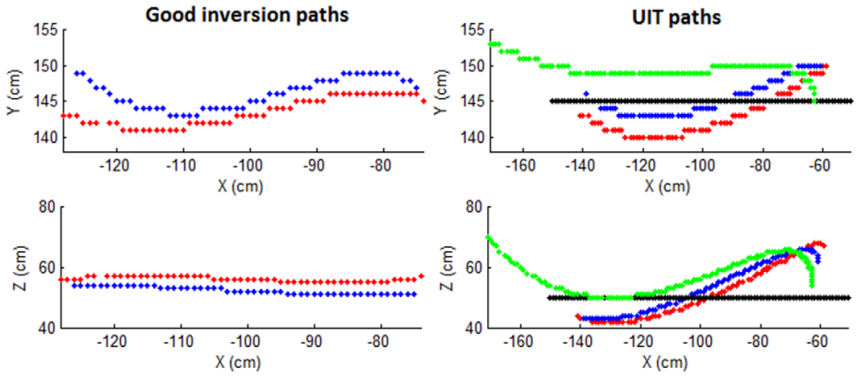

Figure 6. Examples of inverted paths in 2D (XY and XZ planes) for good samples (left) and UITs (right). See figure 1 for reference. The shape of the path in XY-plane results from gait. Our previous experience shows that the path should be roughly linear in XZ-plane (representing horizontal movement). This is not the case for UITs.

If the eigenvalues for a solution differ significantly from these clusters, we say that the sample in consideration is a UIT. This kind of approach is called *outlier detection* [19].

A large amount of samples were inspected visually and any eigenvalue outliers were labeled as UITs. The training data was divided into two differently balanced sets (training libraries) for examining how training data composition affects UIT detection performance: library A (109 samples, of which 59 UITs) and library B (297 samples, of which 22 UITs). The union of libraries A and B is named library C. Library A contains samples from e.g., knives, coins, and jewellery, whereas library B contains samples from 13 object classes.

To train the UIT detection methods, an automated machine learning approach, namely nested binomial logistic regression analysis (LR), was applied. Logistic regression [20] in this context essentially finds a linear discriminant classifier for deciding whether the given sample is a UIT or a good sample. The classifier is formed by the input vector of binary features, their corresponding weights that the logistic regression analysis learns based on given training data, and the discriminating criterion to make the final decision. To implement logistic regression for this study, we used GLMNet for MATLAB [21].

To be able to use LR for training the residual analysis-based UIT detection method, the single feature r was

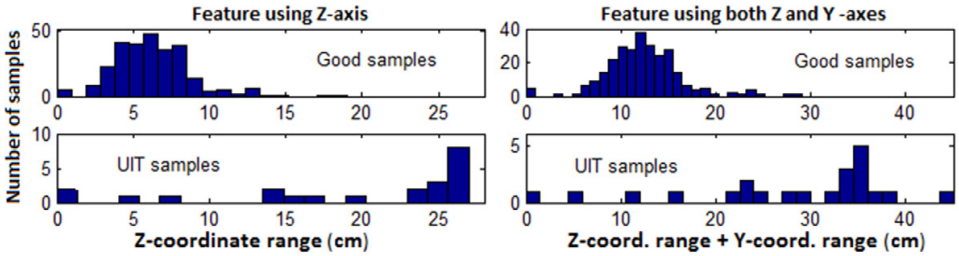

Figure 7. Feature histograms for separating UITs from the good samples. On the left, *Z*-coordinate range means the amount of horizontal movement within the path. Note that UITs tend to have values greater than 10, whereas the good samples get lower values. On the right, *Z*-coord. range + *Y*-coord. range means the sum of the horizontal and vertical ranges for the path. Similarly, the good samples get values below 20, but UITs get higher values.

quantized into 35 binary residual features using 35 values between 0.05 and 0.9 for threshold r_T. Essentially, the classifier learns the best value for r_T. For the path analysis-based UIT detection, we analyzed paths of UITs and good samples in library C. Figure 6 demonstrates the difference between typical good paths and some UIT paths. Based on this knowledge, we selected four suitable path features (see examples in figure 7). To use these features in LR, a set of thresholds were used for quantizing them into 89 binary path features. For each feature, between four and 33 equally distributed thresholds were used. The combined analysis-based method was trained by using both the residual features and the binary path features for LR, resulting in a total of 124 binary input features.

The methods were trained by using all three training libraries, resulting in three versions (differing by parameters) of each method. The performance results for these methods are shown in table 4. A 10-fold nested cross validation of data was used for LR. The results show that regardless of training library, path analysis and combined analysis-based methods are more accurate in predicting UITs than the residual analysis-based method.

The results were validated by using library G (see table 2). Each method detected and removed UITs from the library. The remainder of the library was then classified using the novel classification algorithm described in 3.3. In addition to the aforementioned trained versions of the UIT detection methods, we created a set of new ones for studying the effect of r_T on the residual analysis. Eight new residual analysis UIT detection methods were created by assigning them static values for r_T. Values of r_T were {0.20 0.25 0.30 0.35 0.40 0.50 0.60 0.70}. In addition, three combined analysis UIT detection methods were created by first using residual analysis with a static r_T (0.5, 0.6, and 0.7, respectively) for pre-filtering the library and then the trained path analysis -based method (trained by using library C) for the remainder. The results are shown in figure 8. The results suggest firstly, that the presented novel UIT detection methods are able to reduce the amount of misclassifications significantly, and secondly, that regardless of parameters and used training libraries, it is possible to gain better classification accuracy by using path analysis and combined analysis -based methods compared to using residual-based methods.

Table 4. Results for UIT prediction using logistic regression.

Library	Method	UIT prediction accuracy (%)			Gain over guess		
		A	B	C	A	B	C
	Random guess	54.1	92.6	80.0	1.00	1.00	1.00
	Residual analysis	70.6	94.6	85.7	1.30	1.02	1.07
	Path analysis	85.3	99.0	89.7	1.58	1.07	1.12
	Combined analysis	**88.1**	**99.7**	**92.6**	1.63	1.08	1.16

Note: Random guess means the accuracy score gained with a naive predictor with a static output (the class with the highest a priori probability) for all samples. Gain over guess defines how much better the method is than Random guess.

Using conservative residual thresholds (e.g. 0.6 or 0.7) yields significant improvement on original classification accuracy. Nevertheless, lowering r_T further does not yield significant improvement after $r_T = 0.35$. On the other hand, regardless of their parameters, the markers for the path analysis and combined analysis-based methods are all above the curve formed by residual analysis-based method markers. This further validates our previous observations, suggesting our hypotheses stated in section 4.1 are correct.

5. Discussion

We have shown that significant positional and orientation bias components are present in inverted samples β. Because the magnitude τ of sample eigenvalues is especially affected by the bias components, the use of τ for fine grained analysis, for example estimating object size and shape, might be problematic. On the other hand, the angle φ of sample eigenvalues is robust against the bias. In addition, it has been shown [14] that φ contains information on the material of the object, while τ contains coarse information on the dimensions of the object. Therefore, instead of using Cartesian coordinates, τ and φ should be used for classification purposes, e.g. distance calculation, when possible. The novel classifier presented in this paper used Cartesian coordinates and was shown to cope with

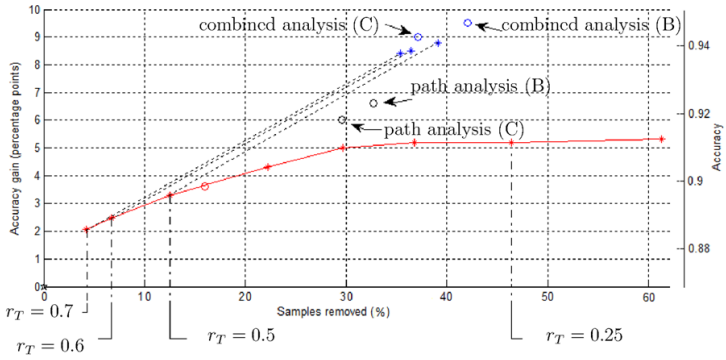

Figure 8. Classification accuracy gain versus percentage of samples remaining in library for each method. Letters B and C in parenthesis denote the used training library. Note that the path-based (black) and combination methods (blue) score consistently above the residual-based filters (red). The black pentagram marker (in the lower left hand corner) shows the result for the unmodified original library. Circular markers (o) represent the trained classifiers. Red asterisk markers (connected by the red line) represent fixed residual threshold methods. Blue asterisk markers represent combinations of a fixed residual threshold and the path-based method trained with Library C.

biased values. However, its principle is independent of the applied distance measure.

The positional bias might be compensated by using samples that are measured using the same approximate location (i.e. portal region) as the template library in the KNN matching process. The region can be estimated using the estimated path $\hat{\mathbf{P}}$ of the object. On the other hand, the orientation of the target object cannot be estimated in the current portal setup. This gives rise to the need for novel, robust distance measures.

The presented UIT detection methods can be used for two main purposes. Firstly, for removal of unreliable samples from classifier training data, or in the case of a KNN classifier, the template library samples x_i. Secondly, self-diagnostics of the inversion could be performed as follows. If a UIT is detected, the inversion process can be re-initiated with a new initial guess. Hence, in theory the only samples to be completely discarded, leading to a potential manual scan, would be the ones with poor SNR. This way it is possible to move the markers in figure 8 towards the left, being able to classify walk-throughs while performing self-diagnostics.

In the case of the combination methods that produced the highest gains in classification accuracy, the rate of UITs was around 35–40%. There are three main reasons why the $\hat{\mathbf{P}}$-based methods classified a significant number of samples as UITs. Firstly, the data set used for training the methods was small and sparse, and overfitting is likely. Better training data containing a wider range of objects might improve performance. Secondly, the features used for the training were arbitrary and were chosen because of their simplicity. Using more complex and a larger number of features might improve results. Thirdly, commercial WTMD portals produce better SNR measurements than the experimental portal in this study, and improving the SNR of the system might lower the ratio of UITs.

6. Conclusions and future work

This paper has presented methods and knowledge that can take metallic object classification using WTMD-technology closer to practice. There is strong evidence that there is a significant positional and orientation bias component in the inverted tensors, and that the bias mostly affects the magnitude of tensor values. We have also proposed a novel classifier and shown, firstly, that it yields better classification accuracy than the previously presented methods, and secondly, that it is capable of classifying noisy and biased samples. The findings on UIT detection suggest that the reliability of classification can be improved by using features derived from the estimated object path.

Our findings give rise to several topics for future research. Previously, the residual has been used widely for considering the validity of solutions found by inversion algorithms, but we have shown that outlier detection methods, such as the UIT detection method described here, might be considered. Furthermore, research on diminishing the effect of the bias components should be carried out. This could be done either by redesigning the portal coils or developing classifiers and distance measures that are more robust against the bias components. Finally, the technology should be tested in a multi-object scenario where several metallic objects might be carried through the portal at a time.

The methods and results presented in this paper might also be applied to any EM metal detection technologies, such as humanitarian demining.

Acknowledgments

This work was supported by the Academy of Finland under the project ‘Magnetic Induction and Data Analyses for Sophisticated Sensing’, grant no. 251777.

References

[1] Kauppila J, Ala-Kleemola T, Vihonen J, Jylhä J, Ruotsalainen M, Järvi A and Visa A 2009 Classification of items in a walk-through metal detector using time series of eigenvalues of the polarizability tensor *Conf. Series Society of Photo-Optical Instrumentation Engineers* vol 7303

[2] Nelson C V 2004 Metal detection and classification technologies *Johns Hopkins APL Tech. Dig.* **25** 62–7
[3] Marsh L A, Ktistis C, Järvi A, Armitage D W and Peyton A J 2013 Three-dimensional object location and inversion of the magnetic polarizability tensor at a single frequency using a walk-through metal detector *Meas. Sci. Technol.* **24** 045102
[4] Makkonen J, Marsh L A, Vihonen J, Visa A, Järvi A and Peyton A J 2013 Classification of metallic targets using a single frequency component of the magnetic polarisability tensor *J. Phys.: Conf. Ser.* **450** 012038
[5] Makkonen J, Marsh L A, Vihonen J, Järvi A, Armitage D W, Visa A and Peyton A J 2014 Knn classification of metallic targets using the magnetic polarizability tensor *Meas. Sci. Technol.* **25** 055105
[6] Marsh L A, Makkonen J, Vihonen J, Visa A, Järvi A, Armitage D W and Peyton A J 2013 Investigation of the significance of the 'body effect' on sensitivity to metallic objects in a walk-through metal detector *J. Phys.: Conf. Ser.* **450** 012037
[7] Agurto A, Li Y, Tian G Y, Bowring N and Lockwood S 2007 A review of concealed weapon detection and research in perspective *IEEE Int. Conf. on Networking, Sensing and Control* pp 443–8
[8] Thomas T H, Barrow B J and Miller J T 2001 Subsurface discrimination using electromagnetic induction sensors *IEEE Trans. Geosci. Remote Sens.* **39** 1286–93
[9] Fails E B, Torrione P A, Scott W R and Collins L M 2007 Performance of a four parameter model for modeling landmine signatures in frequency domain wideband electromagnetic induction detection systems *Proc. SPIE* **6553** 65530D
[10] Zhang Y, Collins L, Yu H, Baum C E and Carin L 2003 Sensing of unexploded ordnance with magnetometer and induction data: theory and signal processing *IEEE Trans. Geosci. Remote Sens.* **41** 1005–15
[11] Norton S J, Won I J and Cespedes E R 2001 Ordnance/clutter discrimination based on target eigenvalue analysis *Subsurf. Sens. Technol. Appl.* **2** 285–98
[12] Norton S J and Won I J 2001 Identification of buried unexploded ordnance from broadband electromagnetic induction data *IEEE Trans. Geosci. Remote Sens.* **39** 2253–61
[13] Fernández J P, Barrowes B, O'Neill K A, Paulse K, Shamatava I, Shubitidze F, Sunin K, Broach J T, Harmon R S and Holloway J H (ed) 2006 Evaluation of svm classification of metallic objects based on a magnetic-dipole representation *Proc. SPIE Detection and Remediation Technologies for Mines and Minelike Targets XI* vol 6217 p 621703
[14] Makkonen J, Marsh L A, Vihonen J, Järvi A, Armitage D W, Visa A and Peyton A J 2015 Determination of material and geometric properties of metallic objects using the magnetic polarisability tensor *IEEE Sensors Applications Symp. Accepted for Publication*
[15] Al-Qubaa A R, Al-Shiha A and Tian G Y 2014 Threat target classification using ann and svm based on a new sensor array system *Prog. Electromagn. Res.* B **61** 69–85
[16] 2013 The National Institute of Justice (NIJ) www.nij.gov/
[17] Marsh L A, Ktistis C, Järvi A, Armitage D W and Peyton A J 2014 Determination of the magnetic polarizability tensor and three dimensional object location for multiple objects using a walk-through metal detector *Meas. Sci. Technol.* **25** 055107
[18] Duda R O, Hart P E and Stork D G 2000 *Pattern Classification* 2nd edn (New York: Wiley-Interscience)
[19] Hodge V J and Austin J 2004 A survey of outlier detection methodologies *Artif. Intell. Rev.* **22** 85–126
[20] Peng C-Y J, Lee K L and Ingersoll G M 2002 An introduction to logistic regression analysis and reporting *J. Educ. Res.* **96** 3–14
[21] Qian J, Hastie T, Friedman J, Tibshirani R and Simon N 2013 Glmnet for matlab www.stanford.edu/~hastie/glmnet_matlab/

Tampereen teknillinen yliopisto
PL 527
33101 Tampere

Tampere University of Technology
P.O.B. 527
FI-33101 Tampere, Finland

ISBN 978-952-15-3668-7
ISSN 1459-2045